# Quantitative characterization of solute transport processes in an undisturbed unsaturated soil by means of electrical resistivity tomography (ERT)

**Inaugural-Dissertation**

zur

Erlangung des Grades

Doktor der Agrarwissenschaft

(Dr. agr.)

der

Hohen Landwirtschaftlichen Fakultät

der

Rheinischen Friedrich-Wilhelms-Universität

zu Bonn

vorgelegt am 7. Mai 2009

von

Johannes Köstel

aus

Offenburg, Deutschland

Referent: Prof. Dr. H. Vereecken
Korreferenten: Prof. Dr. A. Kemna

Tag der mündlichen Prüfung: 23. Oktober 2009
Erscheinungsjahr 2010

## Acknowledgements

I firstly thank my promoter Prof. Harry Vereecken, head of ICG-4, Agrosphere, Forschungszentrum Jülich, and Prof. Andreas Kemna, formerly head of research group ‚Hydrogeophysical Imaging and Characterization' at ICG-4, presently Rheinische Friedrich-Wilhelms-Universität Bonn, for the opportunity and support to conduct this research.

This Ph.D. project would have led to nowhere without the support of many colleagues and the good working atmosphere at Agrosphere institute. I am very grateful to Prof. Andreas Kemna, Prof. Mathieu Javaux, Prof. Jan Vanderborght, and Prof. Harry Vereecken for numerous discussions on the Ph.D. project and for their comments on early drafts and parts of this manuscript.

I would like to thank all the people who were involved in setting up the lysimeter system as well as the measurements and analysis of the data. I thank Dr. Roy Kasteel for his advice on measurement instrument installations and Brilliant Blue related issues and the time spent on discussions on soil physics. I am grateful to Dr. Lutz Weihermüller and Dr. Sander Huisman for sharing their know-how on the TDR measurement system and data processing. I thank Dr. Thomas Pütz who led the excavation of the lysimeter and Jürgen Höltkemeier for numerous suggestions for solving problems with the experimental setup during the initial stages of the Ph.D. project. I owe thanks to Ansgar Weuthen who stood in for me to read out the data loggers when I was absent and, together with Egon Zimmermann, for solving the problem of short circuits of the ERT injection current through the TDR multiplexing system. The support of Ferdinand Engels, Elmar Mommertz and the staff of the ICG workshop was crucial for getting the lysimeter system operational. I am indebted to Rainer Harms for his helping hand in digging up the soil monolith and Ralf-Uwe Limbach for shooting excellent photos. I thank Odilia Esser for the Brilliant Blue analyses and Anke Langen for measuring the water retention curves. I am very, very grateful to the many colleagues who helped carrying the considerably heavy irrigation device!!

This Ph.D. project benefitted a lot from the expertise and the ERT inversion code of Prof. Andrew Binley at Lancaster University whom I also thank for the discussions during my visit in Lancaster and for his comments on partial drafts of this manuscript.

I thank Dr. Jürgen Schmalholz, formerly Technical University of Berlin, for his efforts with the GPR measurements, and I am grateful to Dr. Heiner Stoffregen, Technical University of Berlin, for providing water retention curves and texture analyses on Kaldenkirchen soil samples.

I owe thanks to Thomas Arnold for his help to improve the English in parts of this manuscript.

I thank all colleagues for the great atmosphere at ICG-4 - I had a good time. I will keep good memories of the soccer matches and of the institute band and our performances at the institute Christmas celebration. I especially thank Michael, Roy, Anne, Jana, Myriam, Christoph, Jing, Vladimira, Sarah, and Michel for companionship.

Last but not least, a big thank-you to my parents, family, and friends for their support and encouragement.

## Abstract

Improved understanding of water flow and solute transport through the unsaturated zone is important for the sustainable management of soils. As soils are complex and heterogeneous systems, quantification of the transport processes is difficult. More knowledge on the relationship between solute transport process, soil structure, hydrologic initial and boundary conditions, and observation scale is needed here. Therefore, non-invasive quantitative 3-D spatio-temporal imaging of solute displacement is necessary. Such imaging may be provided by hydro-geophysical methods, for example electrical resistivity tomography (ERT). Recent studies have shown that ERT is able to visualize solute transport through the subsurface with 3-D resolution, but quantitative interpretations of the ERT-image data are difficult.

This thesis explores the potential of ERT to quantitatively characterize vadose zone solute displacement with 3-D spatio-temporal resolution. Four inert solute transport experiments in a large undisturbed unsaturated soil column were imaged using 3-D ERT. Two experiments were conducted with an irrigation rate of 1.5 cm/d, the remaining two with an irrigation rate of 6.5 cm/d. An improved ERT-data-error estimation approach was introduced. Time-domain reflectometry (TDR) was applied to quantitatively ground-truth the ERT-image data. The experimental setup allowed translating the ERT-derived bulk electrical conductivity to solute concentration without neglecting the 3-D structure of the petrophysical properties of the soil. Using these innovations, ERT recovered the mass of the applied tracer with an error of approximately 5% for all four displacement experiments. The solute transport was characterized by means of ERT-derived apparent convection-dispersion equation (CDE) parameters. The apparent velocities were barely affected by the choice of the error level used in the ERT inversion but the apparent dispersivities were. The apparent velocities were less impaired by temporal smearing than the apparent dispersivities. The mean apparent velocity appeared to be not biased by ERT-sensitivity in contrast the velocity variability. The apparent dispersivities were barely correlated with decreasing ERT sensitivity.

In an additional displacement experiment, the food dye Brilliant Blue was directly imaged using ERT. Here, advantage was taken of the negative ionic charge of Brilliant Blue molecule under weakly acid and basic conditions. A comparison of photographically obtained Brilliant Blue staining patterns with respective ERT-derived solute electrical conductivity patterns showed that both patterns coincided as long as the staining features were not cut off from the electrodes.

The ERT-derived 3-D solute concentration images were useful to quantitatively investigate and compare the solute transport of the four inert solute displacement experiments. It was found that the main velocity patterns remained invariable for all four experiments despite a considerable increase in water content between the low and the high flux experiments. Another outcome was that all transport velocity patterns were aligned to a structural feature in the topsoil which, in turn, was aligned to the plowing direction and, therefore, identified as a man-made structure. The mixing regime of all displacement experiments was found to be convective-dispersive despite considerable lateral variations in the local transport velocity. The voxel-scale ERT-derived apparent dispersivity was successfully laterally up-scaled to the column scale using a newly introduced up-scaling approach. Furthermore, the up-scaling approach was useful to investigating the relationship between lateral observation scale and apparent dispersivity.

# Zusammenfassung

Für eine nachhaltige Bewirtschaftung von Böden ist es wichtig Wasserfluss- und Stofftransportprozesse durch die ungesättigte Zone besser zu verstehen. Da Böden komplex und heterogen sind, ist es schwierig, diese Transportprozesse zu quantifizieren. Mehr Wissen über die Beziehung zwischen Stofftransport, Bodenstruktur, hydrologische Anfangs- und Randbedingungen und Beobachtungsskala ist erforderlich. Dazu wird 3-D räumlich-zeitlich aufgelöste Bildgebung von Stofftransportprozessen benötigt. Eine solche Bildgebung kann von hydro-geophysikalischen Methoden bereitgestellt werden, zum Beispiel der elektrische Widerstandstomographie (EWT). Während der letzten Jahre haben Studien gezeigt, dass ERT in der Lage ist, Stofftransport durch den Untergrund in 3-D Auflösung zu visualisieren. Allerdings ist die quantitative Auswertung der EWT Bilddaten schwierig.

Diese Doktorarbeit untersucht das Potential von EWT, Stofftransportprozesse in der vadosen Zone quantitativ in 3-D räumlich-zeitlicher Auflösung zu charakterisieren. Während der Doktorarbeit wurden vier inerte Stofftransportexperimente in einer großen ungestörten Bodensäule mittels EWT visualisiert. Zwei Experimente wurden bei einer konstanten Beregnung von 1,5 cm/d durchgeführt, zwei bei einer Beregnung von etwa 6,5 cm/d. Ein verbesserter Ansatz zur EWT Fehlerabschätzung wurde eingeführt. Time-Domain Reflectometry (TDR) wurde benutzt um die EWT Bilddaten quantitativ zu validieren. Der Versuchsaufbau ermöglichte es, die mit EWT visualisierten elektrischen Leitfähigkeiten ohne Vernachlässigung der 3-D Struktur der petrophysikalischen Bodeneigenschaften in Stoffkonzentration zu übersetzen. Durch diese Innovationen konnte EWT die applizierte Tracermasse mit einem Massenbilanzfehler in der Größenordnung von 5% für alle vier Transportexperimente wiederfinden. Der Stofftransport wurde mit Hilfe von aus den EWT Bilddaten abgeleiteten scheinbaren Konvektions-Dispersions Gleichungsparameter charakterisiert. Im Unterschied zu den scheinbaren Geschwindigkeiten war die scheinbare Dispersivität stark abhängig von dem in der EWT Inversion gewählten Fehlerniveau sowie von zeitlichem Verschmieren. Der Mittelwert der scheinbaren Geschwindigkeiten war kaum von der sich änderenden EWT Sensitivität beeinflusst, die Variabilität der scheinbaren Geschwindigkeiten war es.

In einem zusätzlichen Experiment wurde der Lebensmittelfarbstoff Brilliant Blue direkt mit EWT visualisiert. Ein Vergleich zwischen photographisch bestimmten Brilliant Blue Färbemustern und entsprechenden bulk elektrischen Leitfähigkeiten der EWT Bilder zeigte, dass beide Muster übereinstimmen solange Bildregionen mit Färbekontrast nicht von den Elektroden abgeschnitten waren.

Die EWT Bilddaten zeigen, dass die Transportgeschwindigkeitsmuster während aller vier inerten Transportexperimente trotz eines deutlichen Anstiegs des Bodenwassergehaltes zwischen der niedrigen und der hohen Beregnungsrate weitgehend unverändert blieben. Ein weiteres Ergebnis ist, dass alle Transportmuster an einer Struktur im Oberboden ausgerichtet waren, welches wiederum in Pflugrichtung orientiert war. Die Transportregime aller vier Experimente erwiesen sich als konvektiv-dispersiv, obwohl in der lateralen Richtung deutliche Variationen in den lokalen Transportgeschwindigkeiten erkennbar waren. Die aus EWT abgeleitete scheinbare Dispersivität wurde erfolgreich von der lateralen Skala der EWT Bildvoxel auf die Skala der Bodensäule hochskaliert, wobei ein neu eingeführter Ansatz benutzt wurde. Dieser Ansatz war auch nützlich, den Zusammenhang zwischen scheinbarer Dispersivität und lateraler Beobachtungsskala zu untersuchen.

# Table of Contents

# 1. Introduction

## 1.1. Motivation

Sustainable management of soils is necessary to provide food and drinking water for the increasing world population. Here, the understanding of water flow and solute transport processes through the unsaturated zone is important (e.g. Flury, 1996; Vogel and Roth, 2003; Vereecken et al., 2007). As soils are complex systems which are heterogeneous at multiple scales, quantitative analyses and predictions are difficult (Vogel et al., 2006). 3-D spatio-temporally resolved monitoring is necessary to unequivocally relate solute transport characteristics to the structure of the soil hydraulic properties and state variables (Vanderborght, 2006).

Image series of solute transport processes with 3-D spatio-temporal resolution are provided by hydro-geophysical imaging techniques (Kemna et al., 2006), such as electrical resistivity tomography (ERT). ERT is known to be capable of visualizing solute transport in 3-D spatio-temporal resolution if a tracer with electrical conductivity contrast is used. A quantitative interpretation of ERT-image data, however, is difficult as the ERT inversion problem has no unique solution and needs to be regularized (Day-Lewis et al., 2005). Studies investigating ERT-derived solute concentrations report large mass balance errors (Binley et al., 2002; Singha and Gorelick, 2005). Using a favorable experimental setup and independent measurement methods to validate the ERT-image data, it may be possible to improve and assess the quantitative interpretability of ERT-derived solute concentrations. The latter may then be used to quantitatively investigate the 3-D spatio-temporal structure of solute displacement in an unsaturated undisturbed soil.

## 1.2. Water flow and solute transport theory

### 1.2.1. Water flow theory

Solute transport through soil is strongly dependent on the water flow. The latter is subject to soil hydraulic properties and hydrologic boundary conditions. At microscopic scale, soil hydraulic properties are determined the pore space properties (Roth, 2006). Explicit modeling of the water and air flow through the respective pore-network by using the Navier-Stokes equation requires excessive computational power. At present, investigations in this field of research are still constrained to very small scales as e.g. the publications of Lehmann et al. (2008) or Papafotiou et al. (2008) illustrate.

At the macroscale, the pore space properties determining the soil hydraulic properties are usually lumped into two effective parameters, namely unsaturated hydraulic conductivity, $K(\theta)$ (cm/d), in dependence of the water content $\theta$ (cm³/cm³) and soil water capacity, $C_w(h) = \partial\theta / \partial h$ (-), which relates water content and pressure head $h$ (cm) (Buckingham, 1907). If the air-phase in the pore space is continuous (degenerate multiphase flow regime), the water flux density, $j$ (cm/d), which is the water flow per area, can be described by the Buckingham – Darcy equation (Roth, 2006)

$$j = -K(\theta)\frac{\partial H}{\partial z}, \tag{1.1}$$

whereas $z$ (cm) is a space coordinate and $H$ is the hydraulic head, namely $h + z$. Combining Eq. (1.1) with the mass conservation law yields the Richards equation (Richards, 1931),

$$\frac{\partial \theta}{\partial t} - \frac{\partial}{\partial z} \cdot \left[ K(\theta) \frac{\partial H}{\partial z} \right] = 0 . \quad \textbf{(1.2)}$$

The Richards equation illustrates how the hydrologic state variables, namely water content, hydraulic head, and unsaturated hydraulic conductivity, governing the water flux through soil are intertwined.

### 1.2.2. Solute transport theory

Solute transport is typically described by the convective-dispersive equation (CDE)

$$\frac{\partial C}{\partial t} + v \frac{\partial C}{\partial z} - \frac{\partial}{\partial z} \cdot \left[ D \frac{\partial C}{\partial z} \right] = 0 . \quad \textbf{(1.3)}$$

In Eq. (1.3), $C$ (g/l) denotes the solute concentration, $v$ (cm/d) the solute transport velocity, and $D$ (cm²/d) the hydrodynamic dispersion which characterizes the solute spreading. The latter is expressed by means of the dispersivity, $\lambda$ (cm), which is $D$ / $v$ if molecular diffusion is negligible. Mostly, $v$ and $\lambda$ have been used as effective parameters. In this case the parameters are assumed to correctly describe the solute transport properties of the bulk soil through which the solute has travelled. However, although the application of CDE parameters yields reasonable results for some soils, it fails to predict the water flow and solute transport in many others when extrapolations in space and time are carried out (Jury and Flühler, 1992).

One reason why the CDE cannot predict the solute breakthrough curve is that, in macroscopically homogeneous porous media, the CDE is only valid in the far-field. The far-field is reached for travel times, $t$ (d), much larger than the mixing time, $t^*$ (d), which is a measure for the auto-correlation of the solute transport velocities (Bear, 1972). In the far-field the velocities are not correlated and the solute spreading is proportional to the travel time. In the near-field, i.e. $t << t^*$, the transport velocities are correlated and the solute spreading is proportional to the square of the travel time (Roth, 2006). The two transport mechanisms are referred to by means of the mixing regime (or transport regime) which is convective-dispersive (CD) for the far-field and stochastic convective (SC) for the near-field. When solute is applied to a surface of a macroscopically homogeneous soil, the solute transport process will initially exhibit a SC mixing regime on its passage towards the ground water. With increasing distance to the soil surface the solute particles traverse regions with different transport velocity whereas the auto-correlation in the velocity field disappears and the mixing regime asymptotically reaches the CD regime (Roth, 2006). It is straightforward that if the CDE is used although the far-field has not yet been reached, the solute spreading will not be predicted correctly (Jury and Roth, 1990).

### 1.2.3. The importance of heterogeneity and observation scale on solute displacement

The above considerations are restricted to macroscopically homogeneous soil. This is often a rather crude approximation for undisturbed soil. If the transport properties of a considered soil are macroscopically heterogeneous, effective transport model parameters are only valid for the specific block of soil from which they have been obtained. For such a soil, effective parameters are of minor use for predictive spatial extrapolations on solute

displacement. Heterogeneities in soil hydraulic and solute transport parameters are present at every spatial scale, from the pore scale (µm – mm), the laboratory scale (cm – dm), and the pedon (or Darcy) scale (dm – m) to the field (m – km) and regional scale (> km) (following Vereecken et al., 2007). Often, predictions for large scales are needed for environmental management. However, it is known that processes occurring at smaller scales affect the processes at larger scales (Vogel and Roth, 2003). It follows that it is vital to understand water and solute transport processes at all sub-scales. Up-scaling relationships are needed to link the processes occurring at smaller scales to the scale of interest (e.g. Vereecken et al., 2007)

For undisturbed soil at the pedon and field scale, heterogeneities of the solute transport properties in the vertical direction are intuitively expected as pedogenetic processes mostly lead to horizontal layering of soil (Scheffer and Schachtschabel, 2002). Publications illustrating the importance of the correct implementation of the soil layering in solute transport models are e.g. Abbaspour et al. (2000) or Vanderborght and Vereecken (2008). Apart from soil layering, heterogeneities in the horizontal direction are important (Nielsen et al., 1973; Rudolph et al., 1996). Soil layers are not perfectly uniform and their width varies laterally, impacting the soil hydraulic properties (e.g. van Wesenbeeck and Kachanoski, 1994; Jacques et al. 1998). Preferential flow paths may form along root channels or burrows of the soil fauna (Jarvis, 2007). Other reasons for preferential flow are hydrophobicity of soil organic material (Ritsema and Dekker, 1994) or heterogeneity in the soil texture (Kung, 1990; Javaux et al., 2006). Also, anthropogenetic features can affect the solute transport properties of soil as numerous studies on the impact of wheel tracks show (e.g. Öhrström et al., 2004; Cocquet et al., 2005). The study of Flury et al. (1994) illustrates the large importance of lateral heterogeneities on solute transport in undisturbed soil.

In general, lateral heterogeneity leads to an increase in solute spreading with increasing lateral observation scale (van Wesenbeeck and Kachanoski, 1991; Ward et al., 1995; Vanderborght et al., 2001; Javaux and Vanclooster, 2003) until the largest scale at which heterogeneities exist is reached. This has to be considered if field-scale solute transport properties are to be estimated on base of soil column experiments.

### 1.2.4. The impact of hydrologic initial and boundary conditions on solute displacement

As it is obvious from Eqs. (1.1) and (1.2), the unsaturated hydraulic properties depend on the degree of water saturation. Therefore, the solute transport properties of soil are strongly affected by the hydrologic initial and boundary conditions. It is straightforward that a larger water flux density will result in an increased solute transport velocity. Furthermore, the studies of Wildenschild et al. (1999) and Ursino et al. (2001) in 2-D tanks illustrate how the transport paths change in heterogeneous porous media with applied irrigation rate. The same was demonstrated with numerical studies carried out by Roth and Hammel (1996) or Vanderborght (1998). Consequently, it was observed for solute transport experiments in packed laboratory columns and real soils that the magnitude of the apparent dispersivity (e.g. Padilla et al., 1999; Maciejewski, 1993; Javaux et al., 2006) and also the mixing regime (Khan and Jury, 1990; Forrer et al., 1999; Ursino et al., 2001; Persson et al., 2005) are sensitive to the hydrologic initial and boundary conditions.

## 1.3. Petrophysical models

Often, ionic solutes are used in order to trace solute displacement by means of their electrical conductivity contrast. If measurements of the bulk electrical conductivity, $\sigma_b$ (µS/cm), of the soil are available, a petrophysical relationship has to be parameterized in order to relate the ERT-derived bulk electrical conductivity to the solute electrical conductivity, $\sigma_w$ (µS/cm). Petrophysical relationships which are based on the empirical relationship known as Archie's law (Archie, 1942) are often applied. Archie's law states that the solute electrical conductivity is proportional to the bulk electrical conductivity for saturated porous soil if the electrical mineral surface conductivity (which is strongly related to the size of the clay fraction) is negligible,

$$\sigma_b = \frac{\sigma_w}{F}. \tag{1.4}$$

In Eq. (1.4), $F$ (-) is referred to as the formation factor which accounts for porosity $\Phi$ (cm³/cm³) and the pore-network geometry. An often utilized extension to Archie's law which is applicable to unsaturated soils is the relationship published by Waxman and Smits (1968):

$$\sigma_b = \frac{S^n}{F}\left(\sigma_w + \frac{\sigma_s}{S}\right). \tag{1.5}$$

In Eq. (1.5), $S$ (-) is the water saturation, namely the water content $\theta$ divided by the porosity $\Phi$, $n$ is the saturation exponent which is related to the geometry of the wetted pore space, and $\sigma_s$ (µS/cm) is the electrical conductivity of the mineral surfaces. The review of Friedman (2005) gives an overview of present approaches to model the petrophysical relationships.

## 1.4. Measurement methods used for solute transport investigations

This section gives an overview over methods to investigate solute transport processes in soils without being exhaustive. Distinction is made between non-invasive (or minimal-invasive) imaging methods that provide spatio-temporal resolution (tomographical methods) and all other methods (non-tomographical methods).

### 1.4.1. Non-tomographical methods

Early solute transport experiments aimed at obtaining effective transport properties of the soil. Therefore, leaching experiments were conducted whereas the effluent was collected and so-called breakthrough curves (BTCs) were investigated. By means of inverse modeling, specific transport parameters depending on the considered transport model (e.g. CDE) could be attributed to the entire soil block.

Later on, suction cups (e.g. Biggar and Nielsen, 1976; Patterson et al., 2000) were additionally installed. They provided information on subscale heterogeneity by measuring resident solute concentration. Weihermüller et al. (2005) showed that suction cups modify the local matrix potential and therefore the transport paths. This method is, therefore, of limited use for investigations on the spatial structure of solute transport.

In contrast, time-domain reflectometry (TDR) probes provide resident solute concentrations without modifying the flow field. TDR was originally developed to determine the soil moisture content (e.g. Topp et al., 1980). Since the 1990's, it was also used to measure bulk electrical conductivity (Heimovaara et al., 1995). In this manner, breakthrough curves of resident concentrations of solutes with electrical contrast can be sampled. TDR has been shown to yield a quantitatively better insight into the heterogeneity of solute transport than suction cups (Vanclooster et al., 1995; Vanderborght et al., 1997; Javaux and Vanclooster, 2003). However, the method is restricted to local measurements, and the spatial resolution is therefore limited.

Dye staining methods provide a better spatial resolution. First dye tracer experiments were interpreted qualitatively (e.g. Steenhuis et al., 1990; Flury et al., 1994). By the end of the 1990s, approaches for quantitative evaluation of dye-staining data were developed. In this fashion, spatially highly resolved information is yielded (Forrer et al., 2000). It has been successfully used to investigate links between soil structures and transport processes (Forrer et al., 1999; Perillo et al., 1999; Javaux et al., 2006; Vogel et al., 2006). According to Persson (2005), quantitative dye staining is presently superior to any other method in terms of spatial resolution. An important drawback of most dye staining approaches is their destructive nature. Unless the experiment is restricted to 2-D, like experiments that are carried out in soil containers with transparent walls (Wildenschild and Jensen, 1999; Ursino, et al. 2001), only one snapshot of the transport process can be obtained. The combined effects of flow rate, water saturation, and soil properties on the 3-D structure of the transport process can only be observed in an indirect manner.

In addition to experiments with real soils, numerical simulations in virtual unsaturated soils provided insight into fundamental aspects of water flow and solute transport. Roth (1995) and Roth and Hammel (1996) published an experiment whose results suggest that the structure of the flow and transport process change as well with the applied flow rate as the water saturation degree of the medium. Vanderborght (2001) demonstrated in a numerical study that similar solute concentration distributions are possible in soil-like media with completely different structures. It follows that spatio-temporal monitoring of transport is necessary to relate soil structures unequivocally to the structure of the transport process (Vanderborght et al. 2006).

### 1.4.2. Tomographical methods

Here, 3-D geophysical imaging methods provide new possibilities. Positron emission tomography (PET) and single photon emission computed tomography (SPECT) can image solute transport processes with a spatial resolution of a few millimeters (see Khalili et al., 1998; Gründig et al., 2007; Perret et al., 2000). The underlying principle of both methods is the detection of $\gamma$-rays which are emitted from an appropriate radioactive tracer. Their applicability is limited due to the related efforts necessary to prevent contaminations. Respective solute transport studies have, to our knowledge, so far been constrained to soil columns smaller than 50 cm.

Instead of $\gamma$-rays, X-rays can be used for imaging. For X-ray computed tomography the rays are generated outside the soil sample, transmitted through it, and detected on a photo plate (e.g. Cnudde et al., 2004). The method was frequently applied in soil science,

predominantly for the visualization of soil structure (Taina et al., 2008). Given an appropriate tracer, the method can as well be applied to solute transport imaging (Peyton et al., 1994; Clausnitzer and Hopmans, 2000). At present, resolutions of less than 10 µm can be obtained (e.g. Kaestner et al., 2008). However, the high resolution has to be traded in for sample size, which is not larger than a few millimeters for high resolution images (Taina et al., 2008). For larger samples X-ray computed tomography still yields a resolution of less than 1 millimeter (Cnudde et al., 2004). It is to note that no publication was found during a literature research in which samples larger than some 10 centimeters were imaged by means of X-ray computed tomography.

Another tomographical method, magnetic resonance imaging (MRI), measures the precession of atomic nuclei with non-zero spin imprinted by an externally applied magnetic field (Blümich, 2000). Yoon et al. (2008) report a spatial resolution of 0.2 mm for an experiment carried out on a small tank filled with packed sand (14 centimeters in length). However, the application of MRI in natural soils is hindered by abundance of paramagnetic materials as well as the large internal heterogeneity of structure and geochemical composition (Hall et al., 1997; Votrubova et al., 2003). Furthermore, most present MRI scanners depend on a cylindrical magnet that embraces the soil sample. The method is therefore constrained to samples of some 10 centimeters, 120 cm at maximum (Blümich, 2000).

The above discussed methods are, at least presently, constrained to the laboratory scale. When vadose zone transport processes at larger scales were investigated with spatio-temporal resolution, mainly two methods have been applied: ground penetrating radar (GPR) and electrical resistivity tomography (ERT). The underlying principle of GPR is the emission of a radar wavelet into the subsurface which is, after being modified due to its passage through the soil, recorded by a receiver antenna. The information in the received signal can be used to image both, the dielectric properties and the bulk electrical conductivity of the soil (Annan, 2005). As data processing is more straightforward for the former, most field studies focus on visualizations based on the soil dielectric properties (Binley et al., 2001, 2002a; Schmalholz et al., 2004; Looms et al., 2008), which are related to the soil water content $\theta$. Examples for imaging of electrical conductivity are Day-Lewis et al. (2003) and Chang et al. (2006) who used tracers with electrical conductivity contrast to investigate solute displacement. GPR can be applied from a scale of some centimeters up to a scale of several kilometers (Huisman, 2003). The resolution of GPR depends on the radar frequency, the radar beam coverage, data error, the amount of regularization applied in the image reconstruction (Day-Lewis et al., 2005). It varies in space. Schmalholz et al. (2004) estimate resolutions in the decimeter range for their small-scale experiment ($58 \times 58 \times 140 \times \pi$ cm), Day-Lewis et al. (2003) give resolution estimates between 1.3 and 2.9 m for a cross-borehole experiment with a well separation of approximately 10 meter.

ERT is used to image the bulk electrical conductivity $\sigma_b$ of the soil. The method works by injecting direct electrical current in the subsurface using two electrodes, which are part of an ERT electrode array which can comprise over 200 electrodes. The electrical potential field resulting from the current injection is explored by means of so-called 'transfer resistance' measurements using electrode pairs in which none of the injection electrodes is included. For each ERT image reconstruction, transfer resistance measurements from multitude of electrode quadruples are needed. One such ensemble of transfer resistance measurements is referred to as one 'frame' in the following. Similarly to GPR, the ERT image resolution and accuracy are spatially non-constant. This issue is discussed in more detail in the next section.

The capability of ERT to image processes with 3-D electrical conductivity contrast has been shown since the end of 1980s (Daily, et al., 1987; Daily, et al., 1992; Ramirez, et al., 1993; Binley, et al., 1996a; LaBrecque, et al., 1996). If the spatio-temporally resolved characteristics of solute transport are investigated, the pixel (2-D) or voxel (3-D) breakthrough curves proved to be useful. The concept was introduced by Binley et al. (1996a) and was subsequently applied by Olsen et al. (1999), Slater et al. (2000, 2002). As an extension to this approach, apparent transport model parameters can be obtained by fitting the CDE to the individual pixel/voxel BTCs (Kemna et al., 2002; Vanderborght et al., 2005). In this way the features of local solute breakthrough curves are captured by means of only two parameters: the apparent transport velocity and the apparent dispersivity. Advantages of ERT are its low cost, its automatizability, and its applicability for a very wide range of scales, from some decimeters (e.g. Olsen et al., 1999) up to kilometers (Revil et al., 2008).

Finally, induced polarization (IP) imaging has to be mentioned as an extension to ERT. ERT measures resistances of direct current, the former uses alternated current. IP can be further extended to spectral IP (SIP) where more than only one injection current frequency is applied. The use of alternating current provides information about the polarizability of the bulk soil, which can be deduced from the phase-shift between injection current and measured transfer resistance (Binley and Kemna, 2005). The polarizability of the soil is related to the pore space and soil particle geometry and to soil particles with ion exchange capacities (Slater, 2007). There are justified hopes that information on the hydraulic conductivity of soils can be obtained from SIP phase spectra (Börner et al., 1996; Slater, 2007). As a further step, the phase of the IP/SIP signals can be visualized with spatial resolution using an approach similar to ERT image reconstruction (Kemna 2000; Kemna et al., 2004). It follows that SIP imaging may provide not only the solute transport velocity field (and the heterogeneity of solute spreading at the scale of the image resolution) but as well the information of the underlying hydraulic properties may be inferred with spatial resolution.

## 1.5. ERT imaging of hydrologic processes

### 1.5.1. ERT accuracy and resolution issues

The ERT inversion problem is ill-conditioned and ill-posed. The former means that small errors in the data can lead to large errors in the results. It follows that the appraisal of the measurement and model error plays an important role. Ill-posedness denotes in our case that the problem has no unique solution. It must, therefore, be regularized. Ideally, this is done by data from an independent complementary method or by a-priori-known characteristics of the bulk electrical conductivity structures which are sought to be imaged (e.g. spatial statistics). Both are seldom available. In this case, mostly the smoothness constraint is applied. This typically leads to specific bias in the ERT inversion image

(Kemna et al., 2002, Friedel, 2003; Day-Lewis et al., 2005; Singha and Gorelick, 2006; Day-Lewis et al., 2007) which in turn may cause bias in ERT-derived tracer mass (Binley et al., 2002b; Singha and Gorelick, 2005) or ERT-derived transport parameters (Vanderborght et al., 2005).

Similar to GPR, the resolution and accuracy of ERT is spatially non-constant. They depend on the ERT survey design, the structure of the electrical conductivity distribution of the investigated domain, and the data error (Day-Lewis et al., 2005). It follows that the ERT-image resolution and accuracy can only be known in an approximate manner. There are several approaches to appraise bias and errors in ERT images. However, when applied to 3-D problems they either demand excessive computational power, e.g. the model resolution matrix (e.g. Friedel 2003; Day-Lewis et al. 2005; Oldenborger and Routh, 2009) or e.g. Bayesian inversion approaches (Yeh et al., 2002; Ramirez et al., 2005); or they provide a rather qualitative measure of regions prone to bias, e.g. sensitivity analyses (e.g. Spitzer, 1998; Kemna et al., 2002). Only very recently, Oldenborger et al. (2007) introduced the so-called volume of investigation index which can be regarded as a semi-quantitative approach. However, considering the rapid development towards more powerful computer systems, it is to expect that computational limitations will not further be an issue for quantitative image-error appraisal in the very near future, even for large 3-D problems.

### 1.5.2. State of the art in ERT imaging of hydrologic processes

Due to spatially varying accuracy and bias in the ERT-image data it is crucial to support a ‘ground truth’ for the ERT images by means of an independent method. Among the studies which focus on solute concentration are many which confirm the qualitative agreement between ERT-image data and data from an independent method (Binley et al., 1996a; al Hagrey and Michaelson, 1999; Olsen et al., 1999; Slater et al., 2000; French et al., 2002). Studies in which the validity of the ERT image data is quantitatively investigated include Slater et al. (2002) and Singha and Gorelick (2005, 2006). Slater et al. (2002) compared voxel-scale ERT-derived breakthrough curves with data collected from observation wells in a solute tracer experiment under saturated conditions. They found a broad quantitative agreement in both magnitude and arrival times of the local-scale tracer pulses but dispensed with investigations at the bulk scale of the experiment. In contrast, Singha and Gorelick (2005) reported that ERT detected only 25% of the recovered mass in their field-scale tracer experiment. In a subsequent publication they investigated the corresponding local scale ERT-derived BTCs by means of a multi-level observation well (Singha and Gorelick, 2006). To our knowledge, this is the only study available in which, at the same time, both the quantitative validity of ERT images at the (voxel) local scale and at the bulk scale of the experiment have been investigated by means of an independent method.

Slater et al. (2002) and Singha and Gorelick (2006) carried out their studies on ERT image data validation in the saturated zone. They made use of observation wells. In the vadose zone, these are not applicable. Instead, the already discussed TDR may be used. Al Hagrey et al. (1999a and b) presented experimental setups at which several geophysical methods including ERT and TDR were applied jointly for validation and synergetic reasons. However, the authors abstain from a quantitative comparison of the results. Michot et al. (2003) have shown that a petrophysical relationship can be parameterized by combing ERT and TDR-derived data. Here, the authors abstained from validation approaches but their results strongly indicate that TDR-derived water content measurements are consistent with

corresponding ERT-derived bulk-electrical conductivities. However, a direct quantitative relation between ERT and TDR-derived bulk electrical conductivity has not yet been established.

Another promising approach is the use of dye staining for ERT-image validation. Binley et al. (1996a) used Methylene Blue and showed that ERT and dye staining patterns were consistent. A novel approach would be to use a dye tracer with electrical conductivity contrast (such as Brilliant Blue) and image the dye staining patterns both photographically and by means of ERT. The joint application of both methods bears several advantages such as a spatially resolved mutual ground truth for the two methods or incorporation of the Brilliant Blue staining patterns into the ERT image reconstruction algorithm.

For comparing ERT-derived transport parameters of different transport experiments, it is essential that data inversion has been applied with similar levels of regularization. Variation in ERT data error, due to different degrees of water and solute saturation, have to be compensated; bias due to the varying distance that the tracer travels during the ERT data acquisition time, in the following referred to as temporal smearing, has to be attributed; a data selection approach has to be considered that minimizes the differences in ERT-sensitivity between all available ERT-frames. This illustrates that it is difficult to quantitatively compare 3-D spatially resolved ERT-derived data from different solute displacement experiments. To our knowledge such a study has not yet been published in peer-reviewed literature. At best, Olsen et al. (1999) presented a study which aims in this direction but conclusions drawn from the ERT image data remain qualitative.

## 1.6. Objectives and thesis outline

The here presented study is concerned with investigations of 3-D solute transport processes through the vadose zone by means of ERT. In this context several solute displacement experiments were conducted in a large soil column (lysimeter) filled with undisturbed field soil. The thesis has two main objectives. The first one is to examine the potential and limitations of smoothness constraint ERT to quantitatively image solute displacement. The second objective is using ERT-images to quantitatively characterize and compare solute transport within the previously determined capabilities of ERT.

The chapters two and three deal with the first objective. In chapter two, the TDR-derived electrical conductivity is investigated as to its usefulness as a ground truth for ERT at the local scale. At the same time, the effluent BTC is compared with respective bulk scale ERT-measurements. The chapter also contains refined approaches for pre-processing and error analysis of ERT data and a method to translate electrical conductivity changes to changes in solute concentration taking into account a 3-D parameterization of a petrophysical model whereas the parameters need not to be determined explicitly.

Chapter three is concerned with investigations on direct ERT-imaging of Brilliant Blue by means of its electrical conductivity contrast. Both, photographically and ERT-derived dye concentration patterns are related quantitatively by means of a petrophysical model. Agreement and deviations of the staining patterns are discussed.

Chapter four discusses the quantitative validity and comparability of ERT-image data of four specific steady state solute displacement experiments using TDR and effluent data as a ground-truth. Furthermore, effects of spatially varying ERT sensitivity and temporal smearing on the ERT-derived apparent CDE-parameters are investigated.

Chapter five relies strongly on the results presented in chapter four. Here, the solute transport process characteristics of the four experiments are inferred from the ERT-derived apparent CDE parameters. The effects of irrigation rate and lateral scale on the transport

characteristics are investigated.

Finally, chapter six summarizes and presents the main outcomes of the Ph.D. project and discusses possible future applications of ERT with respect to solute transport characterization.

# 2. Quantitative imaging of solute transport in an unsaturated and undisturbed soil monolith with 3-D ERT and TDR*

## 2.1. Introduction

The quantitative description and prediction of solute movement through the vadose zone is essential for sustainable soil and ground water management. During the last few decades numerous studies have been carried out which contributed to this topic (Corey et al., 1967; van der Pol et al., 1977; De Smedt et al., 1986; Vanderborght et al., 2001; Javaux et al,. 2006) including in particular soil column experiments with well defined boundary conditions (Corey et al., 1967; Mallants et al., 1994; Javaux and Vanclooster, 2003). In such studies, solute breakthrough curves (BTC) typically are measured in the column's effluent. They provide integrated and flux-averaged information on the processes governing solute transport in the column. However, if solute displacement is sought to be understood correctly, e.g. in order to make predictions, the local scale transport properties have to be known. Here, we define the local scale as a scale smaller than the column scale for which data are available. As the local scale transport properties cannot be measured directly in a non-destructive manner, the resident solute concentrations during inert tracer experiments can be measured instead. The local scale apparent transport parameters can be obtained by inversely fitting analytical or numerical solutions of transport models, such as, e.g., the CDE, to the solute breakthrough data.

Typically, two methods are used to determine resident solute concentrations in a non-destructive manner: suction cups and time-domain reflectometry (TDR). Suction cups have been used for a long time in soil science to determine local-scale solute concentrations, both in the laboratory and in the field (e.g. Biggar and Nielsen, 1976; Patterson et al., 2000). However, Weihermuller et al. (2005) showed that suction cups modify the local matrix potential and therefore the transport paths. This method is, therefore, of limited use for a quantitative description of local solute breakthrough. Although TDR was originally developed to determine soil moisture content (e.g. Topp et al., 1980), the method also has been used since the 1990's to measure bulk electrical conductivity (Heimovaara et al., 1995). In this manner, breakthrough curves of resident concentrations of solutes with electrical contrast can be sampled. TDR has been shown to yield a quantitatively better insight into the heterogeneity of solute transport than suction cups (Vanclooster et al., 1995; Vanderborght et al., 1997; Javaux and Vanclooster, 2003). However, the method is restricted to local measurements, and the spatial resolution is therefore limited.

During the 1990's, it was shown that electrical resistivity tomography (ERT) can provide a much better spatial resolution of resident solute concentrations in the course of tracer experiments than local methods such as TDR (Binley et al., 1996a). A quantitative interpretation of ERT images, however, remains difficult due to several limitations related to the underlying inversion process and the diffusive nature of electrical flow (e.g. Day-

* adapted from Koestel, J., Kemna, A., Javaux, M., Binley, A. and Vereecken, H. 2008. Quantitative imaging of solute transport in an unsaturated and undisturbed soil monolith with 3-D ERT and TDR. Water Resources Research 44, W12411, doi:10.1029/2007WR006755.

Lewis et al., 2005; Kemna et al., 2006). In addition, the uncertainty of inferred solute transport characteristics from ERT analysis remains ignored.

An additional problem from using ERT image data arises from the fact that the bulk electrical conductivity is dependent on water content, solute concentration, and surface electrical conductivity. So, once spatially distributed bulk electrical conductivities are obtained from ERT data inversion, these conductivities have to be separated into the three contributing conductors by means of petrophysical relationships. In order to do this, information on the petrophysical model parameters and their topology is required. Such data are rarely available. Numerous studies, therefore, assume spatially constant petrophysical relationships and negligible surface conductivity (e.g. Kemna et al., 2002; French et al., 2002; Winship et al., 2006).

Several studies have been carried out using independent methods to quantitatively verify the image data obtained from ERT. Some of them investigate the ERT-derived water contents, whereas others focus on ERT-derived solute concentration. Binley et al. (2002b) found a good quantitative agreement between cross-borehole ERT and zero-offset ground penetrating radar in terms of the velocity of the center of mass of an injected water plume. However, it was not within the scope of their study to draw conclusions about the validity of the ERT image data at the local scale. Michot et al. (2003), in contrast, investigated the validity of ERT image data at the local scale, although they give no statement about the validity at the bulk scale of the experiment.

Among the studies which focus on solute concentration are many which confirm the qualitative agreement between results from ERT and an independent method (Binley et al., 1996a; al Hagrey and Michaelson, 1999; Olsen et al., 1999; Slater et al., 2000; French et al., 2002). Studies in which the validity of the ERT image data is quantitatively investigated include Slater et al. (2002) and Singha and Gorelick (2005, 2006). Slater et al. (2002) compared voxel-scale ERT-derived breakthrough curves with data collected from observation wells in a solute tracer experiment under saturated conditions. They found a broad quantitative agreement in both magnitude and arrival times of the local-scale tracer pulses but dispensed with investigations at the bulk scale of the experiment. In contrast, Singha and Gorelick (2005) reported that ERT detected only 25% of the recovered mass in their field-scale tracer experiment. In a subsequent publication they investigated the corresponding local scale ERT-derived BTCs by means of a multi-level observation well (Singha and Gorelick, 2006). To our knowledge, this is the only study available in which, at the same time, both the quantitative validity of ERT images at the (voxel) local scale and at the bulk scale of the experiment have been investigated by means of an independent method.

In vadose zone, however, well-based sampling is difficult to employ. In this study we address two points which are necessary in order to investigate solute transport processes in the vadose zone quantitatively by ERT image data: (i) the bulk electrical conductivity has to be translated into solute concentration and (ii) a quantitative ground truth for the ERT imaging results has to be provided at the local scale; additionally, the validity of the ERT imaging results has to be checked at the scale of the experiment if a ground truth cannot be appraised for every single voxel explicitly.

Here, we present results from an experiment in which a solute tracer was applied to an undisturbed soil monolith and monitored by means of smoothness-constrained ERT and TDR as well as measurements in the effluent. The experiment was designed in a way

which allowed us to relate bulk electrical conductivity to solute concentration without neglecting spatial variations in water content and mineral surface conductivity. We investigate the impact of different ERT inversion parameters on the imaging results. We contrast the (voxel-) local-scale ERT-derived bulk electrical conductivity and solute concentration with corresponding TDR data. Additionally, the shapes of the solute breakthrough curves from ERT and TDR are quantitatively compared by means of apparent transport model parameters. As a cross-check of the validity of our approach at the scale of the experiment, we compare the ERT-derived apparent 1-D transport model parameters with the corresponding values determined from the effluent breakthrough data.

## 2.2. Experimental setup

### 2.2.1. Experimental design

The experiment consists of a two step tracer test applied to a large undisturbed soil monolith under steady state unsaturated flow conditions. A constant irrigation rate of 1.5 cm/d (standard deviation 0.1 cm/d) was applied throughout the experiment. Initially, the column was irrigated with tap water and after steady state conditions had been established the tap water was replaced by a $CaCl_2$ solution (providing a positive electrical conductivity contrast) for a period of 47 days. The complete tracer breakthrough took about 30 days, although the data collection was extended to all 47 days after the tracer application (48 days in total). During the last 17 days of the experiment, chemical steady state had been established and hence the precision of the measurement devices could be checked.

The temperature corrected (nLF, 25 °C, see DIN.EN.27888, 1993) tap-water background conductivity was adjusted to 503 µS/cm by adding $CaCl_2$ or distilled water. This electrical conductivity was equivalent to a mean chloride concentration of 54 mg/l (stdev: 2 mg/l). For the tracer solution, we added approximately 925 mg/l of $CaCl_2$ adjusting the solute electrical conductivity to 2530 µS/cm. This corresponds to a chloride concentration of 642 mg/l (stdev: 15 mg/l). The deviations were caused by slight changes in the tap-water ion composition during the experiments.

### 2.2.2. Soil monolith and soil material

We used a PVC column of 150 cm in height with an inner diameter of 116 cm and a wall thickness of 2 cm (Figure 2.1a) to excavate an undisturbed sandy soil monolith from an agricultural field site near Kaldenkirchen (Germany). The topmost and bottommost 5 cm of the column were not filled with the sample: at the bottom, the corresponding gap was backfilled with sand; at the top, the soil surface was covered with a thin layer of fine gravel in order to prevent erosion caused by irrigation.

In total, 212 stainless steel electrodes (1.2 cm in diameter) were installed extending 3 cm into the soil, respectively. The majority of the electrodes (192) were arranged equidistantly with a horizontal spacing of 11.8 cm at six different soil depths along the circumference of the column (Figure 2.1a). Additionally, five electrodes were placed vertically in between each of the six electrode rings along four vertical transects. We used the 6-channel GeoServe RESECS instrument with corresponding relay boxes for electrode switching to carry out the ERT measurements.

In addition to the ERT electrodes, ten TDR probes were inserted into the column. The TDR probes were positioned diametrically opposed to each other at five different depths (Figures 2.1a,b). We used a three-rod design similar to the one employed by Heimovaara

(1993). We chose a rod length of 18.8 cm and a rod spacing of 2.5 cm. The rod spacing to diameter ratio was 10:1. The TDR signals were generated and recorded by means of the Campbell Scientific TDR100 system. The dielectric constant as well as the signal attenuation was logged at one hour intervals using Campbell Scientific SDMX50 multiplexers and a Campbell Scientific CR10X data logger. In order to avoid electricity short cuts through the TDR cables and potential artifacts in the ERT images, switches were built in between TDR probes and multiplexers. In this way, we were able to electrically isolate the TDR probes from each other whenever ERT measurements were performed. Thus, we could apply both methods, ERT and TDR, simultaneously although they had to be alternately switched on and off.

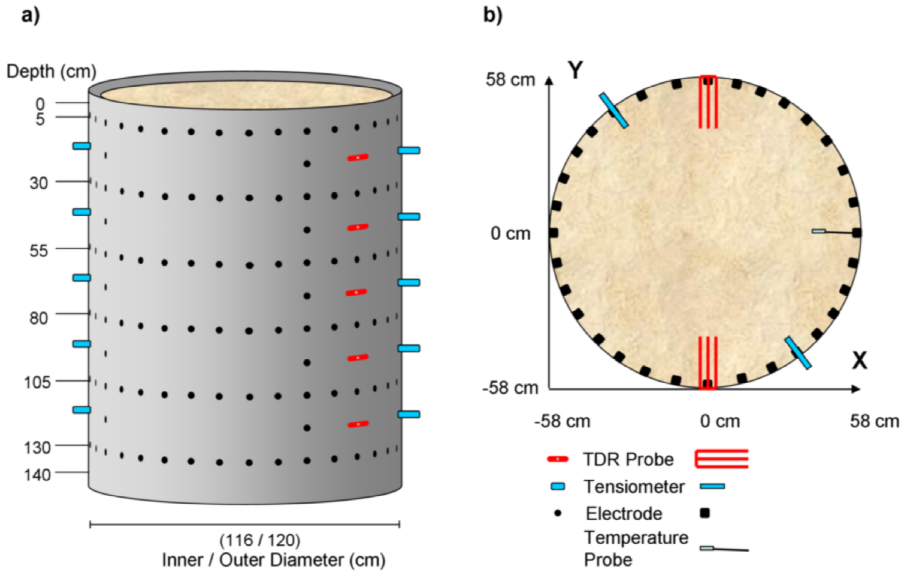


**Figure 2.1: Soil column and instrumentation (a) and horizontal cross-section of the soil (b).**

Next to each TDR probe a tensiometer (UMS T4) was installed (see Figure 2.1b). The tensiometer data were logged every ten minutes with aid of a MAC19 data logger. In addition, a resistance temperature detector (PT100) was installed at each TDR / tensiometer plane.

In order to discriminate between the two vertical TDR and tensiometer transects, they are, in the following, referred to by their XY coordinates (0 | 58) and (0 | -58) in centimeter.

### 2.2.3. Boundary conditions

The experiment was performed in a basement of the lysimeter facility of the Forschungszentrum Jülich. The ambient temperature was kept around 10 °C (+/- 2 °C) to minimize temperature effects on the electrical conductivity. An irrigation device, consisting of 484 needles, was placed on top of the soil column, allowing spatial uniformity of the irrigation. The soil column was mounted on a balance in order to verify steady state conditions. The lower section of the soil column was water saturated during the experiments.

Twelve openings in the bottom section of the column allowed discharge to a 100 ml tipping bucket (UGT Müncheberg). The flow rate was measured and logged on the MAC19 data logger and the effluent was then conducted through a vessel where the electrical conductivity and the water temperature were measured at 10 minute intervals by a WTW Condi325 conductivity meter.

## 2.3. Methods

### 2.3.1. TDR measurements

The TDR data were used to measure the water content $\theta$ (cm³/cm³) as well as the bulk electrical conductivity. For the water content measurement, the bulk dielectric constant $\xi_b$ (-) was used to infer water content using the composite dielectric approach (Roth et al., 1990):

$$\theta = \frac{\xi_b^\alpha - (1-\Phi)\xi_s^\alpha - \Phi\xi_a^\alpha}{\xi_w^\alpha - \xi_a^\alpha}.$$

**(2.1)**

Here, $\xi_s$, $\xi_a$, and $\xi_w$ refer to the temperature corrected dielectric constant of soil solid, air, and water phase, respectively, and $\Phi$ is the porosity. The corresponding values were taken from Roth et al. (1990). They are listed in Table 2.1. The geometry factor $\alpha$ was set to 0.5, which corresponds to the Complex Refractive Index Model (CRIM) (e.g. West et al., 2003).

**Table 2.1: Dielectric numbers ξ which we used to calculate the water content at the TDR positions. The indices s, a, and w stand for solid phase, air, and water, respectively.**

| $\xi_{s,topsoil}$ | $\xi_{s,subsoil}$ | $\xi_a$ | $\xi_w$ (9.5 °C) |
|---|---|---|---|
| 5 | 3.9 | 1 | 84.3 |

The bulk electrical conductivity $\sigma_b$ (µS/cm) was obtained from the TDR signal attenuation for measurement times long after the main detection of the reflected signal. We related the signal attenuation to the bulk electrical conductivity of the soil in the vicinity of the TDR rods using the relationship

$$R_{TDR} = Z_C \frac{(1+\rho_\infty)}{(1-\rho_\infty)}.$$

**(2.2)**

Here, $\rho_\infty$ is the reflection coefficient at very long times, and $Z_C$ is the impedance of the TDR device, multiplexer, and cable. $R_{TDR}$ is the ensemble resistance of $Z_c$ and the resistance of the bulk soil (Heimovaara et al., 1995; Mallants et al., 1996). This then permits estimation of the bulk electrical conductivity according to

$$\sigma_b = \frac{K_p}{R_{TDR} - R_{Cable}}.$$

**(2.3)**

Here, $K_p$ is the cell constant of the TDR probe, and $R_{Cable}$ is the resistance associated with cable tester, multiplexers, and connecters, only.

Both $K_p$ and $R_{Cable}$ were determined for each probe individually using calibration measurements. Therefore, the signal attenuation was measured for TDR probes immersed in water with a known electrical conductivity. The measurements were carried out for eight different electrical conductivities ranging from 11.6 µS/cm to 618 µS/cm. For the calibration process, the mean absolute residuals <*R*> were below 1 µS/cm. Given the bulk electrical conductivities which we measured during the experiment (25 - 300 µS/cm), we can infer a TDR accuracy of 0.3 to 4%. This is in the range of the accuracy of TDR electrical conductivity measurements published by Huisman et al. (2008).

After the TDR probes were installed, the precision of the TDR electrical conductivity measurements was investigated under hydraulic and chemical steady state conditions. We found the coefficient of variation for the electrical conductivity measurements collected during 10 consecutive days to be below 2% for all TDR probes, with a mean coefficient of variation of approximately 1%. The precision of the TDR system is hence rated as high.

## 2.3.2. ERT imaging

2.3.2.1. Inversion algorithm

We carried out 3-D time-lapse ERT inversions to map changes in the spatial distribution of bulk electrical conductivity $\sigma_b$ (µS/cm) inside the soil monolith. We performed 46,260 'skip-1' dipole-dipole measurements (see Slater et al., 2000, for more details on this configuration) for each measurement frame (50% of which were reciprocal measurements – where current and potential dipoles are switched – in order to assess data quality). We used dipole-dipole configurations with both horizontal and vertical dipoles. The dipole length was 22.8 cm for the horizontal scheme and 25 cm for the vertical schemes. The measurement time for one complete measurement frame was 8:23 h. One frame per day was recorded. We inverted the ERT data for each frame individually by means of the error-weighted, smoothness-constrained 'Occam's type' inversion code R3t. No time-lapse regularization was applied. The code utilizes a triangular prism-based finite-element solution of the forward problem (Binley et al., 1996b) and has been previously demonstrated for soil core experiments by Olsen et al. (1999). The algorithm finds the smoothest distribution of electrical conductivity which fits the measured data to a specified error level $\varepsilon_{app}$ using the approach described in Binley and Kemna (2005).

The ERT inversion produces an image of $M$ voxel electrical conductivities ($\sigma_j$, $j = 1, 2, \ldots, M$) given a set of $N$ measurements of four-electrode resistance ($R_i$, $i = 1, 2, \ldots, N$) by minimizing the objective function, $\Psi$, given by

$$\Psi = \left\| \mathbf{W}_\varepsilon \left[ \mathbf{d} - f(\mathbf{m}) \right] \right\|^2 + \alpha \left\| \mathbf{W}_s \mathbf{m} \right\|^2 \qquad \textbf{(2.4)}$$

Here, $\boldsymbol{d}$ is the data vector, given by

$$d_i = -\log R_i \quad i = 1, 2, \ldots, N;$$

the parameters of the inversion, $\boldsymbol{m}$, are given by

$$m_i = \log \sigma_j \quad j = 1, 2, \ldots, M;$$

$f(\mathbf{m})$ is the forward model for parameters $\mathbf{m}$; $\mathbf{W}_\varepsilon$ is an error weighting matrix; $\mathbf{W}_s$ is a smoothness operator representing the discretized second derivative; $\alpha$ is a regularization

parameter which determines the amount of smoothing imposed on **m** during the inversion.

For the ERT forward problem, the soil column was partitioned into 14,720 triangular prisms (edge length ≈ 6 cm). For the inverse problem, in order to reduce computational demands, we discretized the column into 3680 parameters. Thus, patches of 4 adjacent finite elements were lumped to one parameter, respectively (height ≈ 6 cm, horizontal edge length ≈ 12 cm).

During the extraction of the soil column from the ground, the initially circular column cross-section was deformed to a slightly ellipsoid shape. In a first approach, we used a perfectly cylindrical mesh to represent the column for the ERT inversion. In doing so, all horizontal cross-sections of the ERT images exhibited a symmetrical feature which was aligned to the column wall deformation. This strongly suggests an artifact due to electrode and domain boundary misplacement. After we had implemented corrected electrode and column wall positions into the mesh, these features were reduced to a large extent. The corresponding changes in magnitude of the electrical conductivity were up to 50% (depending on the error level $\varepsilon_{app}$). This finding stresses the importance of accurate implementation of the electrode and domain boundary positions into the inversion mesh.

If $\varepsilon_i$ is the measurement error in resistance $R_i$ represented by the standard deviation, and if we assume that the measurement errors are uncorrelated, then $\mathbf{W}_\varepsilon$ in Eq. (2.4) is a diagonal matrix defined as

$$\mathbf{W}_\varepsilon = diag\left[\frac{R_1}{\varepsilon_1}, \frac{R_2}{\varepsilon_2}, ..., \frac{R_N}{\varepsilon_N}\right]^T . \tag{2.5}$$

The inversion is stopped when the root-mean-squared error $\varepsilon_{RMS}$ reaches the target value of one. The root-mean-squared error $\varepsilon_{RMS}$ is given by

$$\varepsilon_{RMS} = \frac{1}{N}\sqrt{\sum_{i=1}^{N} W_{\varepsilon,i}\left(\mathbf{d}_i - f_i(\mathbf{m})\right)^2} . \tag{2.6}$$

From Eq. (2.6) and the objective function in Eq. (2.4) it is apparent that the smoothness inherent in the final ERT image is affected by the error estimates used to compute the data weighting matrix $\mathbf{W}_\varepsilon$.

The true error $\varepsilon$ comprises the measurement error as well as numerical (modeling) errors resulting from, for example, discretization errors or electrode positioning errors (LaBrecque et al., 1996; Zhou and Dahlin, 2003; Oldenborger et al., 2005). In this study, we assumed that $\varepsilon$ can be approximated using an absolute resistance error component, $a_{app}$ (Ω), and a relative resistance error component, $b_{app}$ (-), according to

$$\boldsymbol{\varepsilon}_{\mathbf{app}} = a_{app} + b_{app}\mathbf{R} . \tag{2.7}$$

The optimal error weighting matrix $\mathbf{W}_\varepsilon$ is related to the error level $\varepsilon_{opt}$ which characterizes all noise in the system most accurately. An underestimation of $\varepsilon$ leads to artifacts in the inversion results whereas its overestimation results in overly smooth ERT images (Binley et al., 1995; LaBrecque et al,. 1996).

The ERT inversion problem is ill-conditioned, meaning that small errors in the data can lead to large errors (artifacts) in the results. In order to reduce the impact of noisy data on the ERT image we made use of a robust ERT inversion scheme as described in LaBrecque and Ward (1990). Here, the error weighting matrix $\mathbf{W}_\varepsilon$ is adapted for individual data points during each iteration (while the L2-norm is used to measure both model and data misfits). According to Morelli and LaBrecque (1996), reasonable results can be achieved with this approach even if the true error level is underestimated by one order of magnitude.

However, even if using the robust inversion scheme, the inversion results still depend upon: (i) the choice of the error level $\varepsilon_{app}$ and (ii) the criteria with which data points (e.g. outliers) are removed from the data set prior to inversion.

2.3.2.2. Data error analysis

In ERT studies, data error has been typically appraised by either repeatability or reciprocity checks. The error estimate which results from the latter approach, here referred to as the reciprocal error $\varepsilon_{N/R}$, is empirically known to provide more useful values (e.g. LaBrecque et al., 1996). However, as an estimate of the true error $\varepsilon$, the reciprocal error $\varepsilon_{N/R}$ has substantial flaws. First, it is only a measure of precision and not accuracy. Additionally, it does not take into account correlations between the individual errors. Furthermore, it does not account for numerical errors. Hence, we subsequently used $\varepsilon_{N/R}$ only as a starting and reference point for different parameterizations of error level $\varepsilon_{app}$. In order to reduce the degrees of freedom in this approach, we only consider uniform error level $\varepsilon_{app}$ for all measurement configurations and time frames. Likewise, we neglect any correlation amongst the errors.

Detailed information about how $\varepsilon_{N/R}$ can be determined is reported in LaBrecque et al. (1996) and Slater et al. (2000). Here, we present an approach which is an extension to the method proposed by LaBrecque et al. (1996).

We first removed all obvious outliers from the ERT data set. This was done in two steps. First of all, all data which lie outside pre-defined bounds of measured voltage, injection current, and coefficient of variation from stacking measurements (see Slater et al., 2000) were discarded. The bounds were chosen based on empirical knowledge. They are listed in Table 2.2. Then, all data with a reciprocal error larger than 100% of the corresponding mean (of the normal and reciprocal) transfer resistance $R_{N/R}$ were removed. After performing this process 17,000 to 20,000 of the initial 23,130 normal and reciprocal data were retained for each frame.

**Table 2.2: Pre-defined error bounds for first ERT data filtering.**

| | Lower bound | Upper bound |
|---|---|---|
| Injection current (mA) | 2 | 100 |
| Potential measurement (mV) | 0 | 5000 |
| Coefficient of variation of stacked potential measurements (%) | 0 | 5 |

In the next stage we subdivided the range of measured transfer resistances into logarithmically equally sized bins. For each bin, the standard deviation $s_{bin}$ of the reciprocal errors in that bin was calculated. Note that the standard deviation $s_{bin}$ of the

reciprocal error is the double of the standard error of the mean transfer resistance $R_{N/R}$. The error model parameters $a_{N/R}$ and $b_{N/R}$ were determined by fitting the right-hand side of Eq. (2.8) to $s_{bin}$ (Figure 2.2). The fitted parameters $a_{N/R}$ and $b_{N/R}$ define the error $\varepsilon_{N/R}$ which represents the standard deviation of the reciprocal error:

$$\boldsymbol{\varepsilon}_{\mathbf{N/R}} = a_{N/R} + b_{N/R}\mathbf{R}_{\mathbf{N/R}}. \tag{2.8}$$

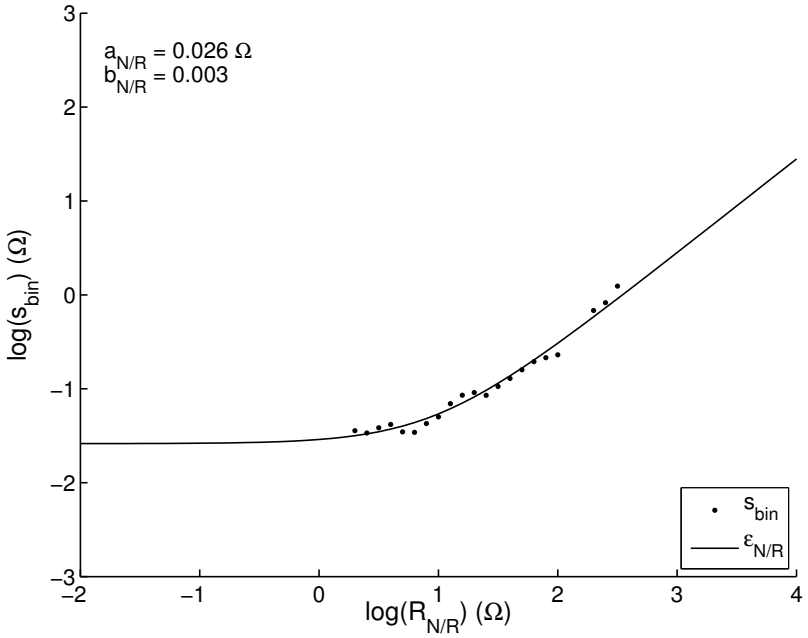


**Figure 2.2: The standard deviation $s_{bin}$ of the N/R misfits which were collected in bins and the corresponding error model fit $\varepsilon_{N/R}$ for the first of the 48 ERT frames. The error model parameters $a_{N/R}$ and $b_{N/R}$ are shown in the upper left of the Figure.**

Following this approach, we found that $\varepsilon_{N/R}$ decreased with progression of the tracer front (Figure 2.3). An explanation for this behavior is that the increased solute concentration enhanced the electrode to soil contact. From this it follows that $\varepsilon_{N/R}$ is spatially variable, not only because of varying solute concentration but also because of spatially varying water content. Indeed, we could confirm this when applying the N/R error analysis to subsets of the ERT data. Additionally, we could observe an increase of $\varepsilon_{N/R}$ when the tracer front was passing the location of the corresponding data subset. We attribute this to the temporal aliasing which occurred due to the time gap between normal and reciprocal measurements. The time gap was not fixed for the individual electrode configurations and varied between some minutes up to 8 hours. However, in a first approach, we restrict ourselves in investigating the spatially and temporally mean $\varepsilon_{N/R}$ only (i.e., in the following, $\varepsilon_{N/R}$ always denotes the spatially and temporally mean $\varepsilon_{N/R}$). The mean of the error model parameter $a_{N/R}$ was found to be 0.009 Ω (maximum 0.031 Ω) whereas the mean of parameter $b_{N/R}$ was 0.5% (maximum 1.1%).

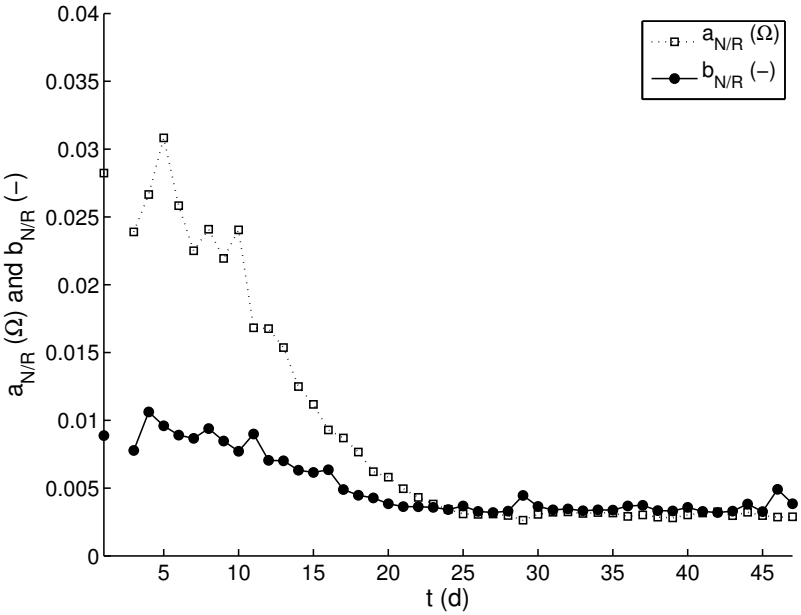


**Figure 2.3: Time series of N/R error model parameters found during the experiment.**

2.3.2.3. Data selection

The mean transfer resistances $R_{N/R}$ of all electrode configurations of an individual time frame are referred to as data points in the following. When a time series of individual ERT frames has to be inverted, it is desirable to (i) invert identical data points for each individual frame in order to yield similar sensitivity distributions for each frame, (ii) invert data points which are distributed as uniformly as possible over the inversion domain, and (iii) reduce the number of data points in order to decrease the computational demand.

In the following we used $\varepsilon_{N/R}$ to meet the first criteria. Data points which had a N/R misfit larger than the five-fold of $\varepsilon_{N/R}$ in at least one of the 48 frames were removed for the entire time series. With this approach, the number of retained data points was 6,371, covering the whole inversion domain. We are aware that the choice of the threshold is largely arbitrary. Furthermore, a constant threshold leads to a bias in the spatial data point density when regions with varying electrode contact are present, e.g. due to spatial water content variations. Spatially varying thresholds with respect to the electrode contact could be used to obtain a uniform data point distribution. For sake of simplicity we refrain from refined data selection approaches in this study. Instead, we focus on comparing inversion results of different error levels $\varepsilon_{app}$. The investigated $\varepsilon_{app}$ were chosen with respect to the reciprocal error $\varepsilon_{N/R}$.

## 2.3.3. Relating electrical conductivity to solute concentration

The soil bulk electrical conductivity is assumed to be related to the solute electrical conductivity $\sigma_w$ (µS/cm) according to the model of Waxman and Smits (1968)

$$\sigma_b = \frac{1}{F}\sigma_w + \sigma_s \,, \tag{2.9}$$

where $\sigma_s$ (µS/cm) is the ohmic surface conductivity of the soil solid phase (largely related

to the clay content in the soil) and $F$ (-) is the so-called formation factor. Following Archie's law (Archie, 1942), the formation factor $F$ accounts for pore space characteristics. For simplicity, we here also incorporate the saturation dependence of the electrolytic conductivity component in Eq. (2.9) (according to Archie's 'second equation') into the formation factor, which then can be written as

$$F = \omega\Phi^{-m}\left(\frac{\theta}{\Phi}\right)^{-n}, \tag{2.10}$$

where $\Phi$ is the porosity, $\theta$ the water content, and $\omega$, $m$, and $n$ are empirical (fitting) parameters.

In order to relate bulk electrical conductivity to solute concentration, five assumptions are made.

(i) Firstly, we assume that under hydraulic steady state conditions the formation factor (here including the water content influence) was spatially variable but remained temporally constant. Knowledge of the actual porosity, the water saturation, and the formation and saturation exponents is not needed.

(ii) In the second assumption we presume that the ohmic mineral surface conductivity remained approximately constant during the course of our experiment, i.e., was in a first approximation independent of salinity. There is evidence in literature that this assumption is justified (e.g. Revil and Glover, 1998) in the regime of our experiment.

(iii) In order to apply the approach, we have to know the solute concentration in the soil water for the entire soil column for two distinct salinity states. Hence, the third assumption is that the solute concentration in the soil water was spatially constant after the solute concentration in the effluent had reached stable values.

If the three assumptions are valid, the solute electrical conductivity $\sigma_w$ is spatially constant at two salinity states: state 1 at the start of the experiment when $\sigma_w$ corresponded to tap water (503 µS/cm) and state 2 at the end of the experiment when $\sigma_w$ corresponded to $CaCl_2$ solution (2,530 µS/cm).

Based on the first three assumptions we can derive the electrical conductivity of the solute at an arbitrary state $t$ from the bulk electrical conductivity at state 1 and state 2. Firstly, we set up Eq. (2.9) for all three solute saturation states and obtain

$$\sigma_{b,t} = \frac{1}{F}\sigma_{w,t} + \sigma_{s,t}, \qquad \sigma_{b,1} = \frac{1}{F}\sigma_{w,1} + \sigma_{s,1} \text{ and} \qquad \sigma_{b,2} = \frac{1}{F}\sigma_{w,2} + \sigma_{s,2}. \tag{2.11a,b,c}$$

Next, we subtract Eq. (2.11b) from Eq. (2.11a) and Eq. (2.11c), respectively. This yields

$$\sigma_{b,t} - \sigma_{b,1} = \frac{1}{F}\sigma_{w,t} - \frac{1}{F}\sigma_{w,1} \text{ and} \qquad \sigma_{b,2} - \sigma_{b,1} = \frac{1}{F}\sigma_{w,2} - \frac{1}{F}\sigma_{w,1}. \tag{2.12a,b}$$

The mineral surface conductivity is cancelled out.

In a last step, we divide Eq. (2.12a) by Eq. (2.12b) which results in

$$\frac{\sigma_{w,t}-\sigma_{w,1}}{\sigma_{w,2}-\sigma_{w,1}}=\frac{\sigma_{b,t}-\sigma_{b,1}}{\sigma_{b,2}-\sigma_{b,1}}.$$

**(2.13)**

The impact of the formation factor is, thus, cancelled out as well.

Two further assumptions are used to relate bulk electrical conductivity to solute concentration C. We assume that the relationship between relative changes of chloride concentration $(C_t-C_1)/(C_2-C_1)$ and solute electrical conductivity $(\sigma_{w,t}-\sigma_{w,1})/(\sigma_{w,2}-\sigma_{w,1})$ was

(iv) constant over time and

(v) identical to the one found for the effluent.

Here, $C_t$ is the chloride concentration for time *t*, $C_1$ is the chloride concentration at salinity state 1 (54 mg/l) and, $C_2$ is the chloride concentration at salinity state 2 (642 mg/l).

The corresponding function, here denoted as *g*, was determined by relating the chloride content in the effluent with the corresponding electrical conductivity measurements:

$$\frac{(C_t-C_1)}{(C_2-C_1)}=g\left(\frac{\sigma_{w,t}-\sigma_{w,1}}{\sigma_{w,2}-\sigma_{w,1}}\right).$$

**(2.14)**

Eq. (2.14) can be resolved to chloride concentration at time *t*, $C_t$:

$$C_t=g\left(\frac{\sigma_{w,t}-\sigma_{w,1}}{\sigma_{w,2}-\sigma_{w,1}}\right)(C_2-C_1)+C_1.$$

**(2.15)**

All measured electrical conductivities were corrected for temperature using the relationship of Franson (1985). Although the environment of the laboratory was temperature controlled, temperature shifts up to a magnitude of ±4 °C occurred due to malfunctions of the climate control and impacts of outside temperature variations over the duration of the experiments (15th of November 2005 to 1st of January 2006).

We observed that the electrical conductivity $\sigma_w$ of the effluent (maximum: 440 µS/cm) did not reach that of the irrigation water (503 µS/cm). Again, after the soil water ionic content in the effluent was in equilibrium with the tracer irrigation water, the electrical conductivity of the effluent was lower than the one of the irrigation water (2,450 µS/cm compared to 2,530 µS/cm). Both times, the balance of $Ca^{2+}$ concentration between irrigation water and effluent is negative. A probable explanation for the decrease in salinity is hence calcium carbonate precipitation together with degassing of carbon dioxide. We are aware that this violates our assumptions made for the calibration of the petrophysical model. However, for sake of simplicity, we ignore this fact and assume a closed solute electrical conductivity balance at this point (constant 440 µS/cm and constant 2,450 µS/cm for the first and last frame, respectively).

An analysis of irrigation and outflow water showed that the mass of applied chloride was conserved during the experiment (mass balance: 98.3%). Analyzing the effluent, we found

that the function $g$ in Eq. (2.15) between change in solute electrical conductivity and change in chloride concentration was not linear but exponential. We fitted a second-order polynomial to the data in order to relate solute electrical conductivity to chloride concentration.

Subsequently, we used Eq. (2.15) to derive (i) the breakthrough curve of the flux-averaged chloride concentration in the effluent, (ii) the breakthrough curves of the resident chloride concentration sampled with each TDR probe, and (iii) the breakthrough curves of the resident chloride concentration for each ERT voxel. The scaling was performed for each TDR probe and each ERT voxel and the effluent data individually by means of the bulk electrical conductivities $\sigma_{b,1}$ and $\sigma_{b,2}$ which were measured at the corresponding probe/voxel as well as the effluent data.

### 2.3.4. Comparing ERT data to TDR and effluent data

With an estimated accuracy of approximately 1% (Huisman et al., 2008) and a measured precision of approximately 1%, we consider TDR as appropriate to rate the validity of the electrical conductivity data which were obtained with ERT.

The sampling volume of a three-rod TDR probe is sensitive to the rod-spacing to rod-diameter ratio which is in our study 10:1. According to Ferré et al. (1998), the sampling volume of our probes can be approximated by a cylinder around the central rod with a radius of one and a half time the rod spacing and length of the rods (approximately 800 cm³). It should be noted that the sensitivity is strongly biased toward the vicinity of the rods.

The volume of one ERT voxel is approximately 90 cm³, although the voxel size should not be confused with the ERT resolution. In order to compare ERT and TDR data, we related the mean of the ERT electrical conductivity of all voxels intersecting the TDR sampling volume to the corresponding TDR probe.

We compare the TDR- and ERT-derived BTCs by means of apparent CDE parameters, the apparent velocity $v_a$ (cm/d) and the apparent dispersivity $\lambda_a$ (cm):

$$\frac{dC}{dt} + v_a \frac{dC}{dx} - \lambda_a v_a \frac{d^2C}{dx^2} = 0 \,. \qquad \textbf{(2.16)}$$

Here, we fit the solution of the 3rd type boundary value problem for a step input and for resident concentrations to the BTCs (Parker and van Genuchten, 1984). The apparent CDE velocity $v_a$ and the apparent CDE dispersivity $\lambda_a$ are not related to a physical process. Similar to temporal moments they merely capture the main characteristics of the breakthrough curve in a condensed manner (see e.g. Vanderborght et al., 2001). We use the apparent CDE parameters since they provide better means to compare breakthrough curve data from different depths and flow rates. Temporal moments always change with depth and flow rate whereas for a homogeneous transport process, the apparent CDE parameters should remain constant with depth and the dispersivity with flow rate. Changes of these parameters with depth and flow rate directly indicate heterogeneous transport.

The flux concentrations measured in the effluent of the column were fitted using the solution of the CDE for a first-type boundary condition. By means of the apparent CDE parameters, we were able to quantitatively compare the breakthrough curve of the mean resident chloride concentrations of the bottommost ERT voxels with the one of the flux

concentration which was measured in the effluent. This provided an additional evaluation of the quantitative interpretability of the ERT images.

The residuals between TDR and ERT-derived apparent velocity $Rd_v$ and apparent dispersivity $Rd_\lambda$ were calculated according to

$$Rd_v = \frac{v_{a,<ERT>} - v_{a,TDR}}{v_{a,TDR}} \tag{2.17}$$

and

$$Rd_\lambda = \frac{\lambda_{a,<ERT>} - \lambda_{a,TDR}}{\lambda_{a,TDR}}. \tag{2.18}$$

Likewise, the residuals between the apparent CDE parameters for the effluent BTC and the averaged BTC of the bottommost ERT voxels were calculated.

## 2.4. Results and Discussion

### 2.4.1. ERT bulk electrical conductivity images

The three-dimensional variation in bulk electrical conductivity, $\sigma_b$, for day 0, day 13, and day 30 is shown in Figure 2.4. The corresponding error model parameters were $a_{app} = 0.02\ \Omega$ and $b_{app} = 0.01$. The left-hand side of Figure 2.4 (day 0) depicts the initial state where the soil water composition corresponded to tap water composition. The right-hand side of Figure 2.4 (day 30) depicts the final state where the composition of soil water corresponded to the $CaCl_2$ solution. Therefore, the bulk electrical conductivity of day 0 and day 30 provide explicit information on the water content distribution inside the lysimeter. The distribution is (qualitatively) in accordance with the TDR-derived water content (Figure 2.5).

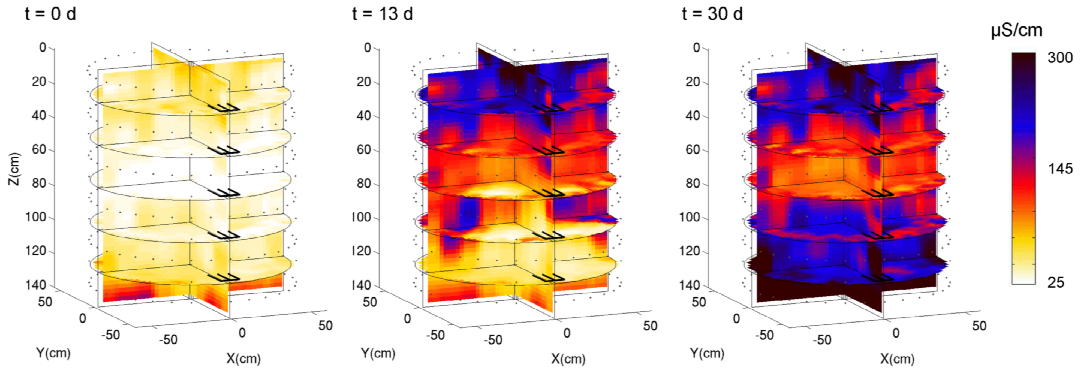


**Figure 2.4: The 3D ERT bulk electrical conductivity at $t$ = 0 d, $t$ = 13 d and $t$ = 30 d for $a_{app}$ = 0.02 Ω and $b_{app}$ = 0.01 ($\varepsilon_{app} \approx 2\varepsilon_{N/R}$).**

The image shown in the central position in Figure 2.4 (day 13) corresponds to a day when the tracer front had reached the bottommost third of the column. It can be seen that the tracer front cannot be delineated from a single bulk electrical conductivity image alone.

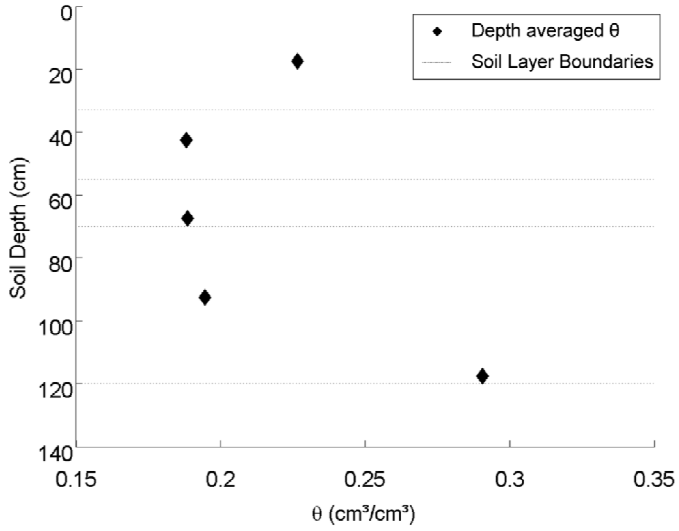


**Figure 2.5: The water content profile inside the soil column measured with TDR.**

## 2.4.2. Comparison of ERT- and TDR-derived bulk electrical conductivity

Figure 2.6 shows the BTCs obtained from TDR and the corresponding ERT-derived voxel BTCs at a depth of 42.5 cm. The impact of the different $\varepsilon_{app}$ on the ERT bulk electrical conductivity can be seen. For $\varepsilon_{app} << \varepsilon_{N/R}$ (Figure 2.6, top), the voxel BTCs and the corresponding mean BTC are relatively noisy, whereas for $\varepsilon_{app} >> \varepsilon_{N/R}$ (Figure 2.6, bottom), the BTCs are quite smooth. At the depth of 42.5 cm, the ERT image-derived electrical conductivity was consistently larger than the one captured with TDR. When $\varepsilon_{app}$ is slightly larger than $\varepsilon_{N/R}$, the mean voxel BTC matches the TDR data best. As an example, the results with $\varepsilon_{app} \approx 2\varepsilon_{N/R}$ are shown in Figure 2.6 (middle).

Figure 2.7 shows vertical bulk electrical conductivity profiles at the two TDR transects at day 31. By this time, the CaCl2 solution had replaced all the tap water in the soil and, thus, the observed spatial variability in electrical conductivity is attributed to spatial variations in water content and clay content rather than solute concentration. Instead they are caused by spatial variations in water content and clay content. If we infer from the layering of the soil that the horizontal gradients in water content and clay content are negligible as compared to the vertical gradients, we can explain the systematic deviations between the smooth ERT images and TDR at an individual soil depth, e.g. at depth 42.5 cm (see Figure 2.6, bottom, and Figure 2.7).

The locations of the peaks in the electrical conductivity profile of the inversion with $\varepsilon_{app} << \varepsilon_{N/R}$ and $\varepsilon_{app} \approx 2\varepsilon_{N/R}$ in Figure 2.7 correspond to the depths of the horizontal electrode rings. The troughs correspond to the inter-ring positions where the TDR probes are located. It is hence unlikely that this artifact-like feature is related to the metal rods of the TDR probes as the metal rods would result in an increase of electrical conductivity. The feature resembles rather an artifact due to an underestimation of the optimal error

level: it becomes less associated with the ERT sensitivity distribution as well as less pronounced with larger $\varepsilon_{app}$.

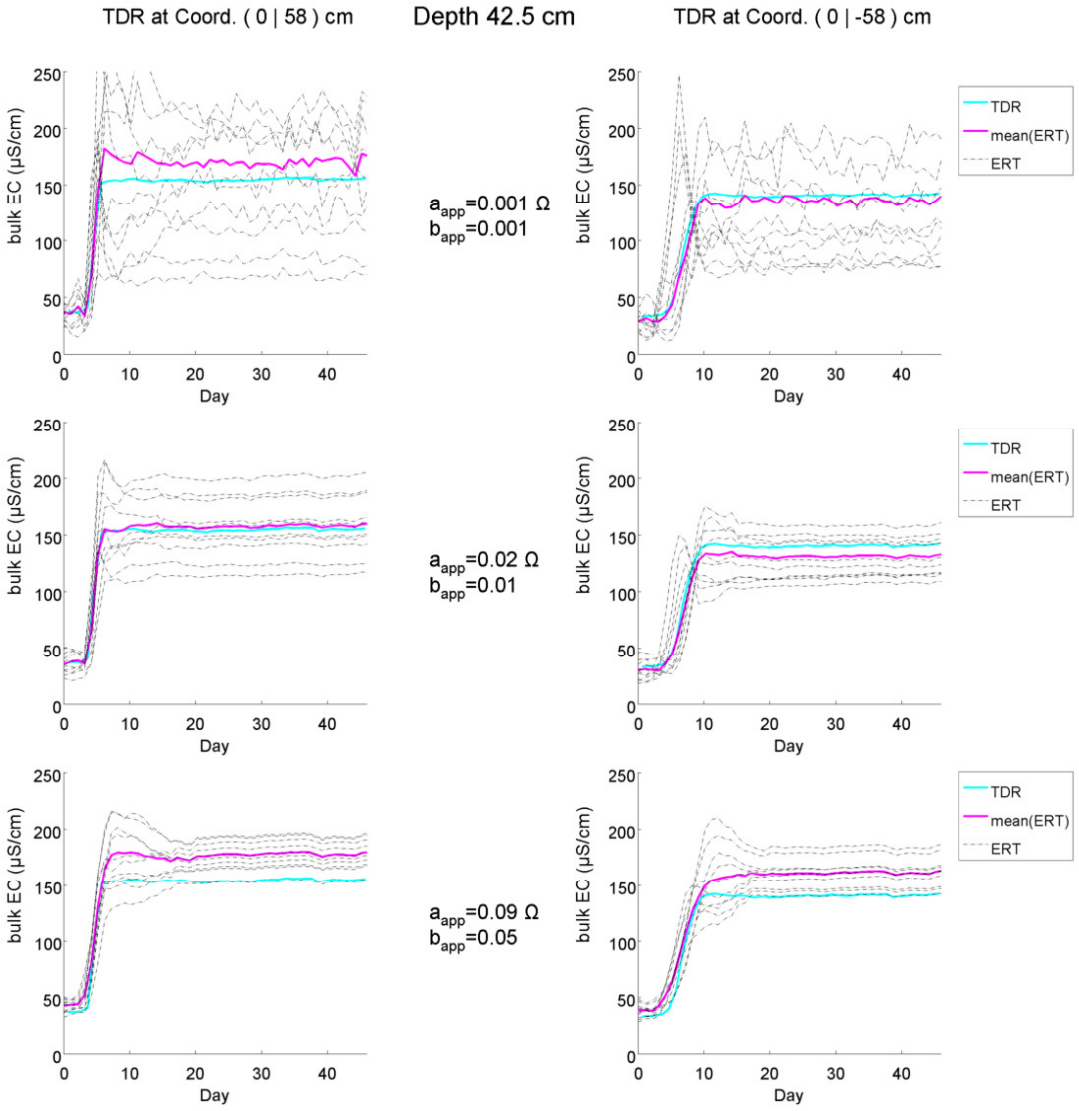


**Figure 2.6: TDR bulk electrical conductivity (EC) BTCs at depth 42.5 cm compared with the mean ERT voxel BTC in vicinity to the corresponding TDR probe locations. Additionally, the corresponding individual voxel BTCs are depicted. The impact of the ERT inversion error level on the results is shown for three examples: $\varepsilon_{app} << \varepsilon_{N/R}$ (top), $\varepsilon_{app} \approx 2\varepsilon_{N/R}$ (middle) and $\varepsilon_{app} >> \varepsilon_{N/R}$ (bottom).**

As discussed above, the mismatch between ERT and TDR is largely dependent on the error level $\varepsilon_{app}$ used in the ERT inversion. Apart from this there may have been other contributing factors. Firstly, the different sampling volumes of TDR and ERT could have led to a mismatch, especially if there were large heterogeneities in bulk electrical conductivity at the TDR measurement scale. A mismatch could have also been caused by errors in the TDR and/or ERT data. Systematic and random errors in the TDR-derived electrical conductivity may have been originated from alterations of the pore space or alterations of the rod spacing during the probe installation (Huisman et al., 2008).

However, detailed studies similar to those presented by Rothe et al. (1997), who investigated the effect of soil compaction on the TDR-derived dielectric constant, are presently not available. For ERT, systematic and random errors in the ERT data could have been caused by, e.g., electrode misplacement. As discussed, we could reduce the misfit between ERT and TDR results significantly by implementing the correct electrode position in the finite-element ERT mesh. We expect further improvement with a finer ERT mesh discretization. In this study, we abstained from this due to computational limitations. Finally, the TDR steel rods could have caused artifacts due to the large electrical conductivity contrast which the TDR rods provide themselves. However, artifact-like features in the vicinity of the TDR probes were visually not observed or did not exceed the range of the bulk electrical conductivity variations in the corresponding cross-section. Therefore, we consider that the effect of the TDR rods on the ERT images is of minor importance. Further investigations of these issues are warranted but exceed the scope of this study.

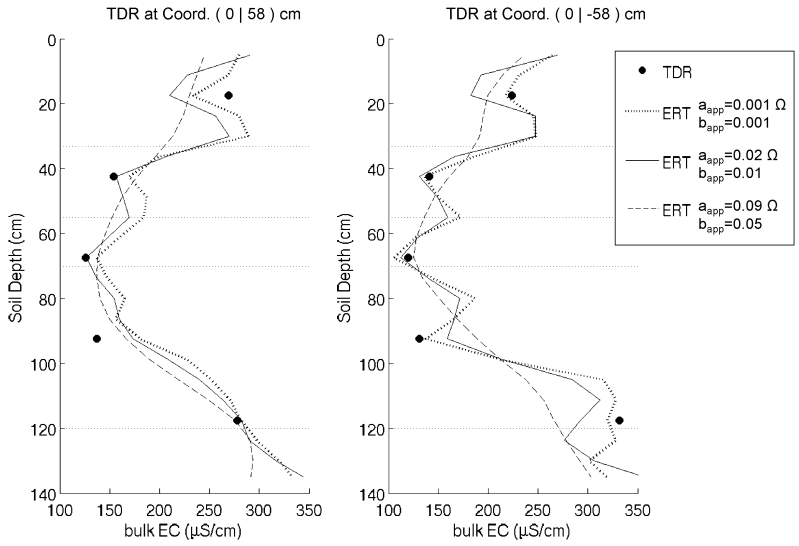


**Figure 2.7: The vertical bulk electrical conductivity profile along the two TDR transects. Next to the TDR data, ERT image data for three different error levels are shown. The ERT data corresponds to the moving average of ERT voxels intersecting an equivalent of the support volume of TDR.**

## 2.4.3. Overshooting values in the ERT image series

For some voxels, the ERT inversion occasionally produced overshooting values (Figure 2.6), i.e. the calculated bulk electrical conductivity values were larger than the ones found when the soil water was in chemical equilibrium with the tracer solution. Such a behavior was not observed in the data from the TDR probes. The overshooting values are hence likely to be related to ERT imaging artifacts. Note that the overshooting values are only observable relative to the ERT-derived bulk electrical conductivity after chemical equilibrium with the tracer had been reached. It can either represent overestimation at the time of the overshoot or underestimation at the time of chemical equilibrium. We suspect that the artifacts reflect how the ERT regularization acts on the reconstructed image for different electrical conductivity gradients. When visually inspecting the location of the overshooting values we could not find any systematics connected to their occurrence.

### 2.4.4. Chloride concentration images

From Figure 2.8, in which the ERT-derived chloride concentrations for $a_{app} = 0.02\ \Omega$ and $b_{app} = 0.01$ are shown, it can be seen that the tracer front is clearly resolved. The maximal gap between the most advanced and most delayed part of the tracer front during the experiment was approximately 50 cm (see Figure 2.8, day 13). Note that the smoothness constraint in the ERT inversion results in a smooth image of the real tracer front progression. In addition, the spatial resolution is worse and smoothing is more pronounced in the center of the column where the sensitivity is lower than near the column's perimeter where the electrodes are located.

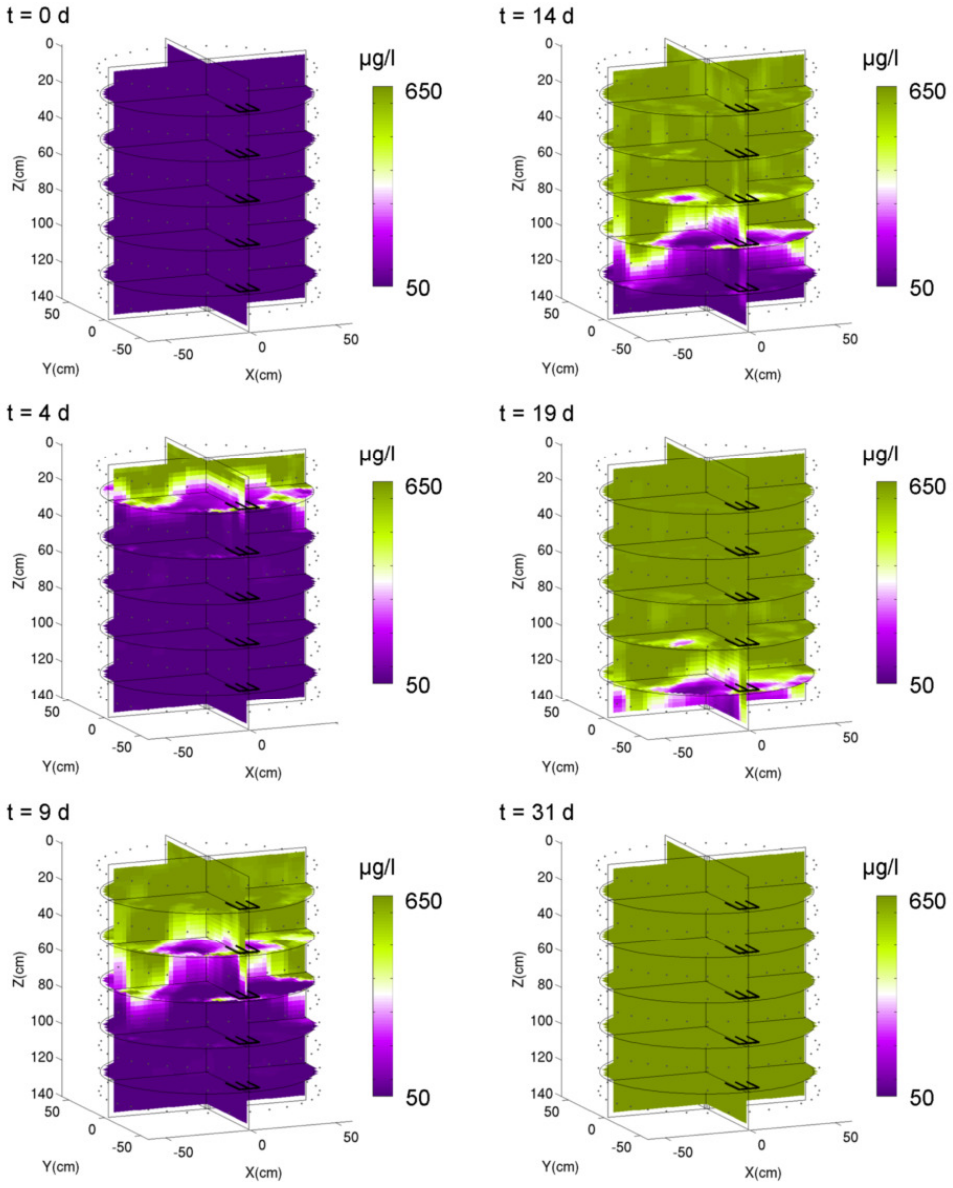


**Figure 2.8: The 3D tracer front progression shown in chloride concentration for $a_{app} = 0.02\ \Omega$ and $b_{app} = 0.01$ ($\varepsilon_{app} \approx 2\varepsilon_{N/R}$).**

### 2.4.5. Comparison of ERT- and TDR-derived chloride concentration

In Figure 2.9, the chloride concentration BTCs for TDR and the mean of the neighboring ERT voxels at depth 42.5 cm are shown. For $\varepsilon_{app} << \varepsilon_{N/R}$ (Figure 2.9, top), the BTCs were noisy; for $\varepsilon_{app} >> \varepsilon_{N/R}$ (Figure 2.9, bottom), the ERT response did not exceed the TDR response. However, the dispersion of the tracer front is larger when measured with ERT data than when based on TDR data. Again, the mid section of Figure 2.9 depicts $\varepsilon_{app} \approx 2\varepsilon_{N/R}$. Here, a good match between TDR and mean voxel ERT BTCs can be observed.

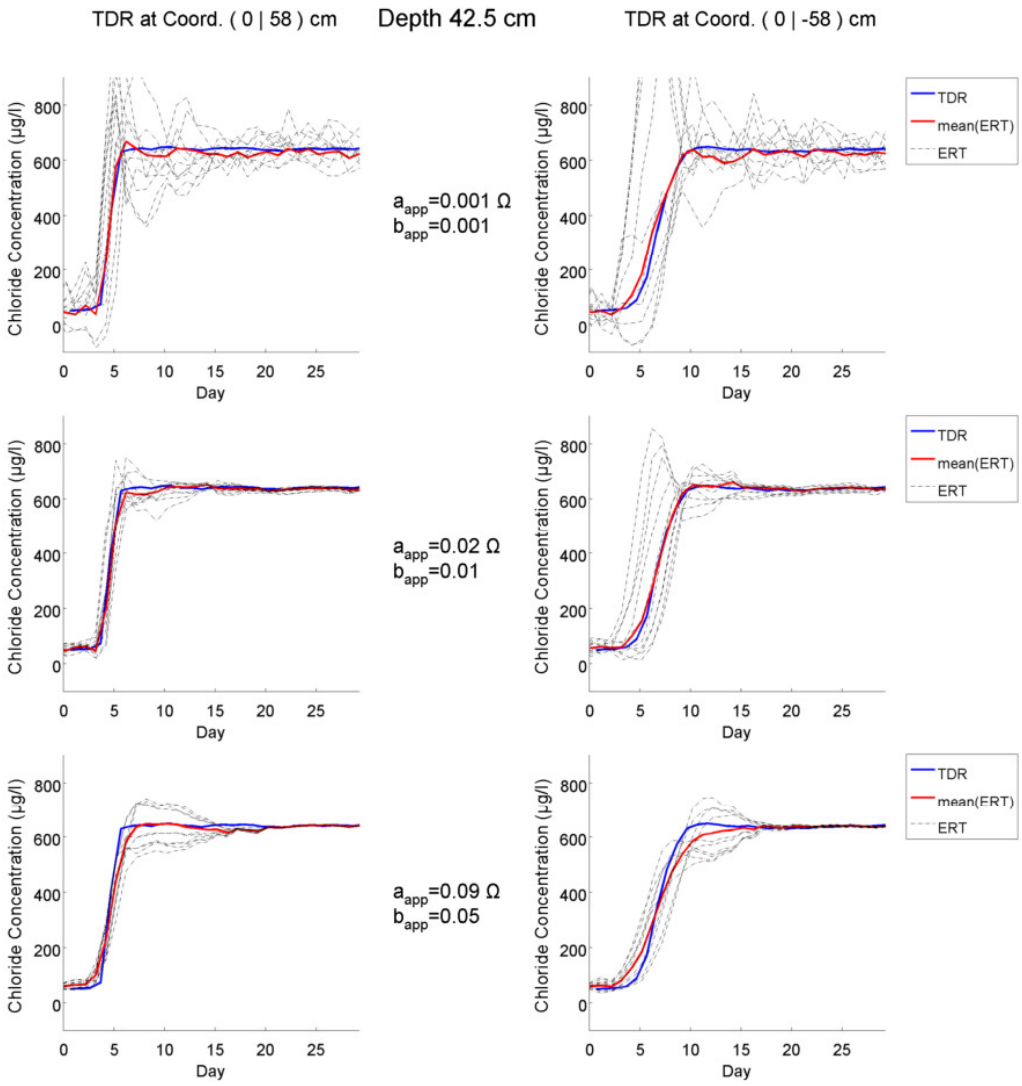


**Figure 2.9: TDR chloride concentration BTCs at depth 42.5 cm compared with the mean ERT voxel BTC in vicinity to the corresponding TDR probe locations. Additionally, the corresponding individual voxel BTCs are depicted. The impact of the ERT inversion error level on the results is shown for three examples: $\varepsilon_{app} << \varepsilon_{N/R}$ (top), $\varepsilon_{app} \approx 2\varepsilon_{N/R}$ (middle) and $\varepsilon_{app} >> \varepsilon_{N/R}$ (bottom).**

### 2.4.6. Comparison of apparent CDE parameters from ERT and TDR chloride BTCs

Figure 2.10 shows the apparent velocities of TDR and mean voxel ERT BTCs. It shows that the solute was traveling faster at the TDR probes at the XY coordinates (0 | 58) than at the XY coordinates (0 | -58). It can be seen that the apparent velocity is relatively insensitive to $\varepsilon_{app}$. Using $\varepsilon_{app} \approx 4\ \varepsilon_{N/R}$ results in the best match between ERT and TDR (Table 2.3). For this ERT error level, the mean residual is below 0.1% (standard deviation 1.6%). Note that the residuals listed in Table 2.3 are valid only for regions with similar ERT sensitivity as the one at the TDR locations. The accuracy of ERT is expected to worsen with increasing distance to the column walls.

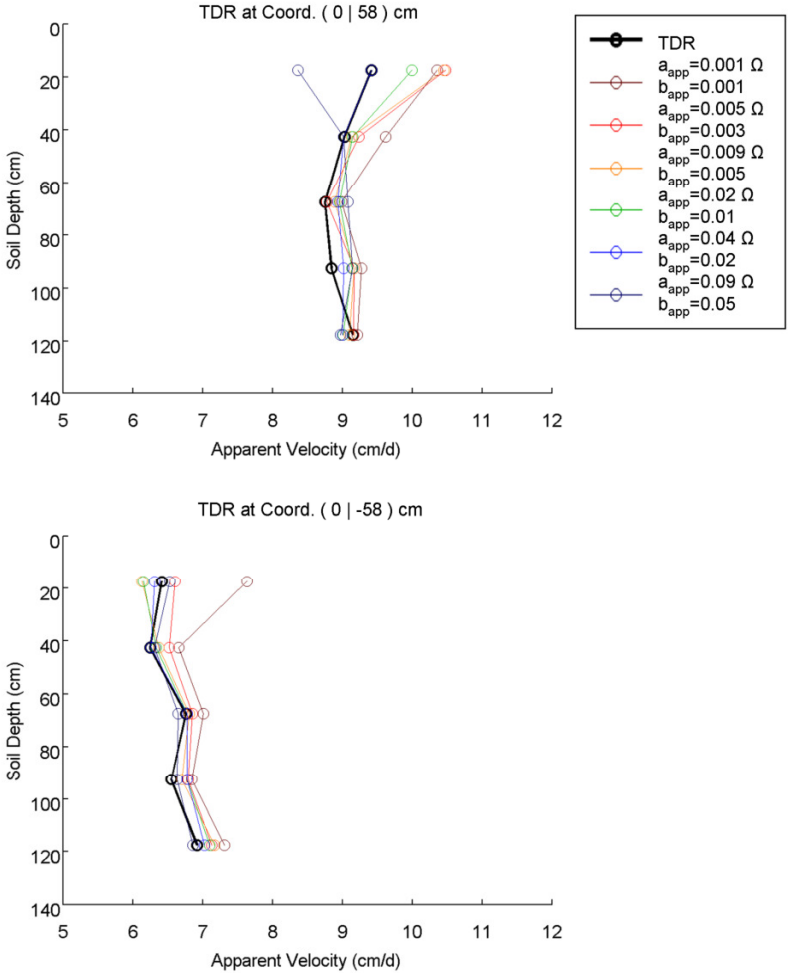


**Figure 2.10: Apparent velocities $v_a$ (cm/d) from TDR and the corresponding mean of the ERT voxel BTCs as a function of $\varepsilon_{app}$.**

The ERT-derived apparent dispersivities, in contrast, are strongly dependent on the choice of $\varepsilon_{app}$ (Figure 2.11). This is also apparent from visual inspection of the BTCs (Figure 2.9). For $\varepsilon_{app} \approx \varepsilon_{N/R}$, the apparent dispersivities are, on average, overestimated by 17.5% (Table 2.3). The largest precision was obtained for $\varepsilon_{app} \approx 2\varepsilon_{N/R}$ (standard deviation of the residuals 26.8%).

**Table 2.3: Mean and standard deviation of residuals between ERT- and TDR-derived apparent velocity ($Rd_v$) and apparent dispersivity ($Rd_\lambda$) at all TDR probe locations as a function of the error level $\varepsilon_{app}$ which constitutes itself by the absolute error $a_{app}$ (Ω) and the relative error $b_{app}$ (%). The best fits are highlighted.**

| $a_{app}$ (Ω) | $b_{app}$ (-) | corresponding to | mean($Rd_v$) (%) | std($Rd_v$) (%) | mean($Rd_\lambda$) (%) | std($Rd_\lambda$) (%) |
|---|---|---|---|---|---|---|
| 0.001 | 0.001 | $\varepsilon_{app} << \varepsilon_{N/R}$ | 6.4 | 5.1 | 18.3 | 60.8 |
| 0.005 | 0.003 | $\varepsilon_{app} \approx \varepsilon_{N/R}/2$ | 3.3 | 3.1 | 18.6 | 54.1 |
| 0.009 | 0.005 | $\varepsilon_{app} = \varepsilon_{N/R}$ | 2.1 | 3.9 | 17.5 | 43.2 |
| 0.02 | 0.01 | $\varepsilon_{app} \approx 2\varepsilon_{N/R}$ | 0.2 | 2.8 | 19.0 | 26.8 |
| 0.04 | 0.02 | $\varepsilon_{app} \approx 4\varepsilon_{N/R}$ | 0.1 | 1.6 | 42.3 | 40.7 |
| 0.09 | 0.05 | $\varepsilon_{app} >> \varepsilon_{N/R}$ | 0 | 4.2 | 117.0 | 74.0 |

The overestimation of the apparent dispersivities can be explained due to the effect of the smoothness constraint in the ERT inversion (Kemna et al., 2002; Vanderborght et al., 2005). Additionally, as the solute moved approximately 3 cm on average during one ERT snapshot, temporal smearing should support an overestimation of apparent dispersivities (Slater et al., 2002; Vanderborght et al., 2005).

Like the apparent velocities, dispersivities differ in magnitude between the two TDR transects at the XY coordinates (0 | 58) and (0 | -58). For the error levels $\varepsilon_{app} \approx \varepsilon_{N/R}$ and $\varepsilon_{app} \approx 2\varepsilon_{N/R}$ the difference in magnitude is recovered by ERT. For these error levels, the shapes of the dispersivity depth profiles are recovered best if both transects are considered.

The ERT image-derived apparent velocities are estimated well regardless of the choice of $\varepsilon_{app}$**,** whereas for a good estimation of the apparent dispersivities the error level $\varepsilon_{app}$ is important. This suggests that investigations on the optimal error level $\varepsilon_{app}$ can be undertaken by means of the misfit between TDR- and ERT-derived apparent dispersivities.

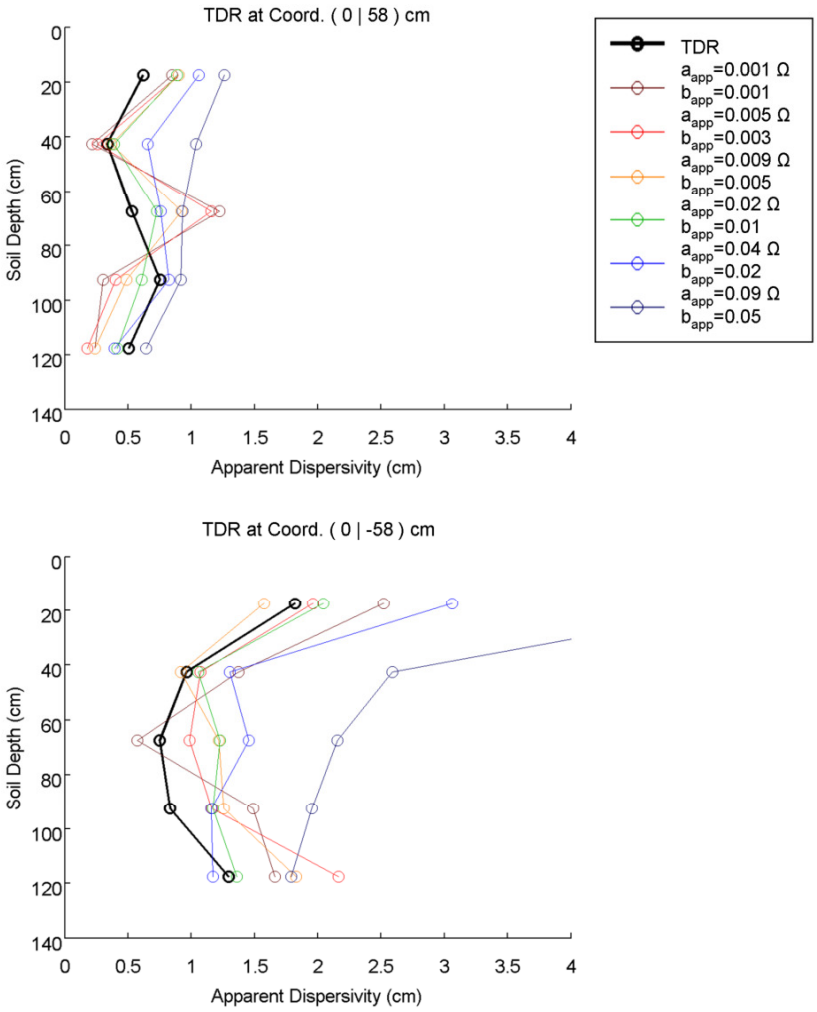


**Figure 2.11: Apparent dispersivities $\lambda_a$ (cm) from TDR and the corresponding mean of the ERT voxel BTCs as a function of $\varepsilon_{app}$.**

## 2.4.7. Comparison of apparent CDE parameters from ERT and effluent chloride BTCs

The 1-D apparent velocity determined from the effluent data and the one derived from the mean of all BTCs in the bottommost ERT voxels match almost perfectly (Table 2.4). Except for overly smooth inversions ($\varepsilon_{app} >> \varepsilon_{N/R}$), the misfit is less than 2% with respect to the effluent data (Table 2.4).

The good match in 1-D apparent velocity suggests that the ERT chloride BTCs recovered the bulk chloride mass correctly, at least at the bottom of the column. We draw this conclusion as the integral over the effluent BTC and the integral over 1-D ERT BTC at the bottom of the column yield an identical mass. This is supported by the fact that we scaled the ERT voxel BTCs to the correct minimum and maximum chloride concentrations.

**Table 2.4: Residuals between ERT- and effluent BTC-derived apparent velocity ($Rd_v$) and dispersivity ($Rd_\lambda$) as a function of the error level $\varepsilon_{app}$ which constitutes itself by the absolute error $a_{app}$ (Ω) and the relative error $b_{app}$ (%). The best fits are highlighted.**

| $a_{app}$ (Ω) | $b_{app}$ (-) | corresponding to | $Rd_v$ (%) | $Rd_\lambda$ (%) |
|---|---|---|---|---|
| 0.001 | 0.001 | $\varepsilon_{app} << \varepsilon_{N/R}$ | 0.5 | 22.3 |
| 0.005 | 0.003 | $\varepsilon_{app} \approx \varepsilon_{N/R}/2$ | 1.7 | 28.7 |
| 0.009 | 0.005 | $\varepsilon_{app} = \varepsilon_{N/R}$ | 1.5 | 30.3 |
| 0.02 | 0.01 | $\varepsilon_{app} \approx 2\varepsilon_{N/R}$ | 1.3 | 31.4 |
| 0.04 | 0.02 | $\varepsilon_{app} \approx 4\varepsilon_{N/R}$ | 0.8 | 27.7 |
| 0.09 | 0.05 | $\varepsilon_{app} >> \varepsilon_{N/R}$ | 3.9 | 4.3 |

The deviations between the ERT- and effluent-derived apparent dispersivities are in the range of the ones we observed in the comparison with the TDR data (4% for $\varepsilon_{app} >> \varepsilon_{N/R}$ to 31% for $\varepsilon_{app} \approx 2\varepsilon_{N/R}$). The ERT-derived dispersivity is exclusively smaller than the dispersivity found in the effluent BTC. The opposite would be expected due to the smoothness constraint in the ERT inversion.

A possible explanation is that boundary effects and decreased sensitivity lead to artifacts in the bottommost ERT voxels as they were located outside the electrode array. Apart from this, the water collection system at the outlet of the column might have generated additional dispersion to the effluent BTC.

An alternative intuitive explanation of why the ERT-derived dispersivity overestimates the TDR-derived one but underestimates the dispersivity in the effluent BTC is depicted in Figure 2.12. In this Figure a schematic of the tracer transport inside the soil column conceptualized with stream tubes is shown for illustration purpose. Within each stream tube (local scale), the tracer is transported with different velocity. At each local-scale tracer front, a BTC is shown which represents the local-scale dispersivity. At the local scale, the smoothness-constrained ERT recovers the travel depth correctly (and hence the transport velocity) but overestimates the dispersivity (dashed line). This is what we observed when comparing TDR- and ERT-derived BTCs and what was also found by Vanderborght et al. (2005). At the column scale, the smoothness-constrained ERT is expected to underestimate the travel depth variability and hence the stream-tube velocity variability (dotted line). The stream-tube velocity variability, however, is positively correlated with a dispersivity component which is generated above the local scale (e.g. Jury and Roth, 1990). This dispersivity component would be underestimated. If in our case this is the dominant contribution to the column-scale dispersivity, this would explain why ERT underestimated the latter. Theoretically, this hypothesis could be investigated by means of TDR. However, in our study this was not possible as the TDR probes sampled only regions with similar and high ERT sensitivity.

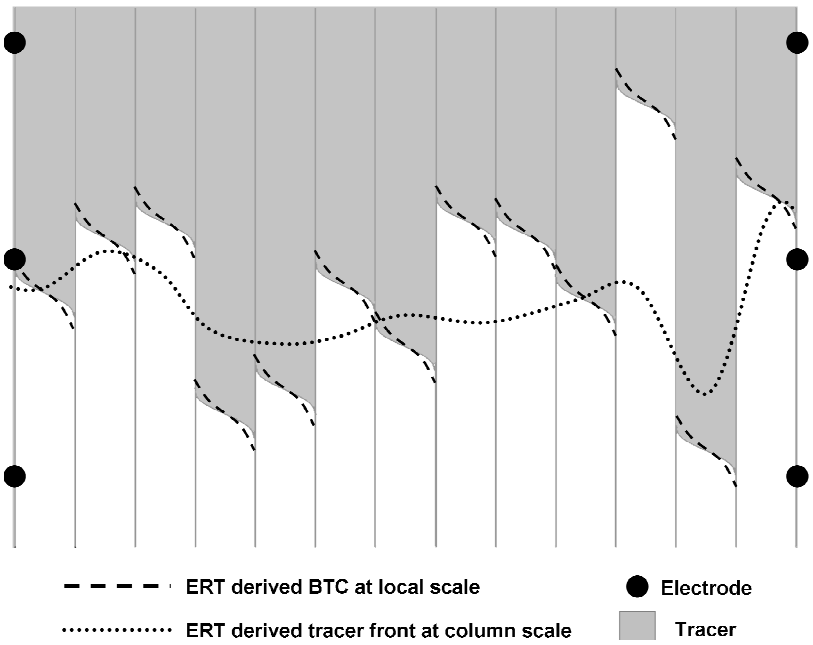


**Figure 2.12: Schematic vertical cross-section through the soil column illustrating how smoothness-constrained ERT is expected to image the local-scale and the column-scale BTC.**

## 2.5. Summary and Conclusion

We have presented a detailed study on some basic issues in the general application of ERT to quantify solute transport parameters in unsaturated undisturbed soils.

The experimental setup which we used in this study allowed us to directly translate bulk electrical conductivity to solute concentration without *a priori* knowledge of the petrophysical properties of the soil material. A drawback of the approach is that it is only applicable when the following conditions are met: (i) hydraulic steady state conditions; (ii) no spatial variation of the soil water solute concentration exists for at least two solute saturation states in the entire domain of the column. Applications of the approach at the field scale are possible, however, large efforts would be needed to meet the necessary conditions (e.g. large amount of water and time). This renders the approach more appropriate for laboratory column-scale studies.

We did not observe mass balance problems when using ERT, as reported in e.g. Singha et al. (2005). We suspect that this is connected with (i) the application of the tracer as a step which is homogeneously distributed over the entire upper boundary of the investigated domain; (ii) the location of the electrodes at the vertical boundaries of the investigated domain; (iii) the improved sensitivity of ERT within a bounded domain; (iv) the scaling of the bulk electrical conductivity to the minimum and maximum chloride concentration.

We introduced an improved method to quantitatively characterize the noise in the raw ERT data by means of normal and reciprocal measurements. The method is based on the approach of LaBrecque et al. (1996). In our revised approach, noise in the complete range of transfer resistances is sampled (a process that can be easily automated). We found that the reciprocal error $\varepsilon_{N/R}$ decreased with increasing salinity of the soil water, likely due to an improved electrode contact.

The ERT-derived apparent transport velocities matched well with those derived from the TDR and effluent data, and the choice of the error level $\varepsilon_{app}$ was of minor importance. In contrast, the apparent dispersivities were overestimated by ERT in comparison to those determined using the TDR data. The overestimation can be explained by the smoothness constraint used in the ERT inversion, as previously shown in synthetic studies (Kemna et al., 2002; Vanderborght et al., 2005), and temporal smearing given significant data acquisition times relative to the process dynamics. The magnitude of the overestimation was sensitive to the applied error level $\varepsilon_{app}$. The best match was achieved for an error level $\varepsilon_{app}$ which was twice the mean reciprocal error $\varepsilon_{N/R}$. Such an error level has been reported to yield the most reasonable results for smoothness-constrained inversions (LaBrecque et al., 1996).

With respect to the effluent BTC, ERT underestimated the apparent dispersivity for all applied error levels $\varepsilon_{app}$. This is surprising as the smoothness constraint in the ERT inversion should always act in the opposite direction. An explanation could be artifacts in the ERT images or effects of the water collection system at the outlet of the column. An alternative explanation is that smoothness-constrained ERT underestimated the variability of the transport velocity in the individual voxel BTCs located in regions with low sensitivity.

Although we cannot verify the validity of the local-scale ERT-derived apparent transport parameters for the entire column, we wish to point out that the presented approach made it possible to image a solute displacement through an undisturbed natural soil in 3-D in a noninvasive manner with unprecedented quantitative consistency. We are positive that the experimental setup will be useful to investigate impacts of the flow rate on the 3-D solute transport characteristics.

In addition, the results suggest that TDR has high potential to act as a quantitative ground truth for ERT. Furthermore, it may be possible to use TDR data to constrain the ERT inversion process. Ideally, the TDR probes should sample the entire ERT sensitivity range. Note that if ERT and TDR are applied jointly, the TDR probes should be electrically isolated from each other when ERT surveys are conducted. Otherwise, electrical short circuits, e.g. through the TDR multiplexing system, can lead to severe artifacts in the ERT images.

# 3. Imaging Brilliant Blue stained soil by means of electrical resistivity tomography*

## 3.1. Introduction

Numerous studies have confirmed that dye tracer experiments provide spatially highly resolved information on solute transport through the unsaturated zone (e.g. Steenhuis et al., 1990; Wang et al., 2003; Javaux et al., 2006; Kasteel et al., 2007). With the aid of these studies, valuable new insights into the nature of solute transport have been gained. For instance, the dye tracer experiments carried out by Flury et al. (1994) provided convincing evidence that preferential flow and transport is rather the rule than the exception in natural soils.

In transport studies in soils, the food dye Brilliant Blue has been preferably employed due to its low toxicity, good visibility, and relatively high mobility (German-Heins and Flury, 2000). Brilliant Blue is not an inert tracer and its sorption isotherm has often been found to be highly non-linear (Perillo et al., 1998; Ketelsen and Meyer-Windel, 1999; German-Heins and Flury, 2000). Hence, inferences of (preferential) water flow pathways derived from Brilliant Blue images are not straightforward (Perillo et al., 1999; Kasteel et al., 2002). Rather, Brilliant Blue is considered especially useful to infer transport characteristics of contaminants with similar adsorption characteristics (Kasteel et al., 2005).

The studies of Ewing and Horton (1999), Forrer et al. (2000), and Persson (2005) showed that quantification of dye concentration from Brilliant Blue stained soil cross-sections is possible using image analysis techniques. At scales between a few centimeters up to a few meters, dying techniques provide better spatial resolution of solute concentrations in soil than any other current method (Persson, 2005). From the dye staining images solute transport properties of the soil can be inferred (Forrer et al., 1999). However, as the method is destructive, time-lapse dye tracer displacement studies are constrained to 2-D. Yet, in order to fully understand solute displacement through unsaturated soils and its corresponding constituent parameters, a full 3-D spatio-temporal monitoring of the solute plume evolution is needed (Vanderborght et al., 2006). In the laboratory, this can be obtained by means of optical methods if the considered porous medium is transparent, for example if glass beads are used (e.g. Stöhr et al., 2003). Ignoring point-like approaches, like, for example, published in Nielsen et al. (1991), optical methods cannot provide 3-D spatio-temporal resolution of solute displacement experiments in natural soils. However, non-invasive tomographical methods have the potential to provide information of the 3-D spatio-temporal evolution of a solute plume or front leading to the dye staining pattern.

In solution, the Brilliant Blue molecule is predominantly electrically negatively charged for pH values larger than 5.83 (Flury and Flühler, 1995). Under these conditions Brilliant Blue provides an electrical contrast which should be detectable by methods sensitive to an electrical conductivity contrast, provided that Brilliant Blue is applied in sufficiently large concentrations.

---

* adapted from Koestel, J. R. Kasteel, O. Esser, A. Kemna, M. Javaux, A. Binley and H. Vereecken. Imaging of Brilliant Blue stained soil by means of electrical resistivity tomography. Vadose Zone Journal. Accepted for publication.

Binley et al. (1996a) and subsequent studies (for example, Park, 1998; Slater et al., 2002; Singha and Gorelick, 2005; Koestel et al., 2008) showed that electrical resistivity tomography (ERT) can be used to image time varying electrical conductivity contrasts in 3-D. The ERT inversion problem is usually strongly underdetermined. Therefore, the problem has to be regularized in order to reconstruct images from ERT data. Here, a smoothness constraint is commonly applied (e.g. Binley and Kemna, 2005). However, the smoothness constraint is not optimal for imaging sharp electrical conductivity contrasts like they often occur in natural systems. Instead of the smoothness constraint, it appears advantageous to use a regularization which is linked to the spatial characteristics of the target object which is sought to be visualized (e.g., Linde et al., 2006), however, information on these spatial characteristics is seldom available. An additional caveat against stand-alone smoothness-constrained ERT images is that they are prone to specific bias (Friedel, 2003; Day-Lewis et al., 2007) which can lead to mass balance problems (Singha and Gorelick, 2005). Therefore, ERT-image results should preferably be ground-truthed by an independent method.

The joint application of photographical and geoelectric methods for the imaging of Brilliant Blue concentrations offers various potential benefits:

- the optically-derived Brilliant Blue image data are useful to ground-truth the ERT image;
- the 3-D spatio-temporal evolution of the solute plume corresponding to 2-D image-derived Brilliant Blue concentrations can be provided by time-lapse ERT and thus the characterization of solute transport can be improved;
- instead of the smoothness constraint, a constraint derived from the spatial characteristics of the 3-D Brilliant Blue image (e.g. spatial statistics, sharpness of the Brilliant Blue solute plume) can be used for the ERT regularization.

A study in which a dye staining technique was jointly applied with ERT is described in Binley et al. (1996a). They used a Methylene Blue dye to ground-truth their ERT analysis of solute transport in an undisturbed soil column. However, their comparison was purely qualitative and they did not directly image the dye tracer using ERT.

The aim of this study is to show that Brilliant Blue can be used as an electrical tracer. Furthermore, we want to demonstrate the efforts and data needed to quantitatively relate optical and electrical Brilliant Blue images. Finally, a comparison between optically and ERT-derived Brilliant Blue concentrations shall illustrate the potential and limitation of smoothness-constraint ERT to non-invasively image electrical conductivity patterns in undisturbed soil.

In our study, we performed a Brilliant Blue displacement experiment in a zero-potential lysimeter, filled with an undisturbed sandy soil. We derive the Brilliant Blue concentrations from photographic data and compare them with corresponding smoothness-constrained ERT-derived bulk electrical conductivities. We show that the electrical conductivity can be translated to bulk Brilliant Blue concentration using approximations for the petrochemical and petrophysical parameters. Finally, we discuss the results with respect to measurement, approximation, and interpolation errors as well as imaging artifacts.

## 3.2. Theory

### 3.2.1. Modeling the petrophysical relationship

Waxman and Smits (1968) presented an empirical relationship for unsaturated shaly sands

that relates the bulk electrical conductivity, $\sigma_b$ (µS/cm), and solute electrical conductivity, $\sigma_w$ (µS/cm), as follows:

$$\sigma_b = \frac{S^n}{F}\left(\sigma_w + \frac{\sigma_s}{S}\right), \tag{3.1}$$

where $\sigma_s$ (µS/cm) denotes the electrical mineral surface conductivity, $F$ (-) is a formation factor which is defined as

$$F = a\Phi^{-m}, \tag{3.2}$$

where $\Phi$ (cm³/cm³) is the porosity and $a$ (-) and $m$ (-) are empirical parameters which account for the pore network geometry (Archie, 1942). Note that we choose µS/cm as units instead of S/m for convenience. In Eq. (3.1), $S$ (-) is the water saturation of the pore space, relating volumetric water content, $\theta$ (cm³/cm³), and porosity, $\Phi$, according to

$$S = \frac{\theta}{\Phi}, \tag{3.3}$$

and $n$ (-) is an empirical parameter referred to as saturation exponent. The latter is known to be a function of the water saturation history (Lewis et al., 1988; Longeron et al., 1989; Knight, 1991).

Following Eq. (3.1), the bulk electrical conductivity, $\sigma_b$, is a function of variables which are non-constant at time scales relevant for our study (several days). These are the solute electrical conductivity, $\sigma_w$, and the water content, $\theta$. In addition, a dependency of the saturation exponent $n$ on the water saturation history has to be taken into consideration. Based on results of Revil and Glover (1998), we assume no dependency of the electrical surface conductivity, $\sigma_s$, on the solute electrical conductivity, $\sigma_w$, for solute electrical conductivities $\sigma_w < 1000$ µS/cm.

In the following we consider changes in $\sigma_b$ between two observation times, which are subsequently referred to as reference (index '0') and sampling time (index 't'). Here, the change in solute electrical conductivity, $\Delta\sigma_w$, is obtained from the changes in bulk electrical conductivity, $\Delta\sigma_b$, if concomitant changes in water content, $\Delta\theta$, and changes in saturation exponent, $\Delta n$, are quantifiable.

As we investigate changes in electrical conductivity with respect to a reference time, we base the following derivations with respect to the ratio-inversion approach as described by Daily and Owen (1991), which is discussed in more detail in section 3.3.4. Following this approach our inversion of ERT data yields a change in conductivity relative to a homogenous reference model. We refer to it as ratio conductivity, $\sigma_r$ (µS/cm). It is defined as:

$$\sigma_r = \sigma_{\mathrm{hom}} \frac{\sigma_{bt}}{\sigma_{b0}}. \tag{3.4}$$

In Eq. (3.4), $\sigma_{bt}$ (µS/cm) denotes the bulk electrical conductivity at the sampling time ($t$),

$\sigma_{b0}$ (µS/cm) the bulk electrical conductivity at the reference time ($t_0$), and $\sigma_{hom}$ (µS/cm) is the electrical conductivity of a homogeneous reference model, chosen with respect to the considered problem (e.g. 100 µS/cm).

For the reference and sampling times, the petrophysical model in Eq. (3.1) can be written as

$$\sigma_{b0} = G_0\left(\sigma_{w0} + \frac{\sigma_s}{S_0}\right), \tag{3.5}$$

with

$$G_0 = \frac{S_0^{\,n_0}}{F}, \tag{3.6}$$

and

$$\sigma_{bt} = G_t\left[\left(\sigma_{w0} + \Delta\sigma_w\right) + \frac{\sigma_s}{\left(S_0 + \Delta S\right)}\right], \tag{3.7}$$

with

$$G_t = \frac{\left(S_0 + \Delta S\right)^{(n_0+\Delta n)}}{F}, \tag{3.8}$$

respectively.

### 3.2.2. Modeling the Brilliant Blue adsorption

Brilliant Blue adsorbs to mineral surfaces. In soils, the bulk Brilliant Blue concentration, $C_b$ (g/cm$^3$), is composed of Brilliant Blue that is dissolved in the soil water, referred to as $C_w$ (g/cm³), and Brilliant Blue that is adsorbed to the soil matrix, referred to as $C_s$ (g/g):

$$C_b = \rho_b C_s + \theta C_w, \tag{3.9}$$

where $\rho_b$ (g/cm³) is the soil bulk density.

Adsorbed and dissolved Brilliant Blue concentrations are related through the function $f$, the so-called adsorption isotherm, i.e.

$$C_s = f\left(C_w\right). \tag{3.10}$$

Combining Eqs. (3.9) and (3.10), the concentration of the dissolved Brilliant Blue with respect to solute volume, $C_w$, is obtained from the bulk concentration, $C_b$, and the adsorbed concentration, $C_s$, by

$$C_w = \frac{C_b - \rho_b f(C_w)}{\theta}. \tag{3.11}$$

### 3.2.3. Relating changes in dissolved Brilliant Blue concentration to changes in solute electrical conductivity

Brilliant Blue is a polyprotic acid. It has two acid dissociation constants which are $pK_{a1}$=5.83 and $pK_{a2}$=6.58 at 20°C (Flury and Flühler, 1995). Dissolved Brilliant Blue is predominantly negatively charged for pH-values larger than 5.83. The largest Brilliant Blue-related electrical conductivity contrast prevails for pH-values larger than 6.58. In order to quantify the relationship between Brilliant Blue concentration and electrical conductivity, the pH of the soil solution has to be taken into account.

For constant temperature and sufficiently low Brilliant Blue concentrations, the relationship between ion concentration and electrical conductivity of the solution is linear. The relationship between the dissolved Brilliant Blue concentration and the corresponding change in solute electrical conductivity ($\Delta\sigma_w$) can be expressed as

$$\Delta\sigma_w = \gamma C_w, \tag{3.12}$$

where $\gamma$ (µScm²/g) is a proportionality factor which depends on the pH of the solution. Note that Eq. (3.12) is only valid if the pH remains constant.

### 3.2.4. Relating changes in bulk Brilliant Blue concentration to the ratio electrical conductivity

In order to relate changes in bulk Brilliant Blue concentration to the ratio electrical conductivity, we subtract Eq. (3.5) from Eq. (3.7), then we incorporate Eqs. (3.4), (3.9), and (3.12), and finally solve for $C_b$. As result we obtain

$$C_b = \frac{\theta_t \sigma_{b0}}{\gamma G_t}\left(\frac{\sigma_r}{\sigma_{\text{hom}}} - 1\right) + \frac{\theta_t}{\gamma G_t}\left(\sigma_{w0}(G_0 - G_t) + G_0 \frac{\sigma_s}{S_0} - G_t \frac{\sigma_s}{S_0 + \Delta S}\right) + \rho_b C_s. \tag{3.13}$$

In Eq. (3.13) the first term on the right-hand side relates changes in bulk electrical conductivity to bulk Brilliant Blue concentration, the second term corrects for changes in the saturation exponent $n$ due to hysteresis and for changes in water saturation, both with respect to the reference time. The last term corrects for adsorbed Brilliant Blue.

If changes in water saturation and saturation exponent can be considered negligible, Eq. (3.13) simplifies to

$$C_b = \frac{\theta \sigma_{b0}}{\gamma G}\left(\frac{\sigma_r}{\sigma_{\text{hom}}} - 1\right) + \rho_b C_s \,. \tag{3.14}$$

## 3.3. Materials and Methods

### 3.3.1. Experimental Setup and Schedule

The experiment was carried out on a lysimeter (diameter = 116 cm, height = 140 cm; Figure 3.1b) containing an undisturbed sandy soil (Gleyic Cambisol) taken from the Kaldenkirchen field site (Germany). The soil is horizontally layered with sharp contrasts in soil color between adjacent soil horizons, especially at 30 and 120 cm depth (Figure 3.1a). The soil texture published in Pütz and Klimsa (1991) is listed in Table 3.1.

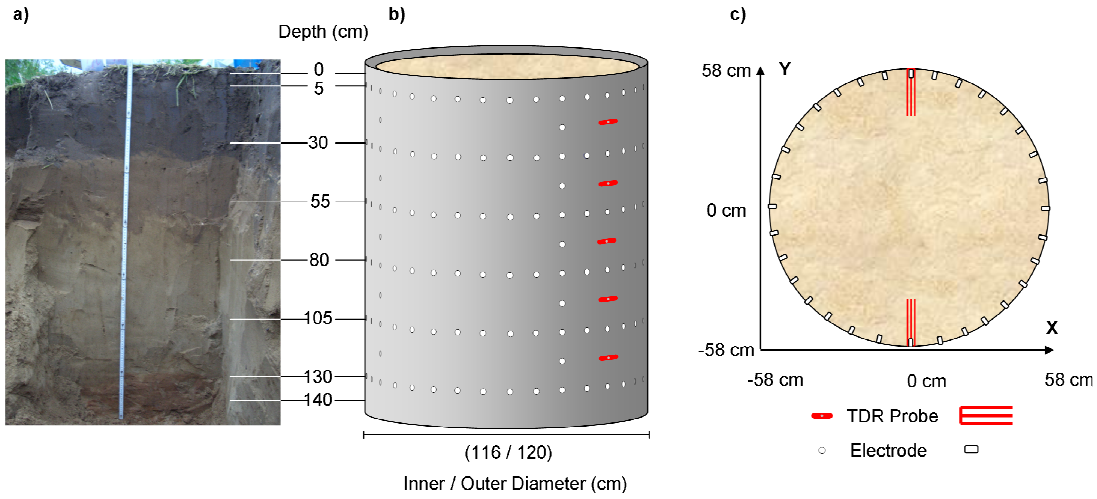


**Figure 3.1: (a) Vertical soil profile at the Kaldenkirchen field site. The location of the six electrode rings with respect to the soil horizons are indicated; (b) the soil column with the locations of electrodes and TDR probes; (c) a horizontal cross-section through the lysimeter. Electrode and TDR probe locations are depicted.**

**Table 3.1: Soil horizons and grain size distribution of the Kaldenkirchen soil according to Pütz and Klimsa (1991). The texture classes correspond to the classification system commonly used in Germany.**

| Horizon | Soil Depth | Sand (%)<br>67 – 2,000 µm | Silt (%)<br>2 - 67 µm | Clay (%)<br>< 2 µm |
|---|---|---|---|---|
| Ap | 0-33 cm | 72.7 | 22.2 | 5.5 |
| Bv1 | 33-55 cm | 76.6 | 21.4 | 2.0 |
| Bv2 | 55-70 cm | 79.1 | 19.7 | 1.2 |
| Bv3 | 70-120 cm | 84.3 | 14.3 | 1.0 |
| IIBv | > 120 cm | 49.0 | 40.7 | 10.3 |

The lysimeter was equipped with 10 TDR probes (3 rods, 18.8 cm rod length; 2.5 cm rod spacing) which were installed in two vertical transects at depths of 17.5, 42.5, 67.5, 92.5, and 117.5 cm (Figure 3.1b and c). Additionally, 212 stainless steel electrodes (1.2 cm in diameter; 5 cm length, extending 3 cm into the soil) were inserted into the soil column for ERT measurements (Figure 3.1b and c). TDR and ERT measurement devices are documented in chapter 4.2. The ERT survey design (skip-1 dipole-dipole; 37,428 measurements, including reciprocals) was identical to the one described in chapter 4.2 used for a tracer displacement experiment with a steady irrigation rate of 6.5 cm/d. The dipole-dipole array was chosen because it is an ERT array that provides higher spatial resolution as compared to other ERT arrays (e.g. Sasaki, 1992).

The lysimeter was located in a basement at the Research Center Jülich, Germany. At the sampling time, the ambient temperature was 14.2 °C, at the reference time it was 9.3 °C. In the following, we converted all electrical-conductivity data to an equivalent conductivity corresponding to a temperature of 20 °C using the relationship published in Franson (1985).

Hydraulic steady state flow was imposed by using an irrigation device which distributed the irrigation water through 484 needles over the lysimeter's upper surface. The coefficient of variation of the spatial water distribution was found to be 17% - 20% during test runs prior to the experiment. The irrigation rate was adjusted to 6.5 cm/d. At first, tap water with electrical conductivity of 455 µS/cm (20 °C) and a pH of 7.9 (22 °C) was irrigated until hydraulic steady-state conditions were established. Subsequently, the tap water was replaced by a Brilliant Blue solution of a concentration of 2.5 mg/cm³. Here, tap water was used to prepare the Brilliant Blue solution resulting in an electrical conductivity of 756 µS/cm (20 °C). After 72.5 hours of dye application, the irrigation was switched back to tap water. Another 53 hours later the irrigation was stopped in order to prevent complete staining of the bottommost soil layers. After the irrigation had been stopped for 46 hours, the soil in the lysimeter was removed layer-wise. In the process, photographs of the stained cross-sections, Brilliant Blue concentration samples (10 per sampling depth), and Kopecky-cylinder (100 cm³ steel cylinders) samples (6 per sampling depth) were collected (see Figure 3.2). The sampling depths are listed in Table 3.2.

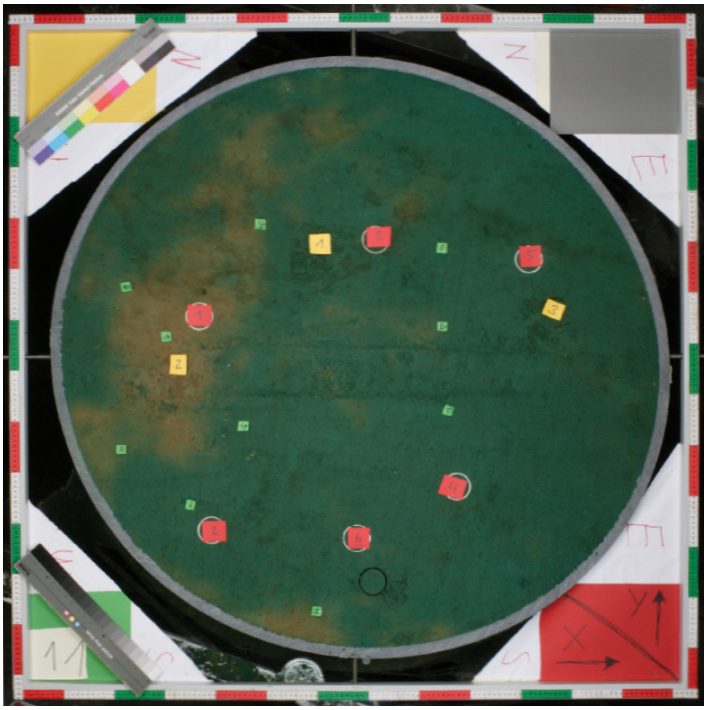

**Figure 3.2: Photograph of the cross-section at depth 99 cm. The labels were applied to mark the location of the Brilliant Blue samples (green), the Kopecky-cylinder samples (red), and texture samples (yellow). The latter were not analyzed for this study.**

**Table 3.2: Soil depths where photographs, Brilliant Blue samples and Kopecky-cylinder samples were available.**

| Soil Depth (cm) | Brilliant Blue Samples | Kopecky-cylinder Samples |
|---|---|---|
| 2 | X | X |
| 12 | | |
| 20 | X* | X |
| 30 | X | X |
| 37 | X | |
| 44 | X | X |
| 54 | X | |
| 66 | | |
| 79 | X | X |
| 91 | X | |
| 99 | X | X |
| 108 | X | |
| 118 | X | X |
| 129 | X | |
| 135 | X | X** |
| 138 | | |

* only 6 Brilliant Blue samples available
** only 2 Kopecky cylinders available

We chose the reference time as such that the water content (or water saturation) was as similar as possible to the one at the sampling time. Accounting for the redistribution of the water after the irrigation stop, we selected a dataset that had been collected just before the Brilliant Blue experiment when the soil column was draining from a previous irrigation experiment with tap-water irrigation of a rate of also 6.5 cm/d. We used the TDR-derived water contents to compare the water contents at reference and sampling time. In between both observation times, the soil column had gone through a drying-wetting-drying sequence, which evokes hysteresis.

### 3.3.2. 1-D approximation of relevant petrophysical and petrochemical parameters and state variables

In order to constrain the parameterization of our petrophysical and petrochemical relationships, we assume that a multitude of relevant parameters are approximately constant within horizontal cross-sections. The assumption is justified by the distinct horizontal layering of the soil (Figure 3.1a). In the vertical, we discretized these parameters according to the horizontal cross-sections at which Brilliant Blue photographs were obtained.

#### 3.3.2.1 Petrophysical data obtained from TDR and the Kopecky-cylinder samples

The 1-D water content profile, $\theta_z$, was obtained by means of TDR data using a dielectric mixing model. Its parameterization is documented in Koestel et al. (2008). Here, we took the average of each of the two moisture contents obtained from TDR probes which were installed at each depth. For depths without TDR probes the water content was linearly interpolated whereas we set the water content at the bottommost 5 cm of the soil column to the saturated water content which was measured by means of the Kopecky-cylinder samples. The layers above the uppermost TDR probe (17.5 cm) were not considered. In between reference and sampling time, the soil column experienced a drying-wetting-drying sequence. The span between minimum and maximum water content in the soil column during this period is denoted as $\Delta\theta_{Span,z}$ and is subsequently used as a qualitative proxy for hysteresis.

Similarly, we interpolated the bulk electrical conductivity at the reference time, $\sigma_{b0}$, which was obtained from the TDR signal attenuation using the calibration relationship published in Koestel et al. (2008). Additionally, the TDR-derived ratio electrical conductivity $\sigma_{r,TDR}$ was calculated using Eq. (3.4).

The 1-D bulk density, $\rho_{b,z}$, and porosity, $\Phi_z$, approximations were obtained from the dried Kopecky-cylinder samples. We took the average of each of the six Kopecky-cylinder samples within corresponding depths. For depths without Kopecky-cylinder samples the bulk density and porosity were linearly interpolated. The 1-D water saturation at the reference time, $S_{0,z}$, and the change in water saturation between reference and sampling time, $\Delta S_z$, were calculated from the 1-D water content, $\theta_z$, and porosity, $\Phi_z$, profiles.

#### 3.3.2.2 Petrochemical data obtained from laboratory measurements on soils and water samples

The adsorption isotherm was estimated with aid of batch experiments which were available for soil samples (approximately 24 g each) taken from three different depths, namely 15 cm, 45 cm, and 90 cm. The soil samples were immersed for two days with Brilliant Blue solutions covering a concentration range between $1\times10^{-7}$ and $2.5\times10^{-2}$ g/cm³.

Afterwards, the Brilliant Blue concentration in the supernatant, $C_w$, was measured photometrically using light of a wavelength of 629.5 nm. Then, we obtained the respective adsorbed concentration, $C_s$, directly from the total concentration. The adsorption isotherms for the three soil depths were modeled by means of an appropriate adsorption isotherm (see section 4.2). In order to obtain a depth profile of the adsorption characteristics, we assume that the adsorption isotherm taken from 15 cm is representative for the topmost soil layer (0 - 33 cm), the one taken from 45 cm for the soil horizon between 33 and 55 cm, and the isotherm corresponding to 90 cm is representative for the depths 55 - 120 cm. A distinct soil horizon boundary is located at 120 cm depth. Beneath this depth, the clay content is considerably larger (see Table 3.1), which implies an increased affinity to adsorption. Due to the lack of data on the adsorption isotherm from these depths, we do not interpret Brilliant Blue data from depths below 120 cm.

The coefficient $\gamma$, which is defined in Eq. (3.12), is pH dependent. As we lacked pH data during the Brilliant Blue experiments we constrained the range of possible $\gamma$ values by measuring the change in electrical conductivity for solutions covering the range of Brilliant Blue concentrations and pH considered in our study. The measurements were conducted for two different values of pH, namely pH 6.1 and pH 7.9. The latter pH is that of the tap water used. The pH 6.1 corresponds to a 0.01 molar $CaCl_2$ solution. It is also the minimal pH that was previously measured in the effluent for all experiments conducted on the soil column. We assume that the pH was never below this value during the experiment.

### 3.3.3. Brilliant Blue sampling and image processing

3.3.3.1. Brilliant Blue sampling

After the irrigation had been stopped for 46 hours, the soil in the lysimeter was removed layer by layer and 16 horizontal cross-sections were prepared for photography (see Figure 3.2). The photographs were taken with a digital camera (Canon EOS Mark II Ds) using a Canon lens of type ES 35 mm 1:14 L. The images were saved in TIF format with a resolution of approximately 16 dots per cm. (40.6 dpi).

The camera was positioned centrally at 160 cm above the respective soil layers, except for the bottommost 4 cross-sections where the distance between camera and soil surface could not be maintained for technical reasons. Here, the distance between the camera and the profile face increased incrementally for each new photographed cross-section up to 180 cm. In order to supply homogeneous illumination, 4 headlights (Multiblitz Ministudio 802) were positioned around the cross-section. Additionally, a white tent was placed above the camera and headlights to minimize the impact of sunlight. For all photographs, a quadratic metal frame with glued on measuring tapes was attached to the lysimeter. This enabled us to check and correct for spatial distortions in the images.

At 13 of the 16 horizontal cross-sections 10 soil samples (126 in total) of approximately 5 g were taken in order to analyze the dye concentration (Figure 3.2). The locations were marked with (green) pieces of paper (see Figure 3.2) and another photograph was taken in order to relate staining intensity to dye concentration. The complete sampling campaign lasted 2 days.

3.3.3.2. Brilliant Blue laboratory analysis

In the laboratory, Brilliant Blue was first extracted from the soil samples with a water-acetone solution (mixing ratio 4:1) as described in Forrer et al. (2000). Then, the Brilliant Blue concentration in the extracted solution was measured photometrically using light with a wavelength of 629.5 nm. In a next step, the bulk Brilliant Blue concentration, i.e., the

mass of Brilliant Blue per mass of soil, $C^{\#}_{b,samples}$ (g/g), was converted to mass of Brilliant Blue per volume of soil, $C_{b,samples}$ (g/cm³), by means of

$$C_{b,samples} = C^{\#}_{b,samples} \rho_{b,z} \,. \tag{3.15}$$

3.3.3.3. Brilliant Blue image correction

In order to quantitatively evaluate the spatially resolved dye concentration from the photographs, we followed the approach published by Forrer et al. (2000). Firstly, geometric distortions were checked with aid of the measuring tapes on the metal frame and were found to be negligible (Figure 3.2). In the next step we corrected the images for inhomogeneous illumination following Forrer et al. (2000). This was done by translating the image from RGB (red, green, blue) color space to HSV (hue, saturation, value) color space (see, for example, Russ, 1995). As we could not rely on a grey board, we used the HSV V-value of the green and yellow paper labels which had been used to mark sample locations (Figure 3.2). Afterwards, the images were translated back to RGB color space.

3.3.3.4. Regression analysis between soil color and Brilliant Blue concentration

We applied a single calibration relationship to relate the staining intensity at the Brilliant Blue sampling locations to the corresponding Brilliant Blue concentration. Like Forrer et al. (2000), we used the image's RGB values and the soil depth as explanatory variables. The soil depth was included in the regression analysis as our soil is horizontally layered and, thus, the depth can be used as a proxy for the background soil color.

In order to obtain the RGB values, we first collected all pixels located within a square of approximately 2.5 by 2.5 cm (50 by 50 pixels) around the center of the individual sampling location. Like Forrer et al. (2000), we calculated the 20% trimmed mean for each RGB value in order to minimize the impact of outliers. RGB values and depth were then standardized to zero mean and unit variance.

Following Forrer et al. *(*2000), the regression analysis was performed by fitting the logarithm to the base of 10 of the Brilliant Blue concentration per volume of bulk soil, $C_b$, to a second-order polynomial using the standardized explanatory variables.

In the next step, the calibration relationship was applied to the photographs which were converted into maps of bulk Brilliant Blue concentrations $C_b$. For this step we imposed the maximum concentration found for the calibration set as an upper threshold. Additionally, all apparent concentrations which were lower than the maximum concentration of the unstained samples in the calibration set were set to zero (see Kasteel et al., 2005).

Next, each photograph was rotated until it matched the ERT coordinate system. Then the image resolution was reduced to 1200 by 900 pixels in total in order to decrease the image noise and to shorten computation time. After this, one centimeter corresponded to approximately 5 pixels (12.7 dpi), except for the bottommost 4 cross-sections where the distance between camera and soil surface was greater than for the upper layers. Here, the resolution was slightly reduced. Finally, a median filter with a footprint of 4 x 4 pixels was applied to further reduce image noise.

### 3.3.4. ERT image reconstruction

For ERT data inversion we used a converted resistance, referred to as ratio resistance, $R_r$, which is given by Daily and Owen (1991):

$$R_r = \frac{R_t}{R_0} R_{\mathrm{hom}}. \qquad (3.16)$$

$R_t$ (Ω) is the transfer resistance measured shortly before the Brilliant Blue sampling time, $R_0$ (Ω) is the transfer resistance measured at the reference time and $R_{hom}$ (Ω) is the forward model response for the given electrode configuration for a virtual analogue of the lysimeter with a homogeneous electrical conductivity of 100 µS/cm.

The inversions were performed with the smoothness-constrained inversion code described in Binley et al. (1996b) which is based on a triangular prism finite element discretization. The inversion algorithm makes use of the option to conduct robust inversions by means of iterative data re-weighting (LaBrecque and Ward, 1990). In order to account for data and modeling errors we applied a simple Gaussian error model for data weighting (Slater et al., 2000) which consists of an absolute ($a_{app}$=0.02 Ω) and a relative ($b_{app}$=0.5 %) error component. The error model parameters were estimated on basis of the reciprocal error analysis described in Koestel et al. (2008).

The ERT inversion yields an image of the ratio electrical conductivity, $\sigma_r$, which is related to the bulk electrical conductivity, $\sigma_{bt}$, briefly before the Brilliant Blue sampling and the one at reference time, $\sigma_{b0}$, as described in Eq. (3.4). The 1-D profile of the electrical conductivity, $\sigma_{r,z}$, is calculated by the areas weighted average of all $\sigma_r$ voxels at each horizontal cross-section.

### 3.3.5. Parameterization of the relationship between $C_b$ and $\sigma_r$

It is our aim to translate the ERT-derived ratio electrical conductivity, $\sigma_r$, to the photographically-derived bulk Brilliant Blue concentration, $C_b$, using Eq. (3.13). In order to achieve this we applied the 1-D approximations derived from the Kopecky-cylinder samples ($\rho_{b,z}$, $\Phi_z$), TDR probes ($\sigma_{bo,z}$, $\theta_{t,z}$), and both ($S_{0,z}$, $\Delta S_z$). The adsorbed Brilliant Blue concentration, $C_s$, was obtained from the optically derived bulk Brilliant Blue concentration, $C_b$, using the adsorption isotherm $f$ as well as Kopecky-cylinder and TDR data (Eqs. 3.9 and 3.10).

For a parameterization of Eq. (3.13), the following yet missing six parameters were also approximated as 1-D parameters: $a_z$; the cementation exponent $m_z$; the saturation exponent $n_{0,z}$ at the reference time; its change $\Delta n_z$ due to hysteresis; the coefficient $\gamma_z$; the mineral surface electrical conductivity $\sigma_{s,z}$. Then, the six missing parameters were found by comparing the image data of the photographically-derived bulk Brilliant Blue concentration, $C_b$, and ERT-derived ratio electrical conductivity, $\sigma_r$. Here, we spatially discretized both, the $C_b$ and the $\sigma_r$ images into square-shaped bins with an edge length of 8 cm. This corresponds approximately to the horizontal cross-section of one finite element which was used for the ERT inversion (66 cm²). To each of the bins, the 20%-trimmed mean of all Brilliant Blue and ERT-image pixels within each corresponding bin was assigned. In this way we achieved an identical spatial sampling for both types of images.

In the following we carried out a Monte Carlo analysis (42,905 realizations) sampling the parameter space of Eq. (3.13) ($a_z$, $m_z$, $n_{0,z}$, $\Delta n_z$, $\gamma_z$, and $\sigma_{s,z}$) using $\sigma_r$ and $C_b$ of the square-shaped bins. The limits for $a_z$, $m_z$, ($n_{0,z}$ + $\Delta n_z$), and $\sigma_{s,z}$ were chosen according to the values

published in (Schön, 1998) for unconsolidated materials. They are listed in Table 3.3. The limits for $\gamma_z$ were determined in the laboratory as described above.

**Table 3.3: The limits put on the parameter space for the Monte-Carlo analysis which was carried out to parameterize Eq. (3.13).**

| Parameter | Lower Limit | Upper Limit |
|---|---|---|
| $a_z$ (-) | 0.7 | 1.5 |
| $m_z$ (-) | 1.1 | 2.1 |
| $n_{0,z} + \Delta n_z$ (-) | 1.0 | 2.6 |
| $\Delta n_z$ (-) | -0.5 | 0 |
| $\gamma_z$ (µScm²/g) | 7.4e4 | 1.1e5 |
| $\sigma_{s,z}$ (µS/cm) | 0 | 50 |

We used the parameter combination for which the objective function at depth $z$, $OF_z$ (%),

$$OF_z = \frac{\sqrt{\Sigma\left(C_{b,ERT,i} - C_{b,i}\right)^2}}{NC_{b,z}} 100 \qquad \textbf{(3.17)}$$

was minimal to translate the ERT-derived $\sigma_r$ images to bulk Brilliant Blue concentration. In Eq. (3.17), $C_{b,ERT,i}$ and $C_{b,i}$ denote ERT and photographically-derived bulk Brilliant Blue concentration of bin $i$, respectively. $C_{b,z}$ is the average bulk Brilliant Blue concentration at depth $z$ and $N$ is the number of bins within the cross-section at depth $z$.

The parameter combination minimizing $OF_z$ is subsequently discussed and the optically and electrically derived Brilliant Blue images are compared. Figure 3.3 gives an overview of the data sources and data processing steps carried out in our study.

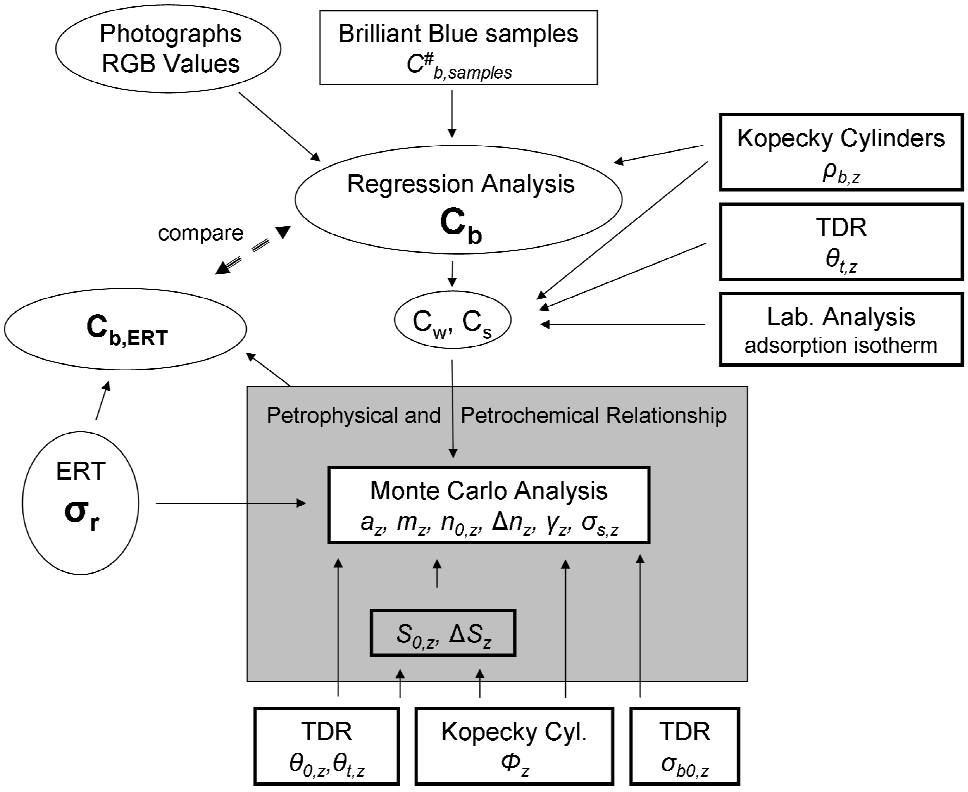


**Figure 3.3: Schematic illustrating the data sources and data processing steps in this study. The bold square frames indicate point-like data which was interpolated to a 1-D approximation of the 3-D distribution of the respective parameter or state variable. The oval frames denote spatially resolved data.**

## 3.4. Results and Discussion

### 3.4.1. Petrophysical parameters and state variables

The water contents, $\theta$, for the reference and sampling time are depicted in Figure 3.4 for the two TDR transects. The large water content variations in the vertical were predominantly caused by the seepage face at the bottom boundary condition. The water content discrepancies between the two TDR probes installed at one depth were in the range of 0.02 $cm^3/cm^3$, except for the depth of 92.5 cm (moisture content mismatch equals 0.05 $cm^3/cm^3$). We conclude that the assumption of horizontally homogeneous water content is justified. The water saturation mismatch between the reference and sampling time, $\Delta S_z$, was small and did not exceed ±0.007 (Table 3.4). We assume that $\Delta S$ was also approximately constant in the horizontal direction.

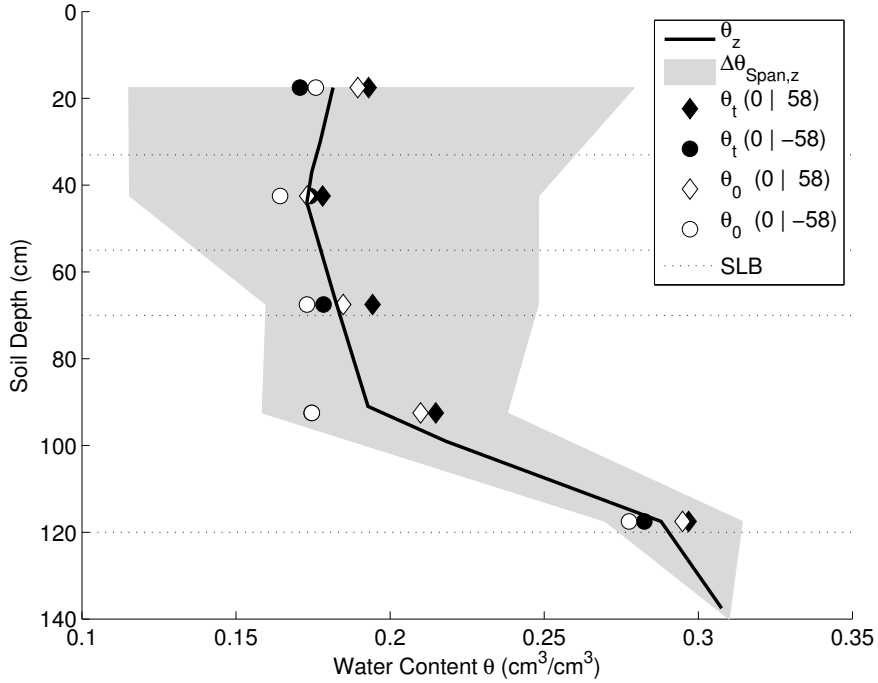


**Figure 3.4: The average TDR-derived water content $\theta_z$ profile at the reference (subscript *0*) and sampling time (subscript *t*) is depicted. The data of the two vertical TDR transects, at XY-coordinates (0 | 58) and (0 | -58) cm are shown separately. Additionally, the span between minimum and maximum water content in the meantime between reference and sampling time is shown (grey). SLB stands for soil layer boundary.**

**Table 3.4: The TDR-derived change in water saturation and the bulk electrical conductivity at the reference time.**

| Soil Depth (cm) | $\Delta S_z$ (cm³/cm³) | $\sigma_{b0,z}$ (µS/cm) |
|---|---|---|
| 17.5 | -0.002 | 35.4 |
| 42.5 | 0.007 | 22.7 |
| 67.5 | 0.006 | 19.1 |
| 92.5 | 0.003 | 19.5 |
| 117.5 | 0.003 | 42.3 |

The span between minimum and maximum water content in the soil column in the meantime between reference and sampling time, $\Delta\theta_{Span,z}$, is depicted Figure 3.4. $\Delta\theta_{Span,z}$ indicates that hysteresis in the saturation exponent $n$ may be an issue for almost the entire soil column (Figure 3.4).

The bulk electrical conductivity at the reference time, $\sigma_{b0,z}$, is listed in (Table 3.4). It is positively correlated with the water content (Figure 3.4).

The bulk density, $\rho_b$, and the porosity, $\Phi$, which were derived from the Kopecky cylinders are depicted (Table 3.5). The respective standard deviations (from the six samples in one depth) are small (Table 3.5), which justifies the 1-D approximation of the three parameters.

**Table 3.5: Sampling depth, mean and standard deviation of the Kopecky-cylinder-derived porosity, $\Phi$, and bulk density, $\rho_b$.**

| Soil Depth (cm) | mean $\Phi$ ($cm^3/cm^3$) | std $\Phi$ ($cm^3/cm^3$) | mean $\rho_b$ ($g/cm^3$) | std $\rho_b$ ($g/cm^3$) |
|---|---|---|---|---|
| 2 | 0.39 | 0.03 | 1,59 | 0,08 |
| 20 | 0.40 | 0.02 | 1,61 | 0,07 |
| 30 | 0.40 | 0.01 | 1,62 | 0,03 |
| 44 | 0.36 | 0.01 | 1,66 | 0,03 |
| 79 | 0.40 | 0.01 | 1,60 | 0,02 |
| 99 | 0.36 | 0.01 | 1,66 | 0,03 |
| 118 | 0.33 | 0.01 | 1,72 | 0,03 |
| 135 | 0.31 | 0.01 | 1,85 | 0,02 |

### 3.4.2. Adsorption characteristics of the Kaldenkirchen soil with respect to Brilliant Blue

We used the Langmuir-Freundlich isotherm to describe Brilliant Blue adsorption:

$$f(C_w) = S_{\max} \frac{K_l C_w^{\beta}}{1 + K_l C_w^{\beta}}, \tag{3.18}$$

where $S_{max}$ (g/g) is the maximally adsorbed Brilliant Blue concentration, $K_l$ ($g^{1-\beta}cm^{3\beta}/g$) is the distribution coefficient and $\beta$ (-) is a fitting parameter which can be regarded as a heterogeneity factor (Hinz, 2001).

Figure 3.5 illustrates that the Langmuir-Freundlich isotherm adequately describes the adsorption characteristics for the two-day equilibrium. The adsorption in the topsoil representing soil depths between 0 - 33 cm is significantly larger than that at greater depths. The adsorption characteristics of the soil samples taken from 45 and 90 cm depth are almost identical. Therefore we describe the adsorption between 33 and 120 cm depth with one single isotherm. The parameterizations of the isotherms are listed in Table 3.6.

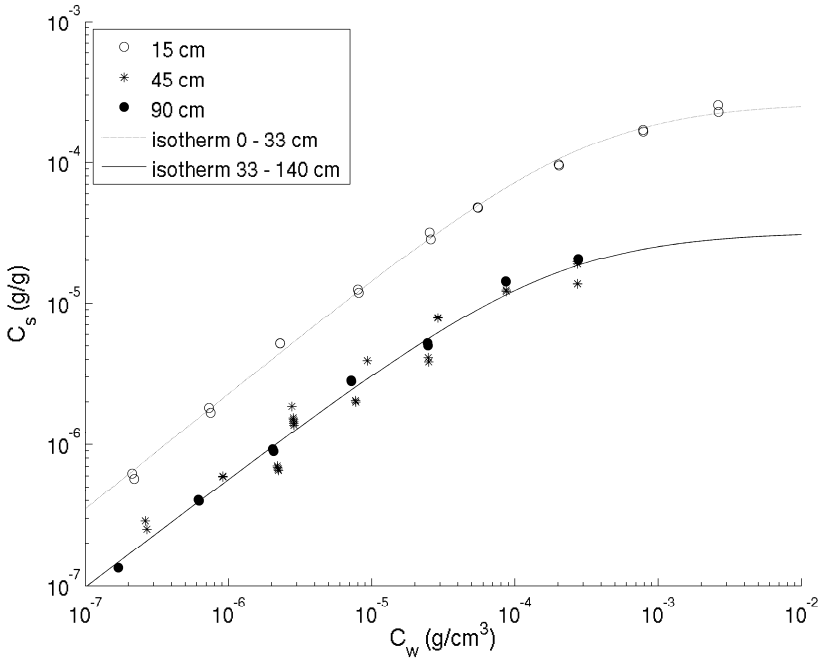


**Figure 3.5: Brilliant Blue adsorption isotherms together with the corresponding Langmuir-Freundlich isotherms.**

**Table 3.6: The parameterization of the Langmuir-Freundlich isotherms.**

| Parameter | Soil Depth 0 – 33 cm | Soil Depth 33 – 120 cm |
|---|---|---|
| $S_m$ (g/g) | 2.6e-4 | 3.1e-5 |
| $K_l$ ($g^{1-\beta}cm^{3\beta}/g$) | 691 | 724 |
| $\beta$ (-) | 0.82 | 0.77 |

### 3.4.3. Relationship between $C_w$ and $\Delta\sigma_w$

Figure 3.6 shows that the relationship between $C_w$ and $\Delta\sigma_w$ is linear for both, dissolved Brilliant Blue in tap water buffered with $CaCl_2$ (pH 6.1, temperature = 20 °C) and pure tap water (pH 7.9, temperature = 20 °C). Consistently with the Brilliant Blue dissociation properties, the slope $\gamma$ is smaller for the buffered solution. Note that the pH for the unbuffered solution (pure tap water) gradually decreased with increasing Brilliant Blue concentration from the pH of tap water (7.9) to 7.3 (20 °C).

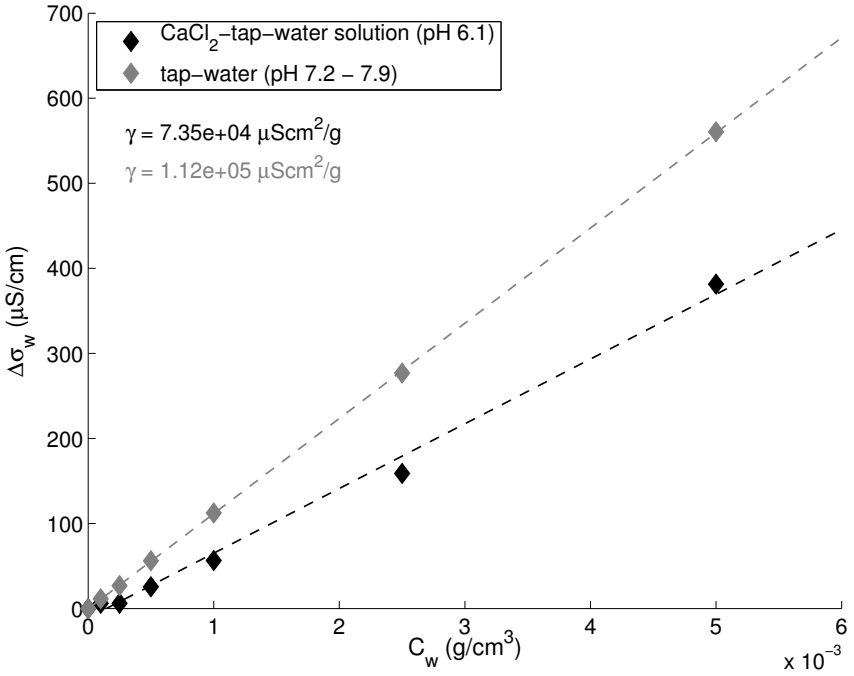


**Figure 3.6: Relationship between the dissolved Brilliant Blue concentration, $C_w$ , and the change in electrical conductivity, $\Delta\sigma_w$ (with respect to a background value), for two different pH.**

### 3.4.4. Photographically-derived bulk Brilliant Blue concentration $C_b$

The following regression relationship fitted the calibration data with a coefficient of determination, $R^2$, of 0.931 and a mean squared error (*MSE*) of 0.035 ($\log_{10}(g/cm^3)^2$):

$$\log_{10}(C_b) = -0.474 - 0.276R + 0.037G - 0.095R^2 + 0.113B^2 - 0.082z^2 + 0.102RG - 0.104GB. \quad \textbf{(3.19)}$$

In Eq. (3.19), R, G, and B stand for the red, green, and blue values in the RGB color space, respectively. The resident Brilliant Blue mass inside the lysimeter was calculated by means of two different methods: (i) from the mass balance and (ii) from the 1-D bulk Brilliant Blue concentration profile (Figure 3.7). The mass balance yielded a resident mass of 416.1 g, as the cumulative mass which had been irrigated is 479.6 g and the cumulative mass in the effluent is 63.5 g. The resident mass that was derived from the 1-D bulk Brilliant Blue concentration profile by means of the trapezoidal rule was 376 g. This corresponds to 90.4 % of the resident mass calculated by means of the mass balance. This is in the range of mass recoveries published in similar studies (Javaux et al., 2006; Kasteel et al., 2007).

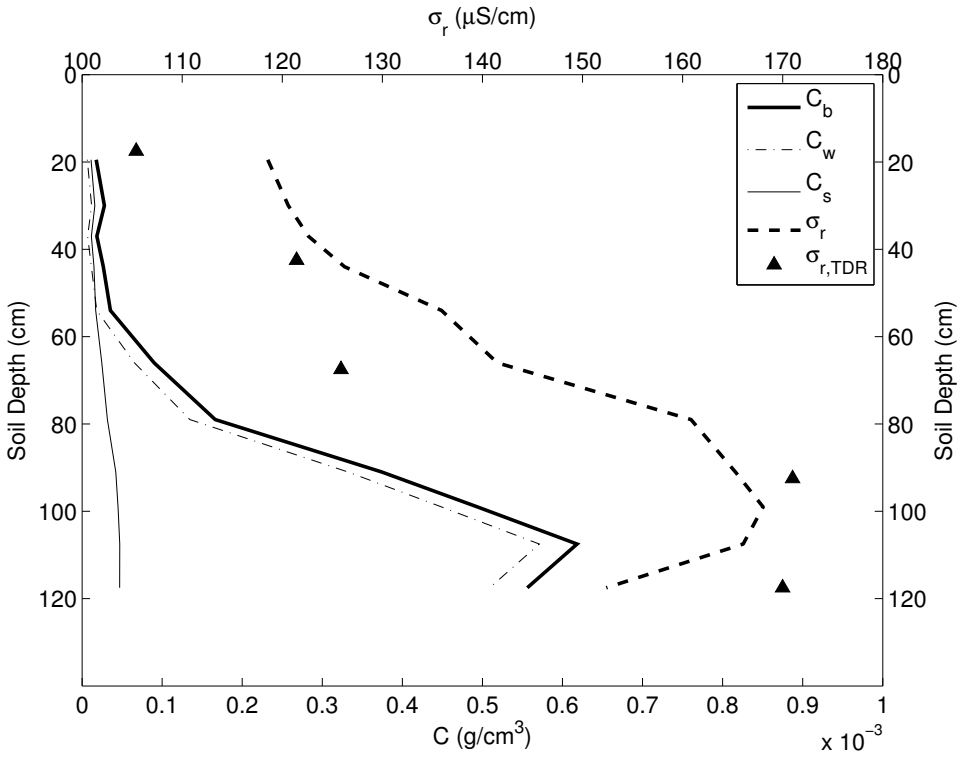


**Figure 3.7: 1-D profiles of the dissolved, adsorbed, and bulk Brilliant Blue concentration are depicted. Additionally, the 1-D ratio electrical conductivity profiles as derived by ERT and TDR are shown. Note that in this figure, $C_w$ and $C_s$ are calculated with respect to bulk soil volume.**

Down to a depth of 55 cm the bulk Brilliant Blue concentration $C_{b,z}$ was smaller than $5\times10^{-5}$ g/cm³ (Figure 3.7). Here, the Brilliant Blue is in equal parts dissolved and adsorbed. Below 55 cm, the bulk Brilliant Blue concentration increases strongly and the dissolved phase becomes more and more dominant. This is a consequence of the non-linear adsorption characteristics of Brilliant Blue (Figure 3.5).

### 3.4.5. ERT-derived ratio electrical conductivity $\sigma_r$ and $\sigma_{r,z}$

The ERT data could be fitted to the target error level in the ERT inversion. As an example, a horizontal cross-section of the ratio electrical conductivity, $\sigma_r$, is depicted in Figure 3.8b. The corresponding 1-D profile of the ratio electrical conductivities, $\sigma_{r,z}$, follows the Brilliant Blue profile (Figure 3.7). The TDR-derived ratio electrical conductivity, $\sigma_{r,TDR}$, confirms the 1-D ERT-derived $\sigma_{r,z}$ (Figure 3.7).

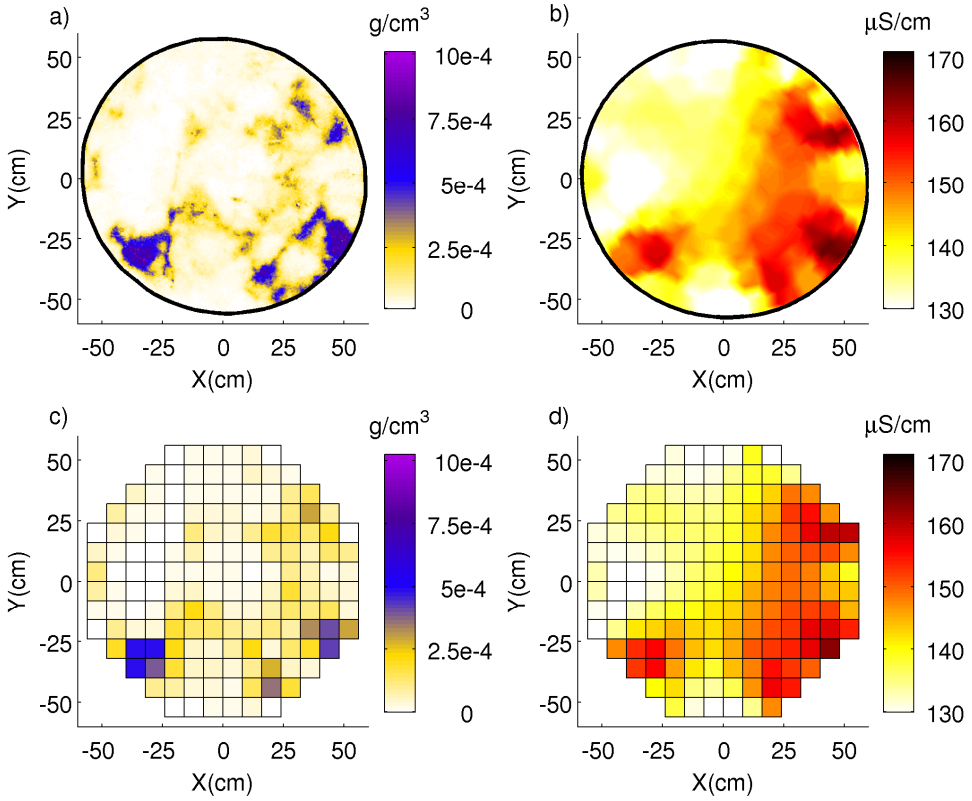


**Figure 3.8: (a) The photographically derived bulk Brilliant Blue concentration in the cross-section at a depth of 66 cm and (b) the corresponding ratio electrical conductivity are shown. The images below (c) and (d) show the same data but with the resolution that we used to parameterize the petrophysical relationship.**

### 3.4.6. Investigating the relationship between $C_b$ and $\sigma_r$

In this section, we present the results of the Monte-Carlo analysis and subsequently apply the parameter set that minimized Eq. (3.17) to translate the ratio electrical conductivity to bulk Brilliant Blue concentration. For illustration purpose, Figure 3.8 (a and b) shows the photographically-derived Brilliant Blue concentration, $C_b$, and the ERT-derived ratio electrical conductivity, $\sigma_r$, at a depth of 66 cm. Similarity between dye staining and electrical conductivity patterns is clearly discernable. The bottom part of Figure 3.8 (c and d) shows the identical data but with the spatial resolution used to parameterize Eq. (3.13).

Figure 3.9 shows the relative misfit between ERT-derived and photographically-derived bulk Brilliant Blue concentration, $OF_z$, for the best fit and the misfit range of the best 50 fits. Except for the topmost cross-section where the signal-to-noise ratio is worst, the misfit is smaller than 50%. Below a depth of 66 cm, the best 50 parameter combinations fit the data equally well. Above this depth, the minimum of the objective function, Eq. (3.17), is better defined.

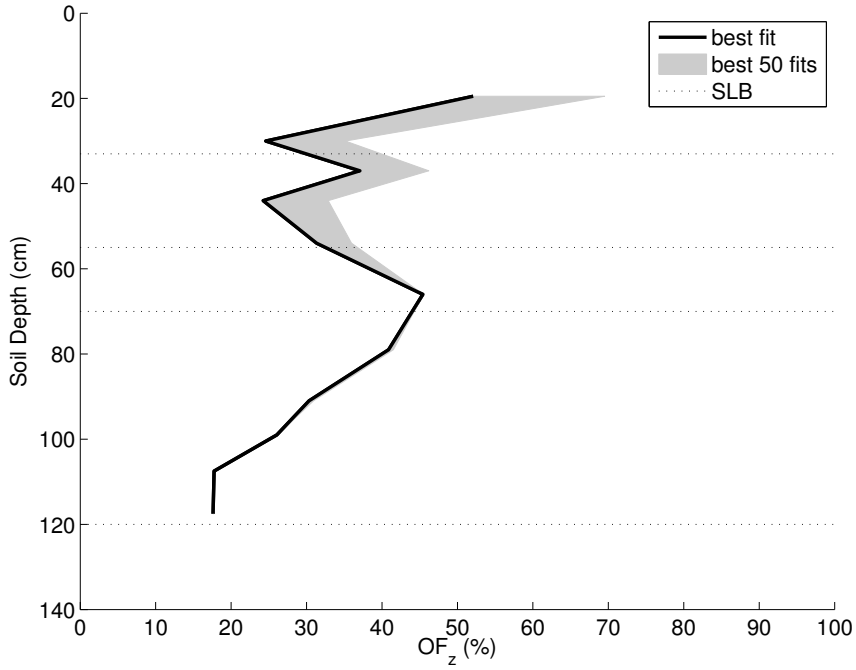


**Figure 3.9: The misfit between ERT-derived and photographically-derived bulk Brilliant Blue concentration for the best fit and the misfit range of the best 50 fits are depicted. SLB stands for soil layer boundary.**

In Figure 3.10, the photographically-derived and sampled bulk Brilliant Blue concentration is plotted against the ratio electrical conductivity. In addition, the petrophysical relationship with the parameter set that yielded the smallest $OF_z$ is shown. The relationship between both quantities is approximately linear for the uppermost 54 cm or 66 cm. At these depths, Eq. (3.13) describes the data well. For larger depths, the linearity breaks down more and more until the petrophysical relationship cannot describe the photographically-derived Brilliant Blue concentrations anymore (Figure 3.10, depths 91cm and 108 cm).

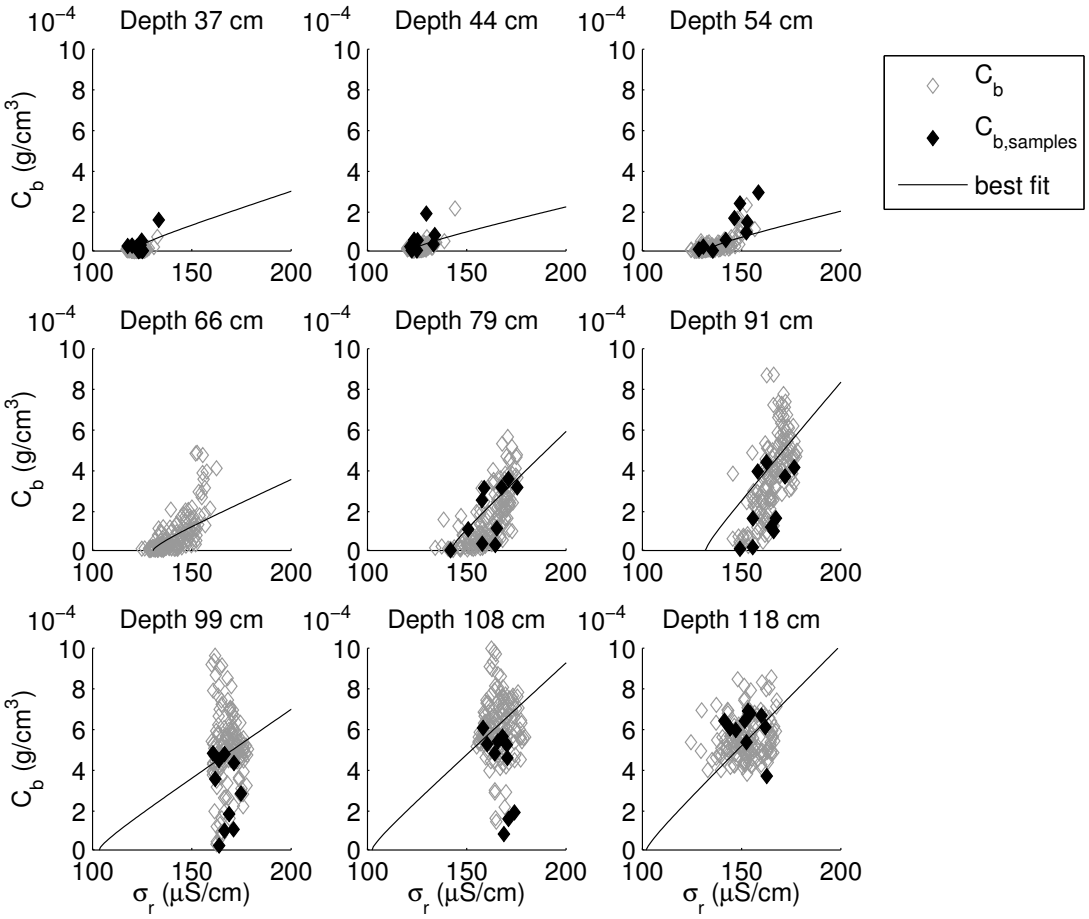


**Figure 3.10: The ERT-derived ratio conductivity versus the photographically-derived (grey diamonds) and sampled (black diamonds) bulk Brilliant Blue concentration for 9 depths. The black line represents the parameterization of Eq. (13) which fitted the data best.**

Figure 3.11a-c also shows that the petrophysical parameters leading to the 50 smallest $OF_z$ are better constrained for the topmost soil layers (depths 20 - 54 cm). Here, $\alpha_z$ is varying between 0.7 and 1.1, $m_z$ between 1.1 and 1.5, and $n_{0,z}$ between 1.1 and 1.6 which are the ranges that are reported in the literature for unconsolidated sandy material (Schön, 1998). $\Delta n_z$ is in an order of magnitude as observed by Knight (1991) (between -0.15 and -0.05, Figure 3.11d). The presence of hysteresis in the saturation exponent in the topmost soil layers appears reasonable in the light of the large water content variations between reference and sampling time, $\Delta\theta_{Span,z}$ (Figure 3.4). From 66 cm downwards, $\alpha_z$ and $m_z$ are not constrained anymore. The saturation exponent $n_{0,z}$ increases strongly for depths 66 – 91 cm (maximum 2.6) and the change in saturation exponent, $\Delta n_z$, follows $n_{0,z}$ inversely until the lower parameter limit is reached (-0.5). We consider the latter value to be unrealistically small, in particular as we may expect an even smaller hysteresis effect for these depths than in the topsoil (see $\Delta\theta_{Span,z}$, Figure 3.4). In this light, the large saturation exponents, $n_{0,z}$, in these depths also appear questionable. Below the depth of 91 cm, $n_{0,z}$ drops again to minimal values and the corresponding $\Delta n_z$ becomes approximately 0.

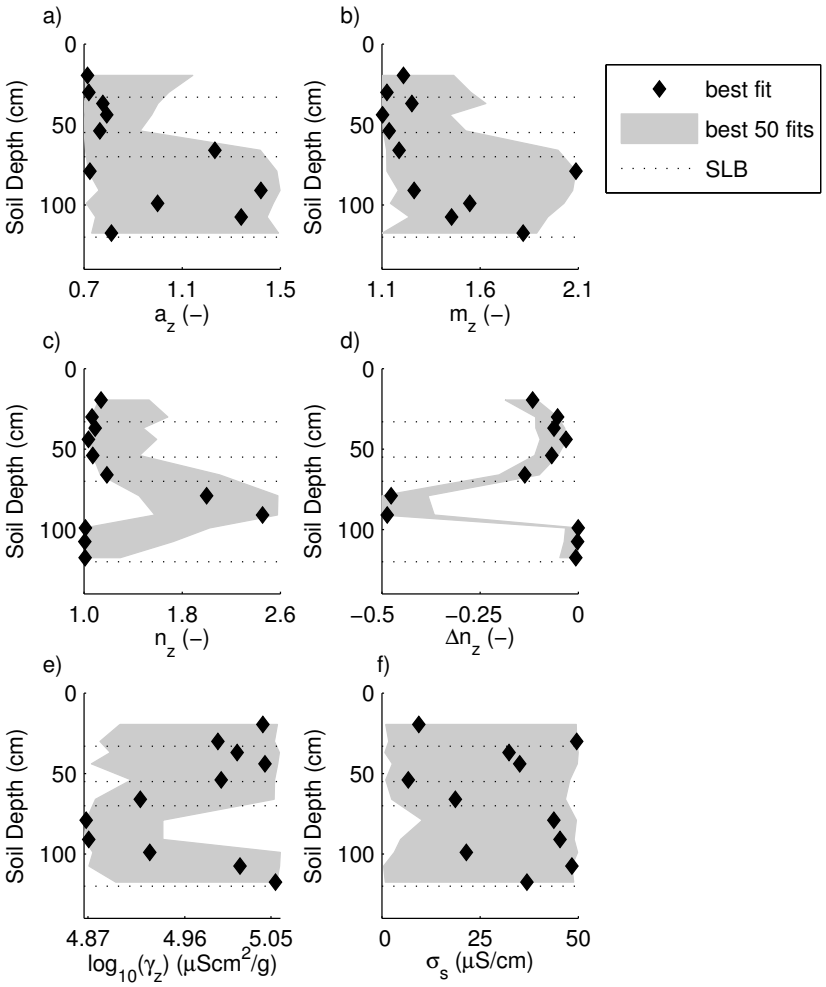


**Figure 3.11: The results of the Monte-Carlo analysis that was carried out to parameterize Eq. (13) are shown. The diamonds depict the parameter set that fitted the data best; the grey shading illustrates the range of each parameter for the 50 best fits. SLB stands for soil layer boundary.**

The petrochemical parameter, $\gamma_z$ (Figure 3.11e), is not constrained, which suggests that the pH-dependency of the Brilliant Blue solution's electrical conductivity was of minor importance for the considered range of pH. Exceptions are the depths 66 - 91 cm where the questionable saturation exponent values are found, which in turn casts doubts on the validity of $\gamma_z$ in these depths. Finally, the results of the Monte-Carlo analysis show that $OF_z$ is also not sensitive to the mineral surface electrical conductivity, $\sigma_s$ (Figure 3.11f). The latter is therefore considered not important to relate $C_b$ and $\sigma_r$ in our study.

Figure 3.12 shows horizontal cross-sections of photographically (left) and ERT-derived (right) bulk Brilliant Blue concentrations using the best parameterizations of Eq. (3.13) (see Figure 3.10). For the depths of 66 cm and 79 cm, ERT provides a strongly smoothed image of the photographically-derived Brilliant Blue concentration but recovers the main features of the dye stained soil. For the depths below (depths 91 cm 108 cm), the agreement between both methods is deteriorated: firstly, ERT does not, or at best does barely, capture the non-stained area which is largely cut off from the column wall where the electrodes are located and, secondly, ERT does not show an increased electrical

conductivity at the rightmost region where the optical method indicates increased Brilliant Blue concentration.

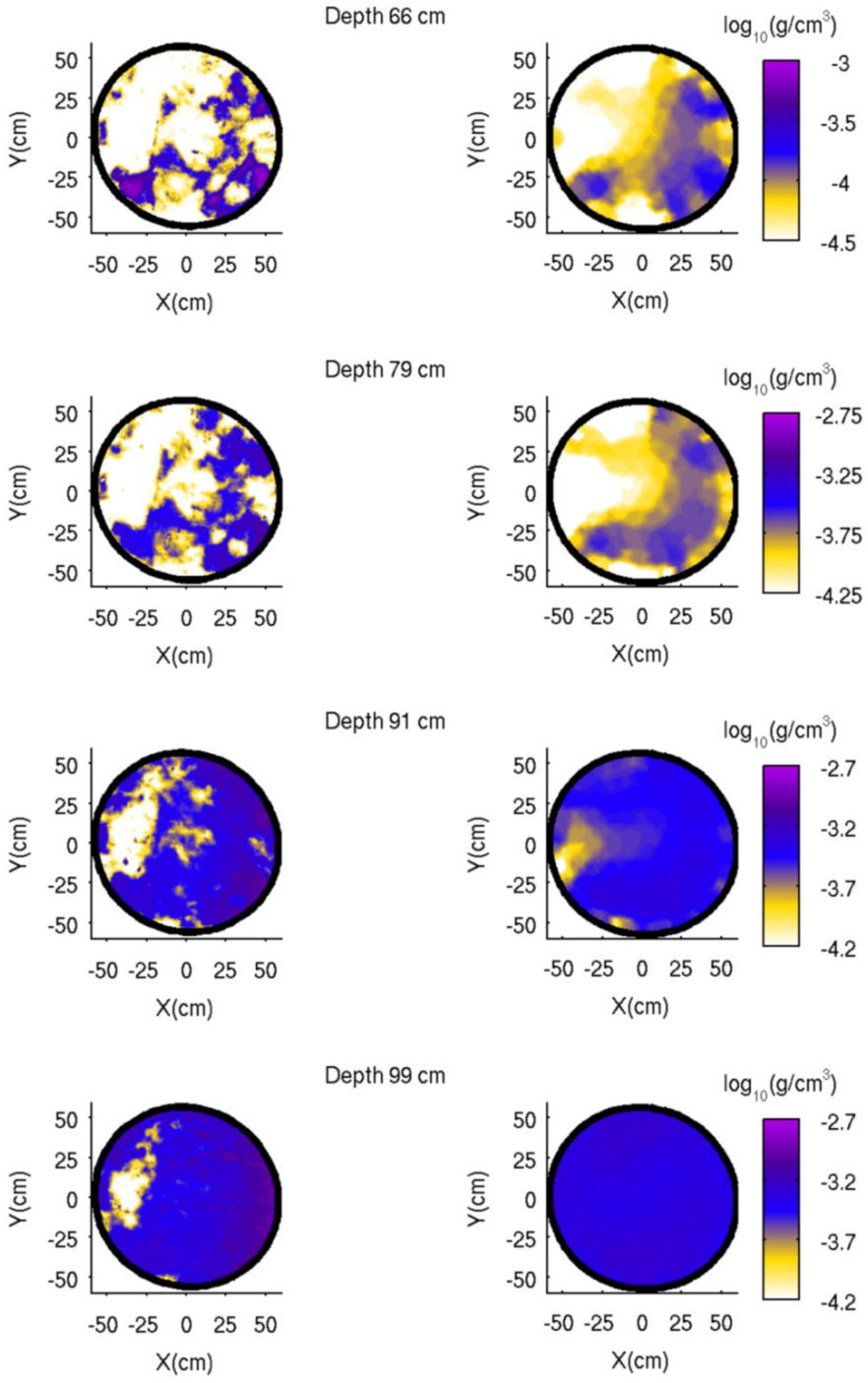


**Figure 3.12: Photographically-derived (left) and ERT-derived (right) bulk Brilliant Blue concentrations $C_b$ for the cross-sections at depths 66, 79, 91 and 99 cm.**

### 3.4.7. Discussion of mismatches between both imaging methods and the corresponding error sources

In this section, we discuss the results with respect to different error sources. Here, we consider a quantitative error appraisal desirable but restrict ourselves to a qualitative discussion as a quantitative analysis would (i) exceed the time budget and computation power available for our study and (ii) were strongly aggravated by the lack of respective data. In the following, we classify the error sources into three groups:

- measurement errors and errors due to the 1-D approximation and interpolation of a multitude of 3-D-variable parameters ($\Phi$, $\theta$, $\Delta S$, $\rho_b$, $\sigma_{b0}$, $\gamma$, $\sigma_s$, $\alpha$, $m$, $n$, $\Delta n$, $S_m$, $K_l$, $\beta$)
- ERT imaging errors
- imaging errors in the photographically derived Brilliant Blue concentration.

Figure 3.10 shows unbiased noise alongside with a systematic break-down of linearity between bulk Brilliant Blue concentration and ratio electrical conductivity with depth. The unbiased noise is attributed to all three of the above discussed errors.

In theory, the systematic break-down of the linearity between photographically-derived bulk Brilliant Blue concentration and ratio electrical conductivity could be also explained by means of measurement, approximation and interpolation errors. However, this would postulate highly improbable coincidences. The break-down of linearity is much better explained by ERT-imaging errors. In the topmost soil layers ($z < 66$ cm), the Brilliant-Blue-related electrical conductivity contrast and the respective lateral gradients are small. Such conditions are known to be especially suited for quantitatively sound smoothness-constrained ERT imaging (e.g. Singha and Gorelick, 2005). Here, the relationship between photographically-derived bulk Brilliant Blue concentration and ratio electrical conductivity is linear and reasonable petrophysical parameters were found in the Monte Carlo analysis. However, without ground-truth, their validity remains speculative.

In the depths of 66 cm and 79 cm, patches of large Brilliant Blue concentrations are located next to the electrodes (Figure 3.12). In these regions, the ERT sensitivity is maximal (Figure 4.4). As a result, the locations of the Brilliant Blue patches are captured correctly by ERT. However, due to the relatively large lateral electrical conductivity gradients, the maximum concentrations are smoothed and therefore underestimated (Figure 3.10, Figure 3.12). In the subsequent depths (91 cm and 99 cm), the major part of the cross-section is stained (Figure 3.12). The only unstained region is almost entirely cut of from the electrodes. It is known, that ERT is less sensitive to isolated spots of electrical conductivity contrast. Consequently, the unstained region is only partly (depth: 91 cm) or not at all (depth: 99 cm) visible in the ERT images. In this way, the linear relationship between photographically-derived bulk Brilliant Blue concentration and ratio electrical conductivity vanishes. For the depths of 79 cm and 91 cm, the breakdown of linearity can be compensated by large $n_{0,z}$ and small $\Delta n_z$ and $\gamma_z$ (Figure 3.11). For the depths below (99 cm and 108 cm), the range of photographically derived bulk Brilliant Blue concentrations is not resolved by ERT and Eq. (3.13) describes only an average value. We therefore address the anomalous parameters found in the Monte-Carlo analysis to ERT-imaging artifacts similar to the ones investigated and described by Day-Lewis et al. (2005) and Singha and Gorelick (2006).

For depths 91 cm and 99 cm, the photographically derived bulk Brilliant Blue concentration shows increased Brilliant Blue concentrations at the right hand side of the

cross-sections. These features should be detectable by ERT as it is located in a region of high ERT sensitivity. However, no regions with increased electrical conductivity are discernable on the corresponding ERT images (Figure 3.12). This suggests that here imaging artifacts in the photographically-derived Brilliant Blue concentrations are present. We suspect that they can be addressed to lateral illumination heterogeneities or lateral variations in soil color. The latter was observed in this part of the column during the sampling campaign. However, the region of apparently increased Brilliant Blue concentration and different soil color are not congruent.

## 3.5. Summary and conclusions

In this study we present evidence that Brilliant Blue staining patterns can be quantitatively recovered by means of their electrical conductivity contrast in moderately acid to basic media. It follows that Brilliant Blue staining patterns can not only be visualized by photographical methods but also by means of a non-invasive geophysical method sensitive to electrical conductivity contrast. The joint application of photographical and geophysical methods (in this study ERT) has various potential benefits, i.e. the Brilliant Blue staining patterns can be used to benchmark the ERT images and vice versa; the advantage of optical Brilliant Blue imaging (high spatial resolution) can be combined with the advantage of ERT imaging (spatio-temporal resolution) which should offer an improved characterization of transport processes; the photographically-derived Brilliant Blue image data can be used to constrain the ERT inversion problem.

Also, our study demonstrates the efforts that have to be invested in data collection and processing to relate electrical and optical Brilliant Blue images quantitatively, i.e. numerous petrochemical (pH, Brilliant Blue adsorption isotherm) and petrophysical parameters (e.g. water content, soil porosity, formation factor, saturation exponent) of the soil have to be characterized. In our study, we achieved this by using and interpolating data from TDR-probes and soil samples and by assuming that the petrochemical and petrophysical parameters were constant in the horizontal direction. Six petrophysical and petrochemical parameters for which no data was available were fitted by means of a Monte Carlo analysis. The six parameters obtained from the Monte Carlo analysis are believed to reflect to large part ERT-imaging errors. This improved the translation of the ratio electrical conductivities to bulk Brilliant Blue concentrations.

Our results illustrate the well known facts that stand-alone smoothness-constrained ERT is not ideally suited to image large electrical conductivity gradients and, more importantly, that isolated regions with electrical conductivity contrast may not be recovered. The former issue could be compensated by the use of a different regularization term, e.g. spatial statistics that are derived on basis of the photographically derived Brilliant Blue images. Moreover, both issues could be improved either by insertion of extra electrodes inside the soil which decreases the probability of isolated regions with electrical conductivity contrast or by a joint application with another geophysical imaging method, for example attenuation georadar (e.g. Ernst et al., 2007).

# 4. Non-invasive 3-D transport characterization in a sandy soil using ERT I: Investigating the validity of ERT-derived transport parameters*

## 4.1. Introduction

Understanding the relationships between soil properties, hydrologic initial and boundary conditions, and solute transport through unsaturated undisturbed soil is necessary to develop predictive models for a sustainable management of the environment (e.g. Vogel and Roth, 2003). During recent decades, these relationships have been investigated by means of numerous leaching experiments and new insights have been gained from the introduction of new measurement methods. The most successful methods to date are: suction cups, time-domain reflectometry (TDR), quantitative dye tracer imaging, multi-compartment sampling (MCS), and numerical experiments.

Suction cups have been applied for a long time in soil science (e.g. Biggar and Nielsen, 1976; Patterson et al., 2000). However, Weihermuller et al. (2005, 2006) recently showed that suction cups modify the local matrix potential and therefore the transport paths. We, therefore, consider suction-cup data of limited value for solute transport characterization.

TDR provides a large number of local volume averaged (or resident) concentration measurements with high temporal resolution (Kachanoski et al., 1992; Vanclooster et al., 1993; Mallants et al., 1994). In this fashion, vertical and lateral-scale effects on transport (Vanderborght et al., 1996; Jacques et al., 1998; Deurer et al., 2001; Javaux and Vanclooster, 2003) as well as flow rate effects (Vanderborght et al., 1997; Javaux and Vanclooster 2003) can be investigated. A disadvantage of TDR is that both the spatial resolution and the spatial coverage of the transport process observation are limited. This makes the technique less suited for investigating the effect of soil properties on the spatial structure of the transport processes.

Quantitative dye tracer imaging, in contrast, yields spatially highly resolved information (Forrer et al., 2000). It has been successfully applied to infer information about the relationship between soil structures and transport processes (Forrer et al., 1999; Perillo et al., 1999; Javaux et al., 2006; Vogel et al., 2006). An important drawback of this method is its destructive nature. Unless the experiment is restricted to 2-D, like e.g. experiments that are carried out in soil containers with transparent walls (Wildenschild and Jensen, 1999; Ursino, et al., 2001), only one snapshot of the transport process can be obtained. The combined effects of flow rate, water saturation, and soil properties on the structure of the transport process can only be investigated in an indirect manner.

TDR and dye-staining provide resident concentrations which represent the mass of solute per bulk volume of soil or pore water. If the transport process is heterogeneous within the volume in which the concentration is defined, the resident concentration is a volume weighted average of the local concentrations within that volume. Although time series and depth profiles of resident concentrations can be used for transport characterization (e.g.

* Adapted from Koestel, J., J. Vanderborght, M. Javaux, A. Kemna, A. Binley and H. Vereecken. Non-invasive 3-D transport characterization in a sandy soil using ERT I: Investigating the validity of ERT-derived transport parameters. Vadose Zone Journal. Accepted for publication.

Jury and Roth, 1990; Javaux and Vanclooster, 2003), they are less suited to estimate solute fluxes or solute leaching. This is especially the case when preferential flow occurs through a small fraction of the total pore volume. Here, flux concentrations (the solute flux divided by the water flux density) are more relevant. Flux concentrations are readily obtained by measuring the concentration in the effluent of soil column experiments. Recently, multi-compartment sampling (MCS) methods have been developed which allow spatially resolved sampling of the effluent flux densities (e.g. Wildenschild et al., 1994; de Rooij and Stagnitti, 2002). However, for obvious reasons, such systems interrupt the flow process at a given depth in the soil profile. As a consequence, it is not possible to investigate the continuity of the flow paths in the main (vertical) flow direction, which is a key parameter for determining the scaling behaviour of the transport process.

Due to the lack of measurement methods providing 3-D spatio-temporal resolution of both, resident and flux concentrations, numerical simulations in heterogeneous unsaturated soils have been carried out in order to understand solute transport in heterogeneous soils. Roth (1995) and Roth and Hammel (1996) published an experiment which suggests that the structure of the flow and transport process changes with the applied flow rate and the degree of water saturation of the medium. Vanderborght (2001) demonstrated in a numerical study that similar solute concentration distributions are possible in soil-like media with completely different structures. Therefore, spatio-temporal monitoring of transport is necessary to relate soil structures unequivocally to the structure of the transport process (Vanderborght et al., 2006).

In our study, we utilize the 3-D geophysical imaging technique - electrical resistivity tomography (ERT). In addition to spatial resolution, one advantage of this method is that it is applicable to a wide range of scales, from some centimeters (e.g. Olsen et al., 1999) up to several kilometers (e.g. Revil et al., 2008). In order to investigate the spatio-temporally resolved characteristics of solute transport processes by means of time-lapse ERT image series, the pixel (2-D) or voxel (3-D) breakthrough curves (BTCs) have proved to be useful. The concept was introduced by Binley et al. (1996a) and subsequently applied by Olsen et al. (1999), and Slater et al. (2000, 2002). As an extension to this approach, apparent transport model parameters can be obtained by fitting the convection-dispersion equation (CDE) to the individual pixel/voxel BTCs (Kemna et al., 2002; Vanderborght et al., 2005). In this way the features of local solute BTCs are captured with the apparent transport velocity and the apparent dispersivity. The 3-D features of the transport process can then be assessed by the spatial distribution of these parameters.

A drawback of ERT is the non-uniqueness of the ERT inversion problem. Ideally, the inversion is constrained by data from an independent method which complements the ERT data. If these are not available, the smoothness constraint is typically applied. This may lead to bias in the ERT inversion image (Friedel, 2003; Day-Lewis et al., 2005; Singha and Gorelick, 2006; Day-Lewis et al., 2007) which then may cause bias in ERT-derived tracer mass (Binley et al., 2002b; Singha and Gorelick, 2005) or transport parameters (Vanderborght et al., 2005).

The amount of bias in the ERT image data varies spatially. It depends on the ERT survey design (quantity and spatial arrangement of measurements), the structure of the electrical conductivity distribution of the investigated domain, and the data error (Day-Lewis et al., 2005). Methods that are able to appraise the bias in ERT images exist, however, when they are applied to 3-D problems, they either demand excessive computational power, as in the case of the model resolution matrix (e.g. Friedel, 2003; Day-Lewis et al., 2005) or Bayesian inversion approaches (Yeh et al., 2002; Ramirez et al., 2005); or they provide a

rather qualitative measure of regions prone to bias like sensitivity analyses (e.g. Spitzer, 1998; Kemna et al., 2002). Only recently, Oldenborger et al. (2007) introduced the so-called volume of investigation index which might be used as an alternative in future studies.

In addition, when transport processes in the vadose zone are considered, changes in bulk electrical conductivity need to be related to changes in solute concentrations. Here, real or apparent petrophysical parameters are required with a 3-D spatial resolution (Singha and Gorelick, 2006). These are seldom available. The number of unknowns can, however, be considerably decreased if the water content is kept constant and if time-lapse images are considered (e.g. Olsen et al., 1999).

Furthermore, in order to compare transport properties derived from time-lapse ERT data obtained from different transport experiments, it is essential that data inversion has been applied with similar levels of regularization. Variation in ERT data error, due to different degrees of water and solute saturation, have to be compensated; bias due to varying distance that the tracer travels during the ERT data acquisition time, in the following referred to as temporal smearing, has to be attributed; a data selection approach has to be considered that minimizes the differences in ERT-sensitivity between all available ERT-frames.

Based on the above considerations it is difficult to quantitatively compare 3-D spatially resolved ERT-derived data from different solute displacement experiments. To our knowledge such a study has not yet been published in peer-reviewed literature. At best Olsen et al. (1999) presented a study which aims in this direction but conclusions drawn from the ERT image data remain qualitative.

Recently, Koestel et al. (2008) presented an experimental setup, requiring hydraulic steady-state conditions, which allow the translation of bulk electrical conductivity explicitly to solute concentration without knowledge of the apparent or real petrophysical parameters. In their experiment, the tracer mass was estimated correctly by ERT at the column outflow. Furthermore, they introduced a refined method to estimate the error in the ERT raw data and used TDR as a ground truth for the ERT image data. Both innovations helped to adjust and appraise bias in the ERT images.

The aim of this study is principally to investigate the potential and limitations of smoothness-constrained ERT to quantitatively derive and compare 3-D spatio-temporal solute transport characteristics of four different solute displacement experiments in a large soil column. Here, we make use of the above discussed experimental setup and innovations which are published in Koestel et al. (2008).

Our study is organized in two parts. In the first part (this chapter), we focus on the description of the experimental setup, the data acquisition and processing, the estimation of the apparent transport parameters, and the validation of the ERT-derived transport parameters against TDR measurements, the tracer mass balance, and the effluent BTC. Furthermore, we investigate the impact of spatial variations in ERT-sensitivity on the ERT-derived apparent transport parameters. In the second part (chapter 5), we discuss 1-D and 3-D apparent transport parameters with respect to scale, soil structure and properties, and hydrologic state variables. Furthermore, we investigate the transport mechanism and the lateral scale-dependency of the apparent dispersivity. We present details on soil properties and the irrigation system in this second part as we consider them to be more relevant with respect to the solute transport characteristics than to the validation of the

ERT-derived data.

## 4.2. Material and Methods

### 4.2.1. Excavation of the Soil Column

We carried out inert tracer experiments in a large circular undisturbed soil column (height 140 cm, inner diameter 116 cm, Figure 4.1) that was taken from an agricultural field site near Kaldenkirchen (Germany). The soil column was extracted from the field by pushing a PVC cylinder (2 cm wall thickness) into the soil. PVC instead of stainless steel was used in order to make geo-electrical measurements possible. The bottom edge of the PVC column was sharpened in order to reduce compaction of the soil at the inner side of the column wall and to facilitate the soil sampling. On top of the column, a steel plate was placed and the column was slowly pressed into the soil in 10 cm intervals by the shuffle of an excavator. In order to reduce the friction between the PVC cylinder and the soil, the soil around the cylinder was excavated. Great care was taken that the column remained vertical keeping artificial soil compaction or gaps near the column walls at a minimum. After the column was completely filled, a perforated PVC plate was pushed underneath it using a steel scaffold. The soil column and PVC plate were placed on a 5 cm thick sand bed in a steel collection pan that was mounted on a frame. The column was transported to the lysimeter facility at the Forschungszentrum Jülich where it was installed on a weighing scale.

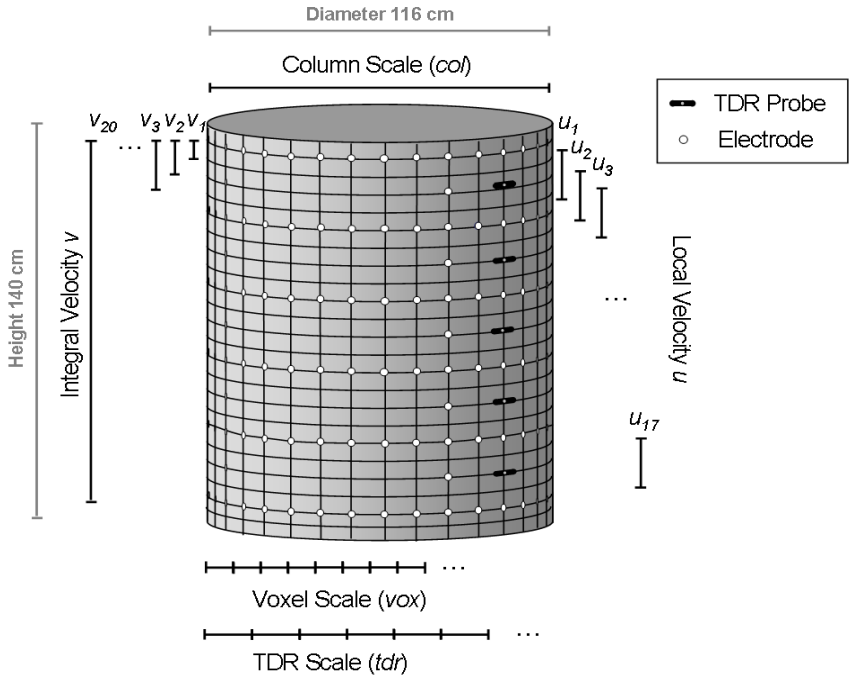


**Figure 4.1: Sketch of the soil column with electrode and TDR-probe locations. Additionally, the different scales at which solute transport is investigated are illustrated.**

### 4.2.2. Experimental Design

In order to enable quantitative interpretation of the ERT data, the experiments were performed under hydraulic steady-state conditions. We used an irrigation device which delivered water to the top surface of the lysimeter through 484 equally distributed needles.

Details about the irrigation homogeneity are presented in the next chapter. A thin layer of gravel (1 cm) was put on top of the column to prevent slaking and crust formation at the soil surface by the impact of the water drops. The soil column was situated in a climate controlled basement where temperature (10 °C) and humidity (relative humidity of 70%) of the air were kept approximately constant throughout the experiment. The evaporation rate was kept at a minimum as the irrigation device was mounted directly on top of the column and largely sealed the soil surface from the ambient. Since no suction was applied, the bottom surface of the lysimeter remained saturated. The drainage water was collected from 12 outlets which were equally distributed over the column's bottom. The outflow rate was measured using a 100-ml tipping bucket. The effluent was lead through in a small vessel with a water-filled volume of approximately 25 $cm^3$ in which the electrical conductivity of the effluent was measured before it was eventually disposed in a large tank by means of a submersible pump.

We applied two different irrigation rates, both leading to unsaturated conditions inside the soil column. The steady state conditions were checked by means of the tipping bucket and the lysimeter mass. The experiments were started after 3 months of steady tap water irrigation (1.5 cm/d). The lower irrigation rate was adjusted to 1.5 cm/d and the higher to 6.5 cm/d (Table 4.1). For each flow rate, the irrigation was started with tap water. When steady state conditions had been established, the tap water (503 µS/cm) was replaced by a $CaCl_2$ solution (2520 µS/cm) which provided a positive electrical conductivity contrast. After the electrical conductivity at the outflow had stabilized to the $CaCl_2$ solution's electrical conductivity, the irrigation water was changed back to tap water. Now the tap water acted as a tracer with negative electrical contrast. In this fashion, four tracer experiments were conducted in total: one 'positive' and one 'negative' tracer experiment for each flow rate, respectively. They are referred to as experiments 1a and 1b for the low-flux experiments and experiments 2a and 2b for the high-flux experiments.

**Table 4.1: Overview of the experimental conditions, the apparent CDE parameters at the outflow, and the mean and standard deviation of the residuals between TDR and ERT-derived apparent CDE parameters.**

| Experiment | | 1a | 1b | 2a | 2b |
|---|---|---|---|---|---|
| Average flux density | (cm/d) | 1.5 | 1.5 | 6.3 | 7.1 |
| Std deviation of the flux density | (cm/d) | 0.1 | 0.1 | 0.4 | 0.3 |
| Electrical conductivity contrast | (-) | positive | negative | positive | negative |
| Average tracer travel distance during one ERT frame | (cm) | 2.5 | 2.5 | 7.3 | 8.2 |
| RMSE[$R_M$]$^{\dagger}$ | (%) | 2.6 | 2.8 | 3.3 | 4.3 |
| $v_{EFFL}$ | (cm/d) | 7.2 | 7.0 | 27.5 | 31.1 |
| $v_{col}$ at $z$ = 127 cm | (cm/d) | 7.2 | 7.1 | 26.8 | 30.9 |
| $\lambda_{EFFL}$ | (cm) | 2.8 | 2.3 | 1.5 | 1.8 |
| $<\lambda_{vox}>$ at z = 127 cm | (cm) | 1.3 | 1.2 | 1.0 | 0.9 |
| $\lambda_{col}$ at $z$ = 127 cm | (cm) | 2.5 | 2.3 | 1.6 | 1.7 |
| $<R_v>$ | (%) | 0 | 0 | 1 | - |
| std[$R_v$] | (%) | 2 | 3 | 6 | - |
| $<R_u>$ | (%) | 0 | -1 | -3 | - |
| std[$R_u$] | (%) | 8 | 9 | 10 | - |
| $<R_\lambda>$ | (%) | 42 | 40 | 55 | - |
| std[$R_\lambda$] | (%) | 41 | 32 | 96 | - |

$^{\dagger}$ not considering the $R_M$ of the first three frames of each experiment

### 4.2.3. Data acquisition and imaging

The tracer breakthrough was monitored with time-lapse ERT. We used a six-channel GeoServe RESECS prototype to carry out the ERT measurements. The majority of 212 (stainless steel) ERT electrodes were arranged in six horizontal rings around the circumference of the soil column (6 x 32, Figure 4.1). The electrodes were 1.2 cm in diameter, 5 cm in length, and extended into the soil by 3 cm. The vertical spacing between the rings was 25 cm. We used horizontal dipoles with a spacing of 23 cm and vertical dipoles with a spacing of 25 cm. For the low-flux experiments, we measured one ERT frame consisting of 46,260 potential measurements (including reciprocals) per day. The measurement time for one frame took 8 hours and 23 minutes. For the high flux experiment, the measurement time was decreased to 6 hours and 23 minutes by reducing the number of potential measurements to 37,428 (including reciprocals). Three frames per day were collected in order to account for the higher transport velocity.

We inverted each ERT frame individually with the error-weighted, smoothness-constrained 'Occam's-type' inversion code R3t (Binley et al., 1996b). The algorithm finds the smoothest distribution of electrical conductivity which fits the measured data to a specified error level $\varepsilon_{app}$ (Ω) using the approach described in Binley and Kemna (2005). We used iterative data weighting as described in Morelli and LaBrecque (1996) and did not apply time-lapse regularization. For the forward solution, the soil column was discretized into a finite element mesh containing 14,720 triangular prisms with edge lengths and heights of approximately 6 cm. To reduce computational demands, a coarser mesh was used for the

parameterization of the inverse solution by assigning the same parameter to a patch of four horizontally adjacent elements of the forward model mesh, respectively. One patch corresponds to a volume of approximately 400 cm³.

The ERT inversion problem is ill-conditioned and ill-posed. The former means that small errors in the data can lead to large errors in the results. It follows that the appraisal of the measurement and model error plays an important role. Ill-posedness denotes in our case that the problem has no unique solution. It must, therefore, be regularized. In our study this was done by means of a smoothness constraint. In the inversion code that we used (R3t), the amount of regularization is coupled with the specified error level to which the data is fitted.

We estimated the appropriate error level $\varepsilon_{app}$ on basis of the reciprocal error (see Slater et al., 2000) for each ERT frame individually, using the method described in Koestel et al. (2008). $\varepsilon_{app}$ is modeled as follows:

$$\varepsilon_{app} = a_{app} + b_{app} R \,, \tag{4.1}$$

where $a_{app}$ (Ω) represents an absolute error component, $b_{app}$ (-) stands for a relative error component, and $R$ (Ω) is the ERT transfer resistance (see Koestel et al., 2008). For the purpose of producing ERT inversion images with similar amounts of smoothness we inverted all ERT data to the same error level. In order to prevent over-fitting, we chose the error level with respect to the experiment with the largest reciprocal error.

The accuracy and resolution of smoothness-constrained ERT depends not only on the data and model error (represented by the error level $\varepsilon_{app}$) but also on the structure of the imaged bulk electrical conductivity itself. From the latter, it follows that accuracy and resolution can only be appraised in an approximate manner. Here, the linearized model resolution matrix provides a measure to estimate the reliability of the ERT image data (Menke, 1989). However, calculating the resolution matrix for large 3-D problems demands excessive computational power which was not at our disposal. Computationally less expensive measures of uncertainty are the volume investigation index (recently introduced by Oldenborger et al., 2007) and sensitivity analyses (e.g. Spitzer, 1998; Kemna et al., 2002). In our study, we used a simple sensitivity analysis as described in Kemna et al. (2002). The sensitivity analysis provides a map of how much information of the local electrical conductivity is captured by the ERT measurements, namely the transfer resistances. In high-sensitivity regions, the ERT image data are more reliable than in regions with low sensitivity.

In addition to ERT, the tracer breakthrough was monitored by means of 10 3-rod TDR probes. We used a Campbell Scientific TDR100 system with SDMX50 multiplexers and a CR10X data logger made from the same manufacturer. The TDR data were logged in hourly intervals. In order to avoid electric short-cuts through the TDR cables, we disconnected the TDR device with the aid of built in relays whenever the ERT device was active (see Koestel et al., 2008). The TDR rods were 18.8 cm long, 0.25 cm thick, and the distance between the centers of two rods was 2.5 cm. They were located in five different depths, namely 17.5 cm, 42.5 cm, 67.5 cm, 92.5 cm, and 117.5 cm (Figure 4.1). We applied the in-situ calibration approach presented in Mallants et al. (1996) in order to translate the TDR attenuation coefficient to solute concentrations. The TDR data was also used to measure the water content and the mixing model published in Roth et al. (1990)

was used to calculate the water content from the dielectric permittivity. The parameterization of the mixing model is published in Koestel et al. (2008).

Next to each TDR-probe a tensiometer was installed (UMS T4). The tensiometer data were logged every 10 minutes with aid of a MAC19 data logger. The electrical conductivity of the effluent was measured by means of a WTW Cond340 device. It was logged in 10 minute intervals.

### 4.2.4. Translating bulk electrical conductivity to solute concentration

The experimental setup allows us to directly infer the change in solute concentration from the bulk electrical conductivity change as long as hydraulic steady state conditions are maintained. Following Waxman and Smits (1968), the relationship between bulk electrical conductivity $\sigma_b$ (µS/cm) and resident chloride concentration $C_r$ (µg/l) is

$$C_{r,t} = \frac{\sigma_{b,t} - \sigma_{b,0}}{\sigma_{b,end} - \sigma_{b,0}} \left( C_{r,end} - C_{r,0} \right) + C_{r,0} \tag{4.2}$$

as long as the relationship between the solute electrical conductivity $\sigma_w$ (µS/cm) and the chloride concentration $C_r$ is linear. The index '$t$' refers to an arbitrary point in time between start and end of the experiment. The flux concentrations $C_f$ (µg/l) in the effluent were obtained from the respective electrical conductivities $\sigma_w$ (µS/cm) using basically the same relationship as given by Eq. (4.2):

$$C_{f,t} = \frac{\sigma_{w,t} - \sigma_{w,0}}{\sigma_{w,end} - \sigma_{w,0}} \left( C_{f,end} - C_{f,0} \right) + C_{f,0} \tag{4.3}$$

The approach and underlying assumptions are documented in detail in Koestel et al. (2008).

### 4.2.5. Comparing ERT-derived and mass-balance-derived tracer mass

In this section, we explain the approach used to validate the ERT-derived tracer mass. In a first step we calculated the change in chloride mass inside the soil column with respect to the initial chloride mass by means of the mass balance:

$$\Delta M_{MB,t} = \sum_{j=1}^{N} \left( C_{f,in} - C_{f,out} \right) \cdot q \cdot r^2 \cdot \pi \cdot \Delta t_j \ . \tag{4.4}$$

In Eq. (4.4), $t$ (d) denotes the time and $z$ (cm) the vertical distance to the column's upper surface, $\Delta M_{MB,t}$ (µg) is the change in chloride mass at time $t$ with respect to the chloride mass at $t = 0$, $C_{f,in}$ (µg/ml) and $C_{f,out}$ (µg/ml) denote the chloride flux concentration of the irrigation and outflow-water, respectively, $r$ (cm) is the soil column radius, and $\Delta t_j$ (d) is the time step between ERT frame $j$-1 and ERT frame $j$. $N$ denotes the last ERT frame taken into account.

Next, we derived the corresponding change in tracer mass using the ERT-derived resident chloride concentrations $C_r$, according to:

$$\Delta M_{ERT,t} = \sum_z \sum_k \theta_z V_{vox} \left( C_{r,t,z,k} - C_{r,t0,z,k} \right),$$

**(4.5)**

where $\Delta M_{ERT,t}$ (µg) is the change in chloride mass at time $t$ with respect to the chloride mass at $t = 0$ (denoted as '*t0*'), $C_{r,t,z,k}$ (µg/ml) and $C_{r,t0,z,k}$ (µg/ml) are the ERT-derived resident chloride concentration in voxel $k$ in the voxel layer in depth $z$ at time $t$ and *t0*, respectively, $\theta_z$ (cm³/cm³) is the average water content at depth $z$, and $V_{vox}$ is the volume of one voxel.

In order to apply Eq. (4.5) the water content $\theta_z$ was estimated using the TDR data. We first took the average water content from each two TDR probes in each depth at which TDR probes had been installed. Then, we linearly interpolated the water contents $\theta_z$ for all voxel layers. For the voxel layers outside the TDR array we assigned the $\theta_z$ of the nearest voxel layer inside the TDR array.

The misfit between the ERT-derived and the mass-balance-derived change in chloride mass was expressed as:

$$R_M = \frac{\Delta M_{ERT,t} - \Delta M_{MB,t}}{\Delta M_{MB,t}} \cdot 100 .$$

**(4.6)**

### 4.2.6. Apparent CDE parameters

We used apparent CDE parameters, namely the apparent velocity $v$ (cm/d) and dispersivity $\lambda$ (cm) to characterize the shape of breakthrough curves (BTCs) of the resident concentration $C_r$ that were measured inside the column and the flux concentrations $C_f$ (µg/ml) that were measured in the column effluent:

$$\frac{\partial C_r}{\partial t} = \lambda v \frac{\partial^2 C_r}{\partial z^2} - v \frac{\partial C_r}{\partial z} \qquad \text{and} \qquad \frac{\partial C_f}{\partial t} = \lambda v \frac{\partial^2 C_f}{\partial z^2} - v \frac{\partial C_f}{\partial z} .$$

**(4.7a and b)**

We obtained the apparent velocity $v$ and dispersivity $\lambda$ by fitting the solution of Eq. (4.7) for first type ($C_f$) and third type ($C_r$) boundary conditions (see Parker and van Genuchten, 1984) to the respective BTC. The apparent velocity $v$ corresponds to the transport velocity of the solute front in vertical direction and $\lambda$ characterizes the vertical spread of the tracer front. The apparent CDE parameters are equivalent to scaled temporal moments of the BTCs.

In a preceding study (see Koestel et al., 2008) we found that ERT-derived BTCs are, to a minor part, subject to overshoot due to artifacts in the ERT inversion process. In order to filter these BTCs, we discarded all CDE parameters from cases where the CDE equation could not be fitted with coefficients of determination, $R^2 > 0.95$. Furthermore, in order to prevent extrapolation outside the sensed soil volume, we abstained from interpreting the ERT-derived transport parameters of the topmost 5 cm of the soil column as well as the bottommost 10 cm of the 3-D ERT images.

### 4.2.7. Observation scales

We derived transport parameters at different horizontal and vertical observation scales (Figure 4.1). In the horizontal we differentiated the three scales: (i) the column scale (subscript '*col*'); (ii) the TDR scale (subscript '*tdr*'); (iii) the ERT voxel scale (subscript '*vox*').

The column scale (approximately 100 cm) refers to the cross-sectional area of the column ($58 \times 58 \times \pi$ cm). The column-scale CDE parameters at the column's outflow were directly obtained from the effluent BTC. The ERT-derived column-scale CDE parameters were obtained from the area-weighted average of all voxel BTCs in a considered depth.

Based on a study of Ferré et al. (1998), the sampling volume of the TDR probes used in our study is approximately 750 cm³ ($3.75 \times 3.75 \times \pi \times 18.8$ cm), corresponding to a scale of approximately 9 cm. The TDR-scale CDE parameters were derived from the TDR measured resident concentration BTC.

The voxel scale refers to the equivalent lateral extent of the patch of finite elements used in the ERT mesh for the inverse problem (approximately 7 cm). The CDE parameters were fitted to each voxel BTC.

In the vertical direction we distinguished between the integral scale and the local scale. The integral velocity $v$ refers to the distance between the column top and the depth coordinate $z$ (Figure 4.1). It is obtained directly from the CDE fit and it represents the average or integrated velocity along the trajectory of a solute particle from the soil surface to the observation depth $z$. The local velocity $u$ (cm/d) refers to the velocity over the vertical distance of 25 cm. This corresponds to the vertical distance between two TDR probes or the height of 4 finite elements used in the ERT inversion. We calculated $u$ at a depth $z_i$ from the integral velocity $v$ at depths $z_{i+2}$ and depth $z_{i-2}$ according to:

$$u_{z,i} = \frac{z_{i+2} - z_{i-2}}{\left(\frac{z_{i+2}}{v_{z,i+2}}\right) - \left(\frac{z_{i-2}}{v_{z,i-2}}\right)}. \qquad \textbf{(4.8)}$$

In Eq. (4.8) the subscript $i$ denotes the $i^{\text{th}}$ horizontal voxel node layer, numbered in ascending order from the column top to its bottom.

### 4.2.8. Comparison of the ERT data with TDR and effluent data

The comparison between TDR and ERT data was carried out by comparing the CDE parameters of the lumped BTC of all voxels intersecting the TDR sampling volume. We expressed the accuracy of ERT with respect to TDR by means of the mean and standard deviation of percentage of relative residuals for all 10 probes:

$$\left\langle R_v \right\rangle = \left\langle \frac{v_{tdr,ERT} - v_{tdr,TDR}}{v_{tdr,TDR}} \right\rangle \cdot 100 \quad \text{and} \quad \text{std}\left[R_v\right] = std\left[ \frac{v_{tdr,ERT} - v_{tdr,TDR}}{v_{tdr,TDR}} \right] \cdot 100 . \qquad \textbf{(4.9a and b)}$$

The mean of $R_v$ denotes the accuracy (or bias) in the ERT-derived transport parameters whereas the standard deviation of $R_v$ reflects precision. In a manner analogous to Eq. (4.9a and b), the mean and standard deviation of the TDR/ERT dispersivity residuals $R_\lambda$ were

derived. The TDR-derived CDE parameters at the TDR scale are referred to with the subscript '*tdr,TDR'*, the ERT-derived ones at the TDR scale with the subscript '*tdr,ERT'*.

In addition, we compared the column-scale CDE parameters of the effluent BTC (subscript '*col,EFFL')* with the ones obtained from ERT in depth $z$ = 127 cm (subscript '*col,ERT').*

## 4.2.9. Investigation of the relationship between ERT sensitivity and ERT-derived transport parameters

Vanderborght et al. (2005) reported that the ERT-derived voxel-scale apparent dispersivity $\lambda_{vox}$ increases with decreasing ERT sensitivity. In contrast, they found no change of apparent velocities $v_{vox}$ with changes of ERT sensitivity. In this section we describe an approach to investigate this issue with respect to the ERT-derived transport parameters in our study, namely $v_{vox}$, $u_{vox}$, and $\lambda_{vox}$.

From the spatial arrangement of the ERT electrodes used in our study we inferred that the ERT sensitivity variations in the vertical direction are negligible compared to the ones in the horizontal direction. We, therefore, focused on sensitivity variations in the horizontal direction. For this purpose we removed trends that the apparent CDE parameters exhibited in the vertical direction. We achieved this by normalizing the voxel-scale apparent CDE parameters to the corresponding column-scale parameter in each considered depth. Next, the normalized voxel-scale apparent CDE parameters were collected in quadratic bins with edge length of 15 cm which were superimposed to the horizontal cross-section of the column for each voxel layer (see Figure 4.2). Then, we calculated the mean ($<v_{n,bin,ERT}>$, $<u_{n,bin,ERT}>$, and $<\lambda_{n,bin,ERT}>$) and the standard deviation (std[$v_{n,bin,ERT}$], std[$u_{n,bin,ERT}$], and std[$\lambda_{n,bin,ERT}$]) of all normalized apparent CDE parameters within each bin. The subscript $n$ denotes that the CDE parameters are normalized. Finally, we contrasted the obtained statistics with the radial distance $r_d$ (cm) to the horizontal column center which is a proxy for the ERT sensitivity.

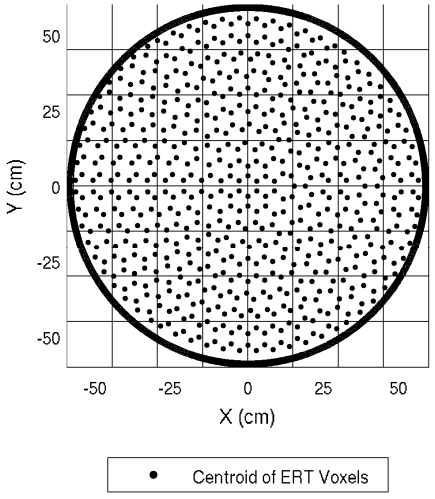


**Figure 4.2: Sketch illustrating how the normalized voxel-scale apparent CDE parameters are collected in quadratic bins with edge length of 15 cm (plan view) for the investigation of the impact of ERT sensitivity on the ERT-derived CDE parameters. Each dot represents the centroid of the triangular horizontal cross-section of one prismatic ERT-voxel.**

## 4.3. Results and discussion

### 4.3.1. Pre- and post-processing of the ERT Data

The time series of the absolute and the relative reciprocal error components, $a_{app}$ and $b_{app}$, of the ERT measurements for each experiment are shown in Figure 4.3. It can be seen that the high-flux experiments exhibit a larger reciprocal error during the main tracer breakthrough (frames #5 - #15). This is likely due to the larger amount of temporal smearing which is inherent in the ERT data for the high-flux experiments (Table 4.1).

In our study, experiment 2b exhibits the largest reciprocal error with an average absolute error of 0.019 Ω and a relative error of 0.009. Koestel et al. (2008) found a reasonable match between TDR, effluent and ERT data for an ERT error level $\varepsilon_{app}$ of approximately two times the reciprocal error. Consequently, we inverted all ERT frames to an absolute error of 0.04 Ω and a relative error of 0.02.

Prior to the inversion, we removed outliers from the ERT raw data as described in Koestel et al. (2008). The number of retained transfer resistances for experiments 1a, 1b, 2a, and 2b were 6,371 (27.5 %), 6,673 (28.8 %), 4,468 (23.9 %), and 6,374 (34.1 %), respectively (not including reciprocals).

When fitting the CDE-equation to the voxel BTCs of all experiments (58,880 in total), 988 (1.7 %) yielded an $R^2 < 0.95$ and were not used for further analysis.

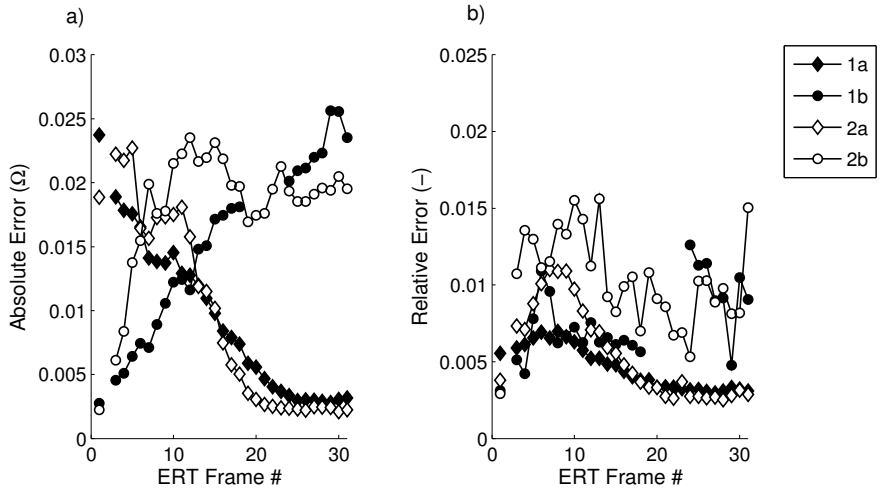


**Figure 4.3: (a) the absolute component of the reciprocal error, $a_{app}$, for each frame and experiment; (b) the relative error component of the reciprocal error, $b_{app}$, for each frame and experiment.**

### 4.3.2. ERT sensitivity distribution

As a representative example, Figure 4.4 shows the sensitivity distribution for experiment 1a, frame #3. The ERT sensitivity alters slightly for each frame and experiment but the main features remain identical: the sensitivity is high near the column walls and low near the horizontal center of the column. This is basically a consequence of the circumferal electrode array used in our study.

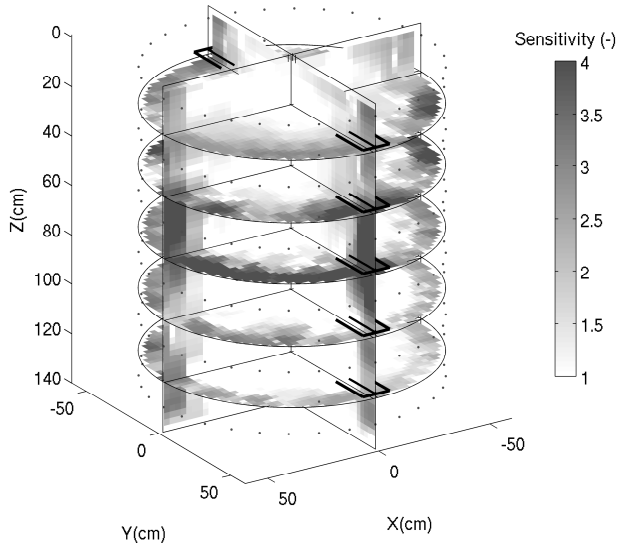


**Figure 4.4: The ERT sensitivity distribution for experiment 1a, frame #3.**

Note that the TDR ground truth is, at best, valid for regions where the ERT sensitivity is similar to the one at the TDR locations. This corresponds to all voxels with less than approximately 20 cm distance to the soil column walls. The ground truth at the effluent is representative for the bottommost part of the soil column.

### 4.3.3. Accuracy of ERT-derived tracer mass

Figure 4.5 shows that ERT estimated the tracer mass inside the soil column with high accuracy except for the first two or three ERT frames of each experiment. For these frames the tracer had reached only the topmost part of the column. Here, large errors in the ERT image are likely as voxels predominantly outside the electrode array were involved in the tracer mass calculation. Moreover, the TDR-derived water content (Figure 4.6) which had been extrapolated for the topmost 17.5 cm of the column is probably biased in this part of the column. In neglecting the first three frames of each experiment, the root mean squared residuals between mass balance and ERT-derived changes in tracer mass, $\Delta M_{MB}$ and $\Delta M_{ERT}$, ranges between 2.6% and 4.3%. We attribute this excellent result to (i) the application of the tracer as a step which is homogeneously distributed over the entire upper boundary of the investigated domain; (ii) the location of the electrodes at the vertical boundaries of the investigated domain; (iii) the improved sensitivity of ERT within a bounded domain; (iv) the scaling of the bulk electrical conductivity to the minimum and maximum chloride concentration (see also Koestel et al., 2008).

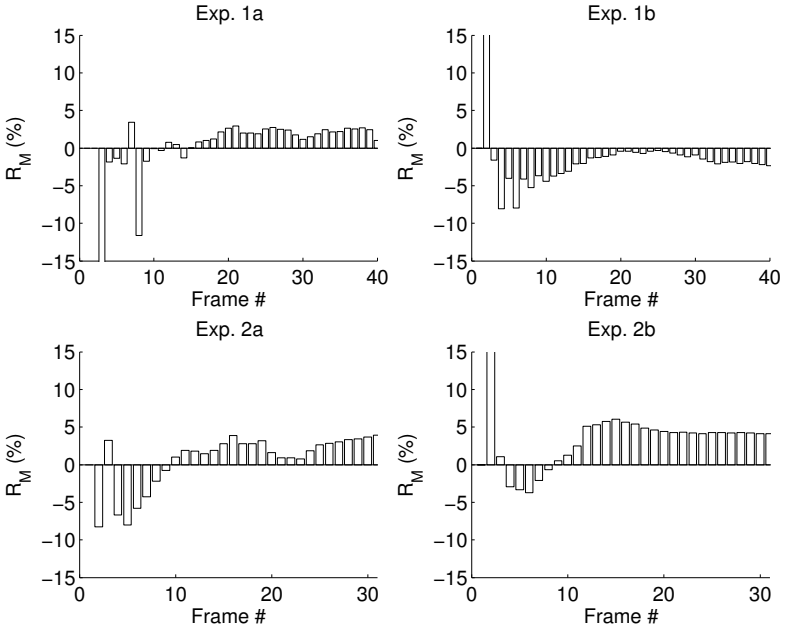


**Figure 4.5: Relative residuals $R_M$ (%) between change in tracer mass as calculated by means of the mass balance and by means of the ERT-derived chloride concentration.**

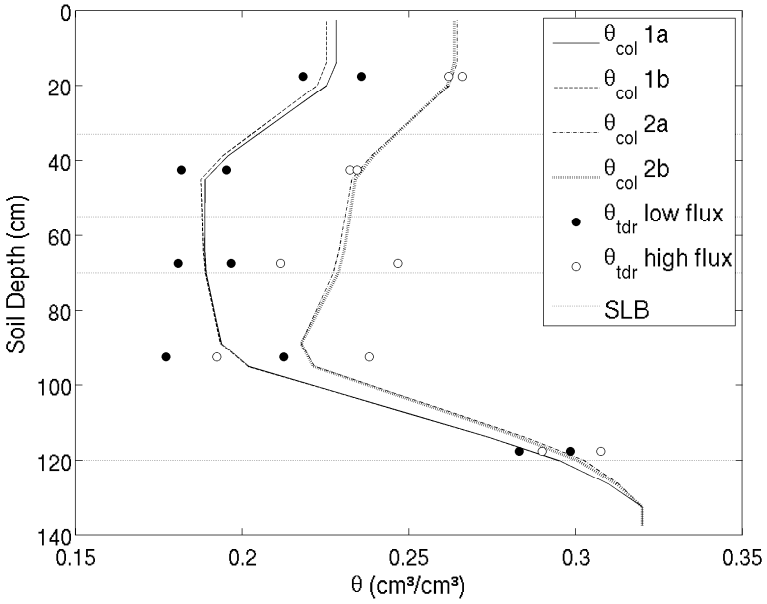


**Figure 4.6: The water content $\theta_{col}$ (cm³/cm³) used for the calculation of the ERT-derived tracer mass inside the column. The circles depict the water content measured at each TDR probe in one depth during the low and the high-flux experiments, respectively. SLB stands for soil layer boundaries.**

## 4.3.4. Accuracy of CDE fitting on the ERT-derived BTCs

Four randomly selected ERT-derived voxel BTCs and the corresponding CDE fit of experiment 2b are compiled in Figure 4.7 for illustration purpose. In Figure 4.8 the column-scale BTC at the bottommost ERT voxel layer within the electrode array (depth $z$ = 127 cm) and the corresponding effluent BTCs are shown together with the CDE fit.

The coefficient of determination, $R^2$, of the all CDE fits (column scale, TDR scale, voxel scale) was predominantly larger than 0.97.

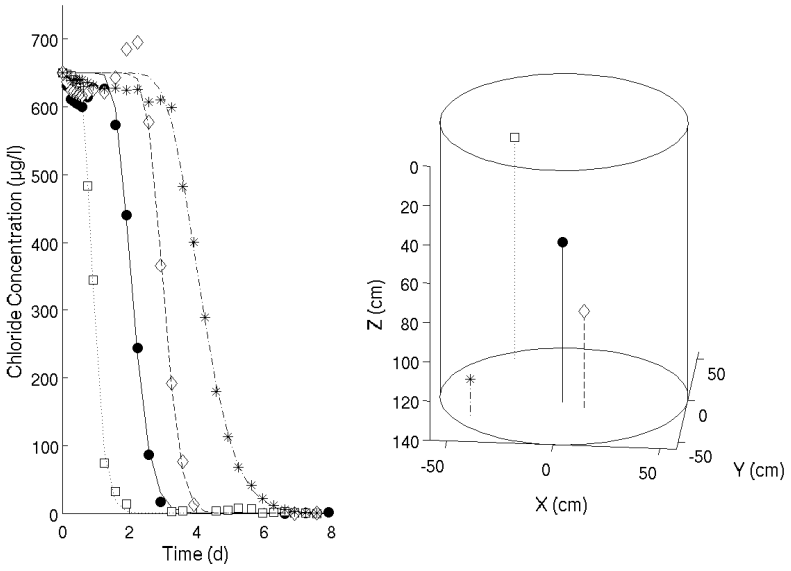


**Figure 4.7: (a) Four randomly selected ERT voxel breakthrough curves and the respective CDE-fit from experiment 2b; (b) the locations of the voxels that are depicted in a).**

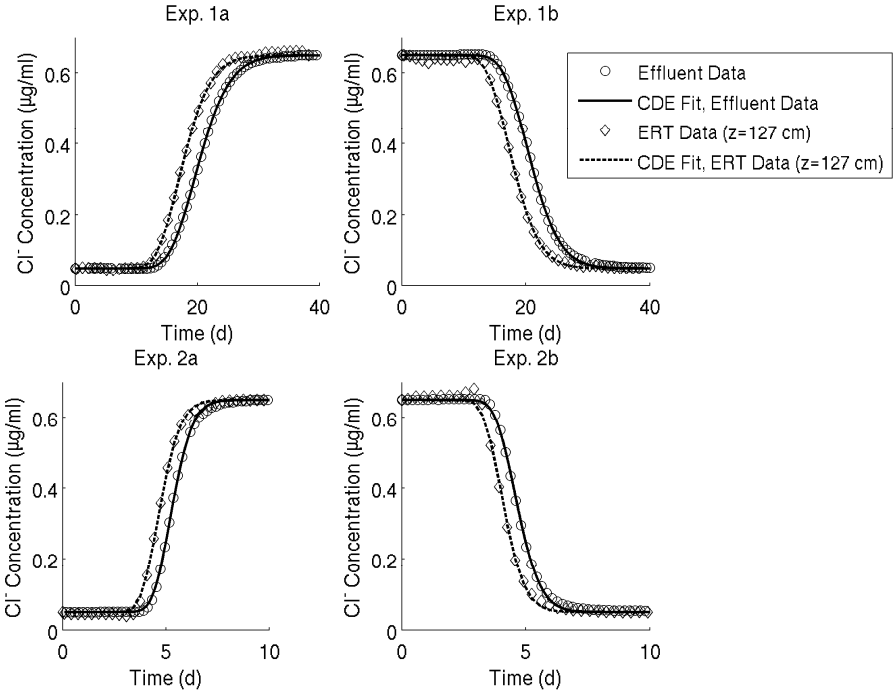


**Figure 4.8: The ERT-derived column-scale BTCs at $z$ = 127 cm and the corresponding CDE-fits. Likewise, the effluent BTCs and the corresponding CDE-fits are shown.**

### 4.3.5. Ground truth for the ERT-derived transport parameters

Supporting the good match between ERT and mass balance-derived tracer mass, the ERT-derived column-scale integral velocity $v_{col,ERT}$ corresponds well with the column-scale integral velocity derived from the effluent $v_{col,EFFL}$ (Figure 4.9). At this point, we postpone further inferences to the validity of the ERT-derived column-scale integral velocity to the next section. Figure 4.9 shows that the ERT-derived TDR-scale integral velocities $v_{tdr,ERT}$ correspond well with the TDR-derived integral velocities $v_{tdr,TDR}$. This is reflected in low mean (small bias) and standard deviations (high precision) of the TDR/ERT residuals $R_v$ (Table 4.1). Assuming a high accuracy of the TDR data with errors of approximately 1% (Huisman et al., 2008; Koestel et al., 2008) and considering the ERT sensitivity distribution (Figure 4.4), we conclude that at the outer edge of the column ERT is capable of quantitatively resolving spatial variations in integral velocities at the TDR scale. As the ERT voxel scale is only slightly smaller, we extend this conclusion to the voxel scale. Notably, the high flux experiment 2a, where the temporal smearing is larger than for the low-flux experiments, exhibits only a slightly larger bias and lower precision than the low-flux experiments. This suggests that temporal smearing is of minor importance for the interpretation of the ERT-derived velocities in our study. From Figure 4.10 and Table 4.1 it can be seen that the accuracy (-3% - 0%) and precision (8% - 10%) of the local ERT-derived TDR-scale velocities $u_{tdr,ERT}$ are reasonable. The impact of different amount of temporal smearing appears to be minor.

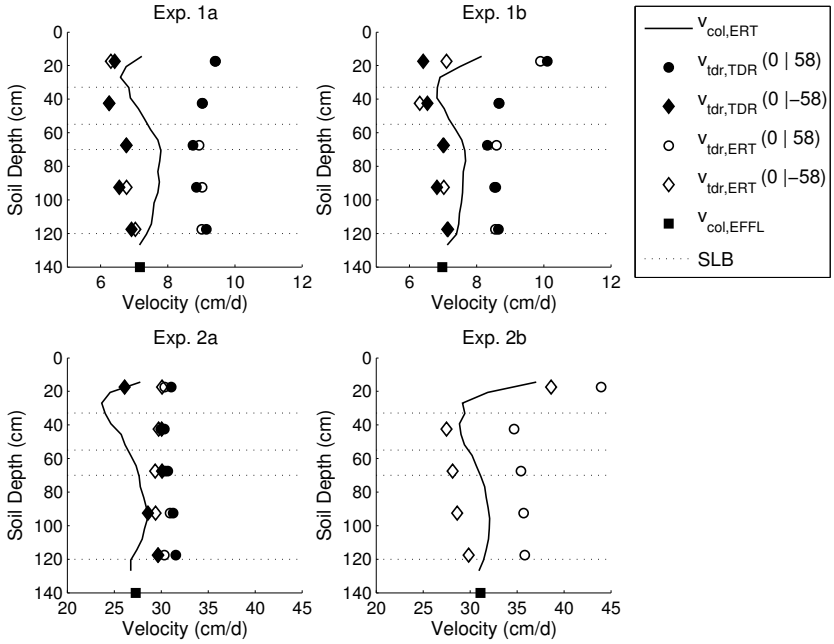


**Figure 4.9: The column-scale integral velocities $v_{col,ERT}$ together with the integral velocity for the effluent BTC $v_{col,EFFL}$. Additionally, the ERT and TDR-derived TDR-scale integral velocities are shown. The numbers in parentheses denote the XY-coordinates of the respective TDR probe in cm. SLB stands for soil layer boundary.**

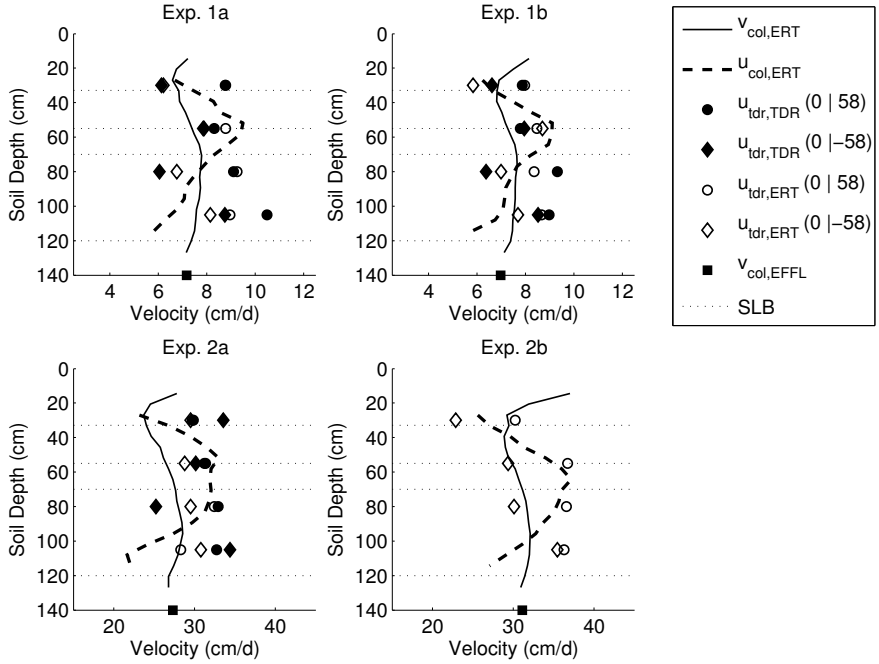


**Figure 4.10: The column-scale integral velocity vcol,ERT together with the column-scale local velocity ucol,ERT. Additionally, the ERT- and TDR-derived TDR-scale integral velocities are shown. The numbers in parentheses denote the XY-coordinates of the respective TDR probe in cm. SLB stands for soil layer boundary.**

The ERT-derived column-scale dispersivity $\lambda_{col,ERT}$ is similar to the column-scale dispersivity derived from the effluent measurements $\lambda_{col,EFFL}$. The validity of $\lambda_{col,ERT}$ is discussed in the next section. The ERT-derived TDR-scale dispersivities $\lambda_{tdr,ERT}$ tend to overestimate the dispersivities derived from TDR measurements $\lambda_{tdr,TDR}$, except for the deepest part of the soil column where the TDR and ERT-derived dispersivities correspond well (Figure 4.11). The mean of the TDR/ERT residuals for the dispersivities $R_\lambda$ indicates that the use of ERT overestimates the TDR-scale dispersivity $\lambda_{tdr,TDR}$ by 40% to 55% (Table 4.1) in regions with distance of approximately 20 cm or less to the column walls (regions with high ERT sensitivity, Figure 4.4). Furthermore, with a standard deviation of the residuals $R_\lambda$ of 32% to 96%, the precision of $\lambda_{tdr,ERT}$ is low (Table 4.1). Notably, the high-flux experiment 2a is inferior in accuracy and precision when compared to the low-flux experiments (Table 4.1). This finding is likely to be a result of the larger amount of temporal smearing inherent in the ERT data.

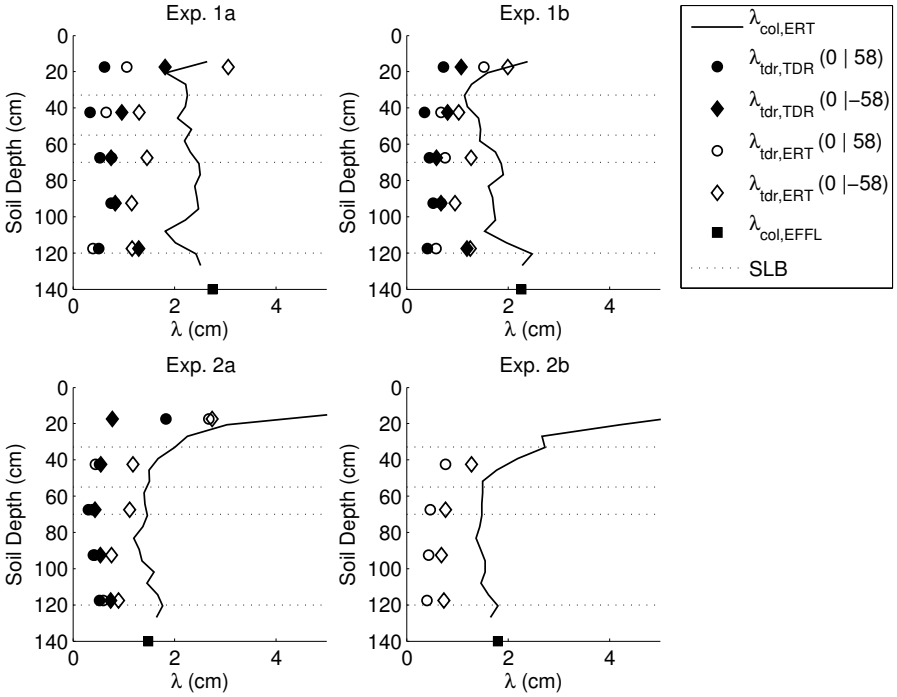


**Figure 4.11: The column-scale apparent dispersivities $\lambda_{col,ERT}$ compared to the apparent dispersivity $\lambda_{col,EFFL}$ from the effluent BTC. Additionally, the ERT- and TDR-derived TDR-scale apparent dispersivities are shown. The numbers in parentheses denote the XY-coordinates of the respective TDR probe in cm. SLB stands for soil layer boundary.**

### 4.3.6. Relationship between ERT sensitivity and ERT-derived transport parameters

In Figure 4.12, the statistics of the normalized CDE parameters that had been collected in the quadratic bins (see Figure 4.2), namely $\langle v_{n,bin,ERT} \rangle$, $\langle u_{n,bin,ERT} \rangle$, $\langle \lambda_{n,bin,ERT} \rangle$, std[$v_{n,bin,ERT}$>, std[$u_{n,bin,ERT}$], and std[$\lambda_{n,bin,ERT}$], from all four experiments are lumped into one graph. Figure 4.12 illustrates that the mean of the ERT-derived integral and local voxel-scale velocities, $\langle v_{n,bin,ERT} \rangle$ and $\langle u_{n,bin,ERT} \rangle$, remain approximately constant with changing ERT sensitivity. Assuming that the mean voxel-scale velocities in the regions with high ERT sensitivity (where the ERT data are ground-truthed by means of TDR data) are representative for the central parts of the column, we infer that the ERT-derived column-scale velocities, $v_{col,ERT}$ and $u_{col,ERT}$, represent the true column-scale velocities. In contrast, the corresponding standard deviations, std[$v_{n,bin,ERT}$] and std[$u_{n,bin,ERT}$], decrease with decreasing ERT-sensitivity. Assuming that the std[$v_{n,bin,ERT}$] and std[$u_{n,bin,ERT}$] next to the column wall are the most reliable measures of the variability, we conclude that the variability of the transport velocities is underestimated by ERT.

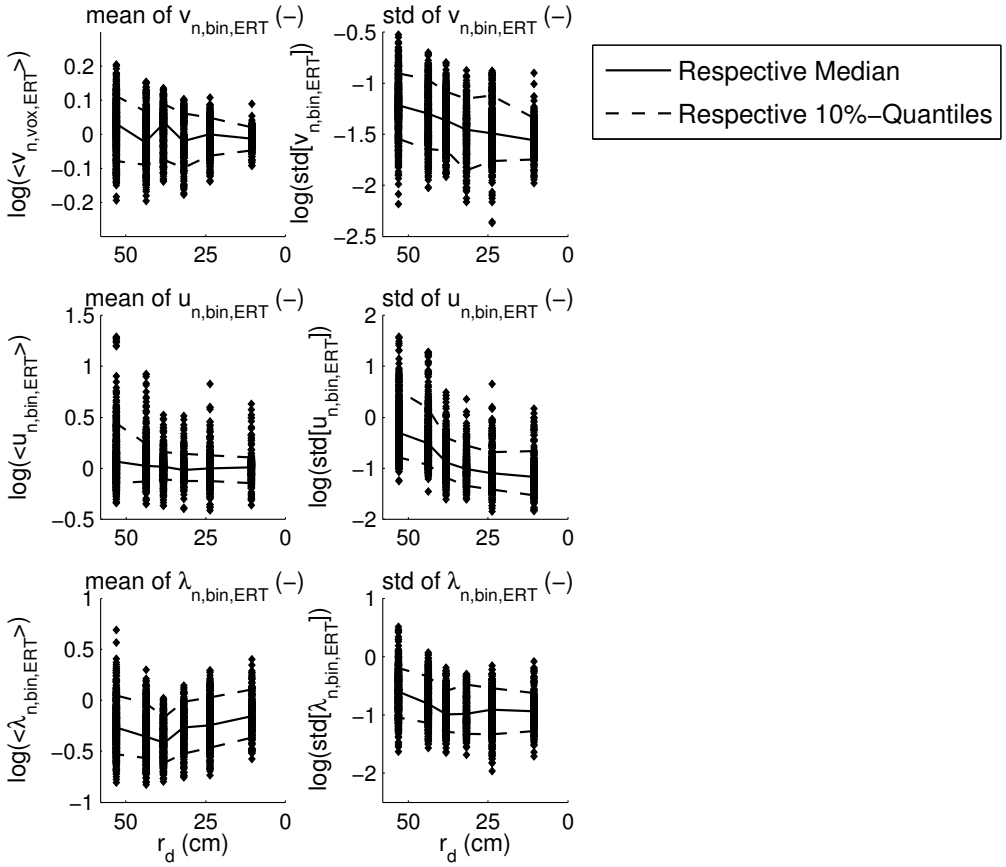


**Figure 4.12: The impact of the ERT sensitivity distribution on the mean and standard deviation of the normalized ERT-derived voxel-scale transport parameters that had been collected in the quadratic bins. The radial distance to the horizontal column center is applied as a proxy for the ERT sensitivity.**

From Figure 4.12 it can be seen that the dispersivities are log-normally distributed. Consequently, $\log(<\lambda_{n,bin,ERT}>)$ is smaller than zero. In contrast to the findings of Vanderborght et al. (2005) this shows that $<\lambda_{n,bin,ERT}>$ does not increase with decreasing ERT sensitivity. Considering that Vanderborght et al. (2005) used a similar electrode arrangement (with respect to the main transport direction) and the same ERT-regularization approach as in our study, we suspect that the differing results are related to the fact that they used a 2-D approach to invert (simulated) 3-D ERT data (see also the assessment of 3-D effects on 2-D inversion of ERT data by Nimmer et al., 2008). Due to the insensitivity of $<\lambda_{n,bin,ERT}>$ with respect to the ERT sensitivity we may assume that the ERT-derived voxel-scale dispersivities $\lambda_{vox,ERT}$ in the central column regions are similarly biased as the ones at the TDR locations (40% - 55% overestimation). Finally, for the sake of completeness, we note that $\text{std}[\lambda_{n,bin,ERT}]$ was similarly insensitive to the ERT sensitivity as $<\lambda_{n,bin,ERT}>$.

## 4.4. Summary and Conclusions

In this study, we investigated the potential and limitations of (smoothness-constrained) ERT to quantitatively determine and compare transport characteristics of four different tracer displacement experiments in a large unsaturated and undisturbed soil column. We obtained an excellent tracer mass recovery for all four experiments through adjustment of

the ERT inversions to an error level equal to the largest average reciprocal error obtained for the four experiments.

The ERT-derived apparent velocities agree well with the ones derived from the TDR and effluent data. Furthermore, the mean ERT-derived voxel-scale velocities were insensitive to the ERT sensitivity distribution. From these two findings it follows that, on average, the voxel-scale velocities are not biased. Furthermore, we infer that the ERT-derived column-scale velocities are good estimators for the true column-scale velocities. The variability of voxel-scale velocities was observed to decrease with decreasing ERT sensitivity. Presuming that the velocity variability is estimated best in the high-sensitivity regions next to the column wall, it follows that the ERT-derived voxel-scale velocity variability underestimates the true value. The ERT-derived transport velocities were found to be only slightly sensitive to the different amount of temporal smearing between the low-flux and the high-flux experiments.

The ERT-derived TDR-scale dispersivities were found to be biased, overestimating the TDR-derived ones except for the bottommost TDR probes. In addition, the precision of the ERT-derived dispersivities was inferior to the TDR-derived ones. The mean ERT-derived voxel-scale dispersivities were merely affected by the ERT sensitivity distribution. From this, we infer that the voxel-scale dispersivities are subject to a similar bias in the entire column as the one found at the TDR location. It follows that the interpretation of the ERT-derived column-scale dispersivities has to be carried out with caution regardless of the fact that they match well with the dispersivity found from the analysis of the effluent data. The ERT-derived dispersivities were found to be sensitive to temporal smearing.

Our study shows that the (smoothness-constrained) ERT-derived velocities are well suited to compare 3-D spatio-temporal transport characteristics of different tracer experiments, but that ERT underestimates the voxel-scale velocity variability. The ERT-derived dispersivities are biased, less precise and, therefore, less valuable for transport characterization. These general findings confirm results of previous studies (e.g. Singha and Gorelick, 2005; Vanderborght et al., 2005). As a workaround, ERT may be combined with another complementary method, for example with ground penetrating radar (GPR) as in the studies of Binley et al. (2002b) or Looms et al. (2008). In this way, the amount of applied regularization in the ERT inverse problem could be reduced and GPR could compensate for information losses in regions with low ERT sensitivity (see e.g. Linde et al., 2006). The joint application of ERT and GPR may also help to resolve the ambiguity between solute-concentration and water-content related changes in bulk electrical conductivity. In this way, the setup presented here may be used to investigate solute transport under realistic boundary conditions since hydraulic steady-state conditions would no longer be required. Thus, quantitative solute transport monitoring with ERT in the field could be realized.

In this study, we investigated the validity of ERT-derived transport parameters by means of the mass balance, comparison with TDR data, and dependence on ERT sensitivity. For future studies, the joint application of ERT with multi-compartment sampling, dye tracer imaging or investigations by means of numerical models may be fruitful extensions to the approach described here. In addition, other tools for solute transport characterization such as the dilution index (Kitanidis, 1994; Cirpka and Kitanidis, 2002) or the leaching surface (de Rooij and Stagnitti, 2002; de Rooij et al., 2006) may prove to be useful in this context.

A drawback of our study is that the appraisal of the uncertainty of the ERT image data and the subsequently derived transport parameters is incomplete. In our study, we investigated

the accuracy of ERT by means of the mass balance and ground truths with TDR and effluent data. However, this does not provide a spatially resolved measure of uncertainty. Such a measure of uncertainty could be achieved by means of the model covariance matrix, for instance in the framework of Bayesian ERT inversion approaches; however, these approaches are computationally intensive. Future investigation on their value in non-linear parameter estimation deserves further attention.

# 5. Non-invasive 3-D transport characterization in a sandy soil using ERT II: Transport process inference*

## 5.1. Introduction

Quantitative prediction of solute transport through the unsaturated zone is necessary to improve the managing of our environmental resources. At present, such predictions are only possible in an approximate manner as solute transport through structured soil is still far from being understood quantitatively (see e.g. Vogel and Roth, 2003). It is especially difficult to predict the solute spreading (Vanderborght and Vereecken, 2007a). In this context, the major drivers are heterogeneities in the transport velocities (e.g. Biggar and Nielsen, 1976; Yeh et al., 1985; Ghodrati and Jury, 1992; Ursino et al., 2001; Vogel and Roth, 2003; Vogel et al., 2006). For advection-dominated transport processes, the solute spread is determined by sub-scale velocity heterogeneities (Jury and Sposito, 1985). Moreover, the velocity of a solute particle may change along its travel path, which, in the literature about vadose zone transport, is referred to as lateral solute mixing (Flühler et al., 1996). The latter is related to the evolution of the solute spread with travel distance (Jury and Roth, 1990). It follows that the knowledge of the correct mixing regime improves predictions about solute transport. In vadose zone literature, the mixing regime is classified as convective-dispersive (CD) for complete lateral mixing (Taylor, 1953), stochastic-convective (SC) for negligible lateral mixing (Simmons, 1982), or as a transition regime between these two (Jury and Roth, 1990).

The mixing regime is often determined by quantifying the evolution of the solute spread with travel distance (e.g. Jury and Roth, 1990). In this context, apparent (longitudinal) dispersivities have proved to be useful (Vanderborght and Vereecken, 2007b). However, strictly speaking, this approach requires the assumption that variability in the local velocities is constant for all depths (Vanderborght and Vereecken, 2007a). Basically, the variability of the velocity field is needed to explicitly identify the mixing regime. As the latter is seldom available, the apparent dispersivities, which are derived from breakthrough curves that are measured at different depths and are a measure of the solute spread, are usually relied on to derive the mixing regime.

The prediction of the apparent dispersivity is aggravated by the fact that its magnitude is subject to the lateral scale over which the solute breakthrough curve (BTC) is sampled. In general, an increase in apparent dispersivity with lateral observation scale has been found (van Wesenbeeck and Kachanoski, 1991 and 1994; Ward et al., 1995; Javaux and Vanclooster, 2003). Persson et al. (2005) illustrated that the dispersivity-increase may occur in sudden jumps. However, the study of Jacques et al. (1997) demonstrates that there are also soils that do not exhibit a lateral scale-dependency of the apparent dispersivity. The basic mechanism leading to the behavior described above is the sampling of additional, larger-scale velocity heterogeneity with increasing lateral observation scale. However, for a quantitative prediction of the lateral-scale effect, the statistics of the respective velocity field have to be known (Jury and Sposito, 1985). Information on the

* Adapted from Koestel, J., J. Vanderborght, M. Javaux, A. Kemna, A. Binley and H. Vereecken. Non-invasive 3-D transport characterization in a sandy soil using ERT II: Transport process inference. Vadose Zone Journal. Accepted for publication.

velocity field may also prove to be useful to examine changes of the mixing regime with lateral observation scale (Javaux and Vanclooster, 2003).

The prediction of apparent dispersivity is not only complicated by its sensitivity to the lateral observation scale; other important influencing factors are the initial and boundary conditions. Several studies have shown that the apparent dispersivity was correlated with the applied water flux density. This correlation could be negative (Padilla et al., 1999; Nützmann et al., 2002; Toride et al., 2003), positive (Maciejewski, 1993), or the relation between flux density and apparent dispersivity could be non-monotonic with a minimum for a certain water flux (Roth and Hammel, 1996; Javaux et al., 2006). Analogously, the mixing regime has been observed to be sensitive to the applied water flux density and the amount of lateral mixing may increase (e.g. Khan and Jury, 1990; Forrer et al., 1999; Vanderborght et al., 2001) or decrease (Ursino et al., 2001; Persson et al., 2005) for larger water flux densities. Some studies revealed no or merely weak relationship between water flux density and mixing regime (Vanderborght et al., 1997; Javaux and Vanclooster, 2003).

Due to the lack of adequate measurement methods, all the above mentioned studies dispense with 3-D spatially resolved data on velocity field (see chapter 4). Knowledge of the latter would add crucial insight into the relation between apparent dispersivity and mixing regime, lateral observation scale, and boundary conditions. It would also be helpful to relate these transport characteristics to the spatial distribution of soil hydraulic properties and structural features. In chapter 4 we have shown that ERT-derived apparent convection-dispersion equation (CDE) parameters, namely the apparent velocity and dispersivity, are able to quantitatively characterize the 3-D evolution of the considered tracer fronts subject to ERT-specific limitations regarding resolution and image reconstruction issues.

In this chapter we investigate four tracer displacement experiments in an unsaturated undisturbed soil column under hydraulic steady state conditions by means of ERT-derived apparent CDE parameters with 3-D resolution. The chapter builds on the previous one which focuses on the validity of the ERT-derived CDE parameters. In contrast, in this chapter, here, we place emphasis on the solute transport characterization. We use TDR and tensiometer data to derive the hydrologic state variables corresponding to the respective hydraulic steady state conditions. We then evaluate links between solute transport characteristics at different lateral scales, hydrologic state variables, and soil structural features in the topsoil. Furthermore, we infer the mixing regime and apply a newly introduced up-scaling approach which calculates the increase of apparent dispersivity with lateral observation scale on basis of the velocity field statistics.

## 5.2. Materials and Methods

### 5.2.1. Experimental Setup and Soil

We investigated and compared the 3-D spatio-temporal evolution of solute fronts of four chloride displacement experiments under two distinct steady state flow rates (1.5 cm/d and 6.5 cm/d) through a large undisturbed soil column (140 cm in height, 116 cm in diameter, Figure 5.1b). The soil was unsaturated (except for the bottommost part of the column) for both water flux densities. As we did not apply suction at the bottom boundary it remained water saturated (i.e. acting as a seepage face). The four experiments are, in the following, referred to as experiments 1a and 1b (or low-flux experiments) for the lower irrigation rate and experiments 2a and 2b (or high-flux experiments) for the higher irrigation rate. We made use of the electrical conductivity contrast, which was caused by the infiltration of a

salt tracer solution ($CaCl_2$), and applied time-lapse 3-D ERT to capture the tracer transport. The ERT electrode-array comprised 212 stainless-steel electrodes which were installed in the column wall (Figure 5.1b). In addition, we used 10 TDR-probes in 5 different depths to gather ERT-independent solute breakthrough curves and to determine the water content. The location of 5 of the TDR-probes is depicted in Figure 5.1b. The other 5 probes were installed diametrically opposite. Next to each TDR-probe, a tensiometer was installed providing measurements of the suction head. The experimental design, the measurement equipment, and the data acquisition and processing are described in detail in chapter 4.2.

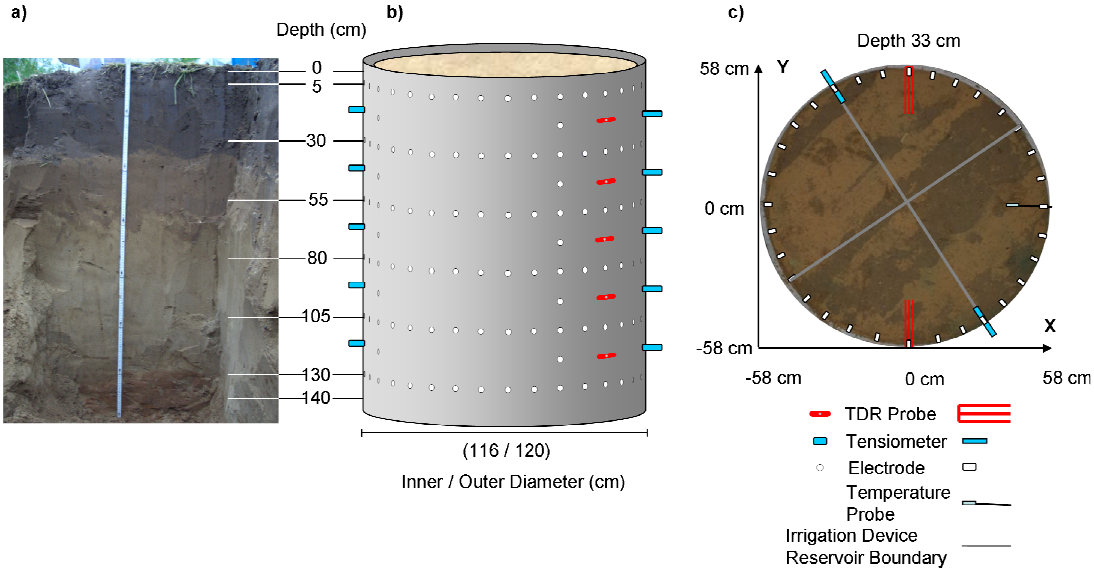


**Figure 5.1: (a) Vertical soil profile at the Kaldenkirchen field site. The location of the six electrode rings with respect to the soil horizons are indicated; (b) the soil column with the locations of electrodes, TDR probes and tensiometers; (c) a horizontal cross-section through the soil column in depth $z$ = 33 cm. Electrode, TDR probe, and tensiometer locations are depicted as well as the positions of the four irrigation device reservoirs.**

The undisturbed soil sample inside the column (Figure 5.1a and c) was excavated from an agricultural field site near Kaldenkirchen (Germany). Information on the excavation procedure can be obtained from chapter 4.2. The soil parent material consists of aeolian sands. Table 5.1 lists the soil texture, bulk density, and porosity sampled at the field site. The saturated hydraulic conductivity was sampled from the column itself by means of 100 cm³ steel cylinders. From Figure 5.1a, a sharp boundary between the plow layer and the subsoil (depth ≈ 33 cm) can be observed. When excavating the column, layer by layer at the end of the experiments, we uncovered an undulation of this boundary (Figure 5.1c). The undulation was oriented perpendicular to the plow direction and was identified as part of a structural feature generated during the plowing process. In addition, we found compacted platy macro-aggregates at the bottom of the plow horizon (depth 30 – 35 cm). This is often observed in plowed soil and referred to as plow pan.

**Table 5.1: Soil horizons and the corresponding textures, bulk densities (BD), saturated hydraulic conductivities ($K_s$), and porosities.**

| Horizon | Soil Depth | Sand (%) 67 – 2,000 µm | Silt (%) 2 - 67 µm | Clay (%) < 2 µm | BD (g/cm³) | $K_s$ ($\log_{10}$[cm/d]) | Porosity (%) |
|---|---|---|---|---|---|---|---|
| Ap | 0-33 cm | 72.7 | 22.2 | 5.5 | 1.60 | 0.7 – 2.9 | 40.1 |
| Bv1 | 33-55 cm | 76.6 | 21.4 | 2.0 | 1.66 | 2.0 – 2.9 | 37.5 |
| Bv2 | 55-70 cm | 79.1 | 19.7 | 1.2 | 1.60 | - | 40.6 |
| Bv3 | 70-120 cm | 84.3 | 14.3 | 1.0 | 1.66 | 1.8 – 3.0 | 38.0 |
| IIBv | > 120 cm | 49.0 | 40.7 | 10.3 | 1.79 | 1.7 – 4.0 | 31.8 |

### 5.2.2. Irrigation Device

We used a piston pump which supplied the water to a circular irrigation device consisting of four reservoirs (quadrants), each connected to 121 needles (484 in total) which were evenly distributed over the soil surface. During an initial testing phase we found that the coefficient of variation of the spatial irrigation distribution was 0.29 - 0.32 for the low-flux and 0.17 - 0.2 for the high-flux experiments. The spatial irrigation homogeneity was very sensitive to tilting and gas bubbles inside the device. In one extreme case during the testing phase this lead to an irrigation rate ratio of 1:2 between two of the four reservoirs. The appearance of air bubbles could not be avoided during the course of the experiments. As we were not able to check the irrigation homogeneity while the device was mounted, we cannot rule out irrigation heterogeneity as an influencing quantity on the spatio-temporal characteristics of the solute transport. The location of the irrigation device reservoirs is depicted in Figure 5.1c.

### 5.2.3. Deriving the Unsaturated Hydraulic Conductivity

In this section we describe how the 1-D unsaturated hydraulic conductivity $K(h)$ (cm/d) was derived from tensiometer measurements. We assumed that the pressure head $h_z$ (cm) was approximately constant in each horizontal cross-section. In depths $z$ (cm) where two tensiometers were installed, we obtained $h_z$ by taking the average of the observed pressure heads. Note that we defined $z$ to be positive in the downward direction. We assigned a pressure head of 0 to the depth $z$ = 140 cm due to the seepage face boundary condition. Then, we interpolated the pressure head profile $h_z$ using a cubic spline function. To avoid extrapolation, we did not consider voxel layers above the topmost tensiometers. The 1-D column-scale unsaturated hydraulic conductivities $K(h_z)$ were calculated according to the Darcy-Buckingham law using $h_z$ and the water flux density $q$ (cm/d) of the corresponding experiment (see e.g. Hillel, 1980).

### 5.2.4. Definition of the Apparent CDE Parameters and Scales

We derived apparent CDE parameters from the solute breakthrough curves as described in chapter 4. We distinguished two vertical scales: the integral scale which is the distance between the upper soil surface and the depth of observation and the local scale which refers to a distance between two observation depths. The velocity at the integral scale is denoted with $v$ (cm/d) and the local-scale velocity with $u$ (cm/d). The former refers to the mean velocity with which the tracer front traveled from the top of the column to the corresponding depth. The latter is derived from two integral velocities at the same

horizontal location but separated by a vertical distance of 25 cm (see chapter 4). The apparent dispersivity $\lambda$ (cm) is only derived for the integral scale. Local-scale dispersivities were not considered.

Furthermore, we distinguished three horizontal scales, namely the voxel, the TDR, and the column scale. The voxel scale (approximately 7 cm) corresponds to the square root of the horizontal area of one triangular patch of finite elements used for the ERT image reconstruction (chapter 4). It is denoted with the subscript *'vox'*. The TDR-scale (approximately 9 cm) complies with the support volume of the TDR-probes ($7.5 \times 7.5 \times \pi \times 18.8$ cm³). It is labeled with the subscript *'tdr'*. ERT-derived CDE parameters at the TDR scale were obtained on basis of the volume-weighted average of all voxel-scale BTCs intersecting the TDR support volume in the considered depth. Finally, the subscript *'col'* denotes the scale (approximately 100 cm) corresponding to the column's horizontal cross-section ($58 \times 58 \times \pi$ cm²). The ERT-derived column-scale CDE parameters were derived from column scale averaged breakthrough curves, i.e., the area weighted average of all voxel scale BTCs at the considered depth. The scales are illustrated in further detail by Figure 4.1.

In addition to the label of the corresponding horizontal scale, the transport parameters are tagged with subscripts referring to the measurement method that was used to obtain them, namely '*ERT*', '*TDR*', and '*EFFL*'. The latter abbreviation denotes the data measured in the effluent. As an example, $v_{tdr,ERT}$ refers to the ERT-derived integral velocity at the TDR scale. Table 5.2 provides an overview of all derived transport parameters with respect to scale and measurement method.

Finally, we calculated the column-scale piston-flow local velocity $u_{col,TDR}$ as

$$u_{col,TDR} = \frac{q}{\theta_{col}}, \tag{5.1}$$

where $\theta_{col}$ (cm³/cm³) is the average volumetric water content derived from the two TDR probes at each depth.

**Table 5.2: The apparent CDE parameters that are considered in our study with respect to horizontal scale and measurement method for which the parameters are available.**

| | Integral velocity $v$ (cm/d) | Local velocity $u$ (cm/d) | Dispersivity $\lambda$ (cm) |
|---|---|---|---|
| Voxel scale (subscript 'vox') | ERT | ERT | ERT |
| TDR scale (subscript 'tdr') | TDR, ERT | TDR, ERT | TDR, ERT |
| Column scale (subscript 'col') | ERT, Effluent | TDR*, ERT | ERT, Effluent |

* the TDR-derived local velocities refer to the piston flow velocity $u_{col,TDR}$

## 5.2.5. Investigation of the Mixing Regime

As already discussed, the apparent dispersivity is an indicator for the mixing regime. A linear increase of the apparent dispersivity $\lambda$ with travel distance indicates that lateral mixing is not complete and the solute transport process can be described as stochastic-convective. In contrast, a constant apparent dispersivity indicates that solute spreading can be described as a diffusive or Fickian process, in other words, that the transport can be

characterized as convective-dispersive (e.g. Roth and Hammel, 1996; Vanderborght et al., 2001).

However the apparent dispersivity can only be used as an indicator for the mixing regime under the assumption that the local velocity variability remains constant and does not change with depth. Strictly speaking, the variability in the local velocities should be investigated in addition to the variability in the integral velocities which provides similar information about the mixing regime as the apparent dispersivity. In our study, we quantified the velocity-variability by means of the coefficient of variation of the voxel-scale integral velocities $CV_v$ and the voxel-scale local velocities $CV_u$:

$$CV_v = \frac{std\left[v_{vox,ERT}\right]}{\left\langle v_{vox,ERT}\right\rangle} \quad \text{and} \quad CV_u = \frac{std\left[u_{vox,ERT}\right]}{\left\langle u_{vox,ERT}\right\rangle}. \tag{5.2a and b}$$

Lateral mixing refers to a change of the relative local velocity of a solute particle (relative to the mean local velocity at a certain depth) along the particle trajectory. A decreasing $CV_v$ with travel distance indicates lateral mixing if, at the same time, the corresponding $CV_u$ remains constant. For a constant $CV_u$ with depth, a constant $CV_v$ indicates that no lateral mixing occurs and the relative local velocity of a particle does not change along the particle trajectory (e.g. Javaux and Vanclooster, 2003). Together, the variability in the integral and in the local velocities provides a better measure to identify the mixing regime.

### 5.2.6. Lateral Up-Scaling Approach for the Apparent Dispersivity

In this section we present an up-scaling approach to derive column-scale velocities and dispersivities from ERT-derived voxel-scale apparent transport parameters. If we assume that the solute flux is proportional to the transport velocity, the voxel-scale velocity $v_{vox,ERT}$ can be up-scaled to the column-scale velocity $v^*_{col,ERT}$ by calculating the area-weighted mean of the voxel-scale velocities $v_{vox,ERT}$. Here, the asterisk denotes that $v^*_{col,ERT}$ is the up-scaled column-scale velocity in contrast to $v_{col,ERT,}$ which is the velocity obtained from the column-scale BTC.

Similarly, an up-scaled dispersivity, $\lambda^*_{col,ERT}$, can be derived from smaller scale dispersivities and the statistics of the voxel-scale velocities. The column-scale dispersivity $\lambda^*_{col,ERT}$ can, in general, be defined to consist of two terms:

$$\lambda^*_{col,ERT} = \left\langle \lambda_{vox,ERT} \right\rangle + \lambda_{adv,ERT} \tag{5.3}$$

where, $\langle\lambda_{vox,ERT}\rangle$ is the contribution to the column-scale dispersivity of dispersion that is observed at the voxel-scale and $\lambda_{adv,ERT}$ refers to the advective dispersivity, i.e. the dispersivity increment between voxel-scale and column scale which is generated by variability of the voxel-scale velocities. $<\lambda_{vox,ERT}>$ and $\lambda_{adv,ERT}$ were derived assuming that the local solute flux is proportional to the transport velocity and the derivations of the following equations are given in the Appendix.

$<\lambda_{vox,ERT}>$ is obtained from:

$$\left\langle \lambda_{vox,ERT} \right\rangle = \frac{v_{col,ERT} \sum_{\mathrm{n_{vox}}} \frac{\lambda_{vox,ERT,k}}{v_{\mathrm{vox,ERT,k}}}}{\mathrm{n_{vox}}} \tag{5.4}$$

where the index k denotes the $k^{\mathrm{th}}$ voxel in the column's cross-section and $n_{vox}$ is the number of voxels in a cross-section. The advective dispersivity $\lambda_{adv,ERT}$ is calculated according to:

$$\lambda_{adv,ERT} = \frac{z}{2}\left( \frac{v_{col,ERT} \sum_{\mathrm{n_{vox}}} \frac{1}{v_{vox,ERT,k}}}{\mathrm{n_{vox}}} - 1 \right) \tag{5.5}$$

At the end of this section we point out that the up-scaling approach does not only apply to ERT-derived data but is generally valid as long as the discussed underlying assumptions are met.

### 5.2.7. Investigating the Lateral Observation-Scale Dependency of the ERT-Derived Apparent Dispersivities

Investigating the lateral observation-scale dependency of the up-scaled dispersivities, $\lambda^*$ was calculated for a range of lateral observation scales $s$ (cm). The latter corresponds with the length of the sides of square cross-sections which we superimposed to the ERT-derived apparent CDE parameters within each horizontal cross-section (for illustration see Figure 4.2). The up-scaled dispersivity $\lambda^*_s$ was calculated using the same equations as $\lambda^*_{col}$ but using only voxels within a square with side-lengths $s$.

## 5.3. Results and discussion

### 5.3.1. Hydrologic Steady-State Conditions

For all experiments, the water content was larger in the top and in the bottom parts of the soil column than in the middle parts of the soil column (Figure 5.2). The corresponding pressure head shows a similar distribution (Figure 5.3a). The large water content at the bottom is a result of the presence of a seepage-face bottom boundary condition. The large pressure heads near the column's top hint to a hydraulically less conductive layer within the topsoil, most likely the compacted layer at the bottom of the plow horizon. In the topmost 70 cm of the soil column a significant change in water content of up to 5 volume percent is observable between the two flow rates (Figure 5.2). Other notable features of the hydrologic state variables are that (i) the shape of the pressure head profiles clearly differ between the low and the high-flux experiments (Figure 5.3a) and (ii) that the TDR probes detected considerable lateral water content differences for soil depths of 60 cm < $z$ < 100 cm (Figure 5.2) which hints to heterogeneities in the soil hydraulic properties within the respective horizontal cross-sections.

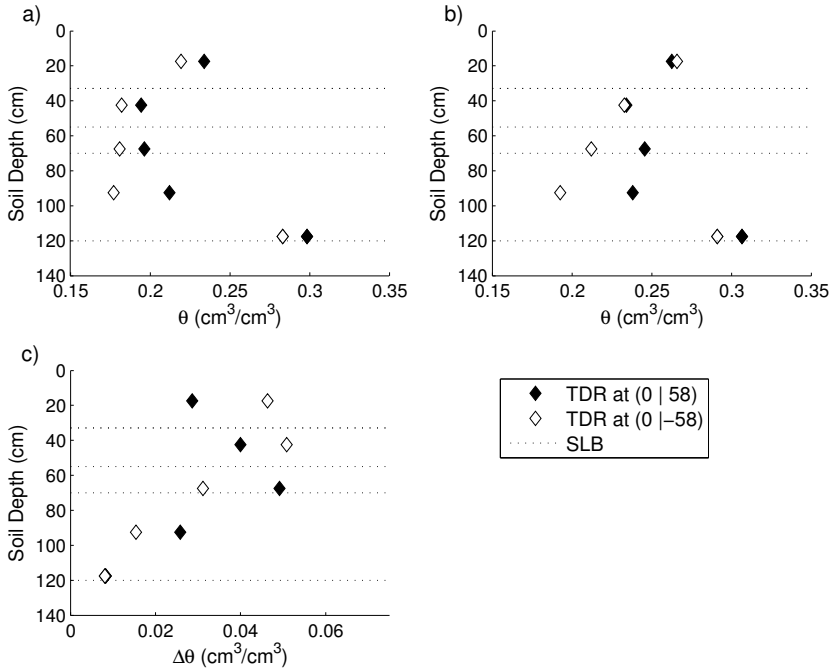


**Figure 5.2: (a) The TDR derived water content for the low-flux experiments, (b) for the high-flux experiments, and (c) the difference in water content between the high and low-flux experiments. SLB stands for soil layer boundary.**

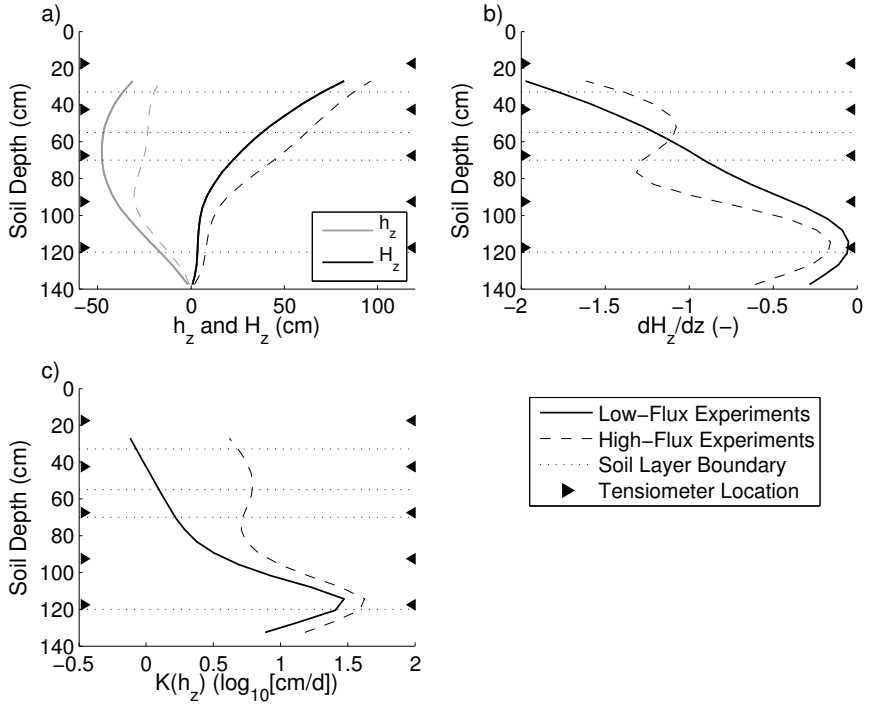


**Figure 5.3: (a) The 1-D pressure and hydraulic head, $h_z$ and $H_z$, (b) the hydraulic head gradients $dH_z/dz$, and (c) the unsaturated hydraulic conductivities $K(h_z)$ for the low and the high-flux experiments. Additionally, the locations of the TDR probes and the soil layer boundaries are shown.**

Figure 5.3b illustrates changes in the profile of the hydraulic head gradients between the low and the high-flux experiments: for the low-flux experiments, the hydraulic head gradients increase steadily from values smaller than -1 in the topsoil to values larger than -0.5 at depths $z$ > 100 cm; for the high–flux experiments, a prominent kink in the *dH/dz* profile is visible in a depth of 70 cm. Together with the augmented increase in water content in this depth between the low and the high-flux experiments (see Figure 5.2c), it appears that a secondary hydraulically less permeable layer exists at $z$ = 70 cm for the high-flux experiments. As a result, the gap between the low and the high-flux unsaturated conductivities (in the log-domain) is especially large above a depth of 70 cm where also the increase in water content is the largest (Figure 5.2 and Figure 5.3c). The deviations in the hydraulic conditions suggest that also the solute transport characteristics differ between the low and high-flux experiments.

### 5.3.2. Apparent Column-Scale CDE Parameters

Figure 5.4 depicts that the ERT-derived column-scale integral ($v_{col,ERT}$) and local velocity ($u_{col,ERT}$) profiles of the low-flux experiments (1a and 1b) are similar. Likewise, the velocity profiles of the high-flux experiments (2a and 2b) bear resemblance. All profiles indicate slower transport in the top and bottom regions of the column and faster transport in the vertical middle. This is consistent with the water content profile (Figure 5.2) as under constant flux density, the local transport velocity of an inert tracer is inversely related to the water content provided that the entire wetted pore space contributes equally to the transport.

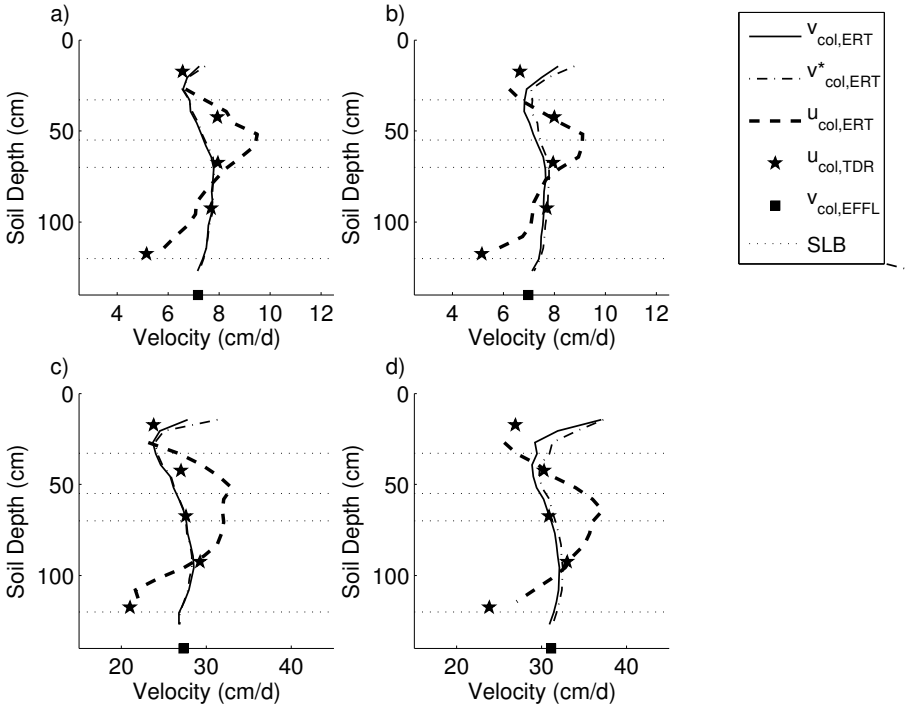


**Figure 5.4: The ERT-derived column-scale integral velocity $v_{col,ERT}$ and the up-scaled column-scale integral velocity $v^*_{col,ERT}$ for experiments 1a (a), 1b (b), 2a (c), and 2b (d). Additionally the ERT-derived column-scale local velocity $u_{col,ERT}$ and the TDR-derived piston flow velocities $u_{col,TDR}$ are shown. SLB stands for soil layer boundary.**

The local velocities $u_{col,ERT}$ indicate that accelerated transport occurred between depths of $z = 30$ and $z = 70$ cm for the low-flux experiments (Figure 5.4). For the high-flux experiments (2a and 2b), the domain of the accelerated transport was larger and extended from a depth of $z = 30$ to $z = 100$ cm. An explanation for this may be the smaller increase in water content in depth $z = 92.5$ cm between low and high-flux experiments (Figure 5.2c) together with a (in absolute terms) larger hydraulic gradient with respect to the corresponding increase of unsaturated hydraulic conductivity (Figure 5.3c).

The ERT-derived local velocities $u_{col,ERT}$ correspond well with the piston flow velocities $u_{col,TDR}$ (Figure 5.4) except for the high-flux experiments at 67.5 cm depth. One explanation for the mismatch could be that the water content at the TDR locations was not representative for the entire column cross-section at this depth but overestimated it by 0.035 $cm^3/cm^3$. Alternatively, the residuals between $u_{col,ERT}$ and $u_{col,TDR}$ may indicate that the solute transport occurred only in a part of the wetted pore space (e.g. Jury and Flühler, 1992). Notably, at 67.5 cm depth, an increase in the hydraulic head gradient (in absolute terms) and increased water contents for the high-flux experiments (as compared to the low-flux experiments) were observed. However, the discrepancy between $u_{col,ERT}$ and $u_{col,TDR}$ may as well be related to differences in vertical distance over which $u_{col,TDR}$ (approximately 7.5 cm) and $u_{col,ERT}$ (approximately 25 cm) were derived.

Figure 5.5 shows the ERT-derived column-scale dispersivities $\lambda_{col,ERT}$. We suspect that the large values in the topsoil ($z < 30$ cm) either stem from spatial irrigation heterogeneities or from artifacts caused by the applied ERT inversion approach: as the tracer fronts are very sharp near the top the bulk electrical conductivity gradients are especially large and the ERT-derived BTCs are disproportionately smoothed. Neglecting the topmost 30 cm, the column-scale dispersivities remain approximately constant with depth. In addition, it can be seen that the dispersivity is larger for the low-flux experiment and, hence, for lower water contents. This finding is in accordance with the results of the majority of lab scale experiments (Padilla et al., 1999; Nützmann et al., 2002; Sato et al., 2003; Toride et al., 2003). The column-scale dispersivity profile is further discussed in section entitled ‘Inference to Mixing Regime’.

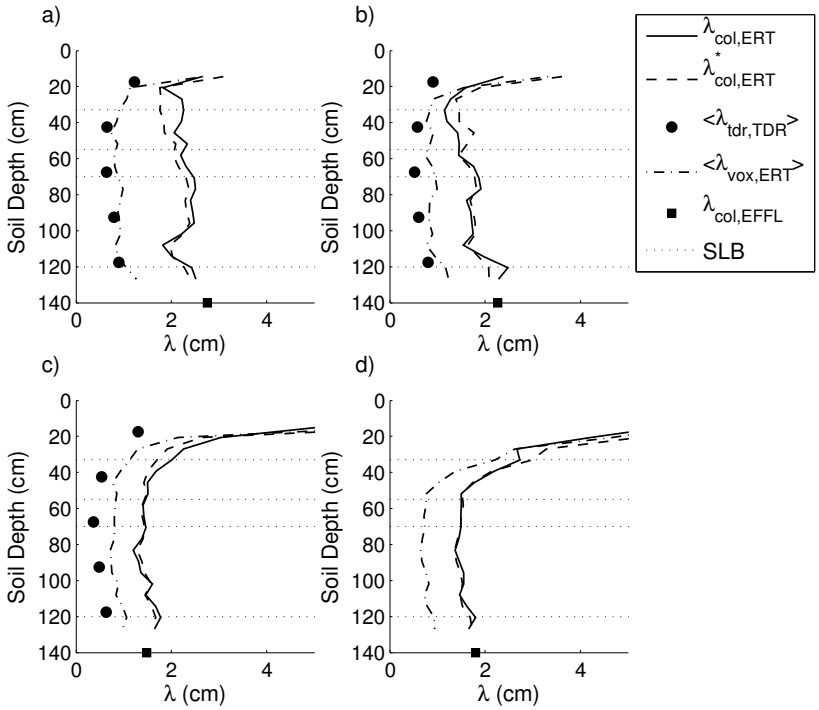


**Figure 5.5: The ERT-derived column-scale dispersivities $\lambda_{col,ERT}$ together with the apparent dispersivity $\lambda_{col,EFFL}$ of the effluent BTC for experiments 1a (a), 1b (b), 2a (c), and 2b (d). Furthermore, the averaged TDR-derived TDR-scale dispersivities $<\lambda_{tdr,TDR}>$ and the averaged ERT-derived voxel-scale dispersivity $<\lambda_{vox,ERT}>$ are shown. Additionally, the up-scaled column-scale dispersivity $\lambda^*_{col,ERT}$ and the the dispersivity of the effluent BTC $\lambda_{col,ERT}$ are depicted. SLB stands for soil layer boundary.**

### 5.3.3. Apparent Voxel-Scale CDE Parameters

Figure 5.6 shows horizontal cross-sections of the logarithms of the ERT-derived voxel-scale integral velocities $v_{vox,ERT}$ normalized to the corresponding column-scale integral velocity for the effluent BTC $v_{col,EFFL}$. Despite the considerable increase in water content, the $v_{vox,ERT}$-distributions of all experiments are similar. All $v_{vox,ERT}$ patterns are aligned to the soil structural feature excavated at the soil layer interface between plow layer and subsoil (see Figure 5.1c). The addressed alignment of the integral velocity patterns is most developed for larger depths (Figure 5.6, $z$ = 125). Such transport patterns are typical for plowed soil (Petersen et al., 1997; Petersen et al., 2001; Öhrström et al., 2004; Coquet et al., 2005). A more detailed visual inspection yields that experiments 1a and 1b (low flux) show $v_{vox,ERT}$ features which distinguish them from the experiments 2a and 2b (high flux). These are most prominently (i) a region with accelerated transport around the XY-coordinates (20 | 40) which is much less pronounced in the high-flux experiments; (ii) the band with delayed transport which extends across the entire horizontal cross-sections in the direction of the structural feature in the topsoil is not clearly developed for the low-flux experiments. Instead, the velocity patterns are rather congruent with the location of the irrigation device segments. Here, the transport patterns were possibly influenced by spatially heterogeneous irrigation.

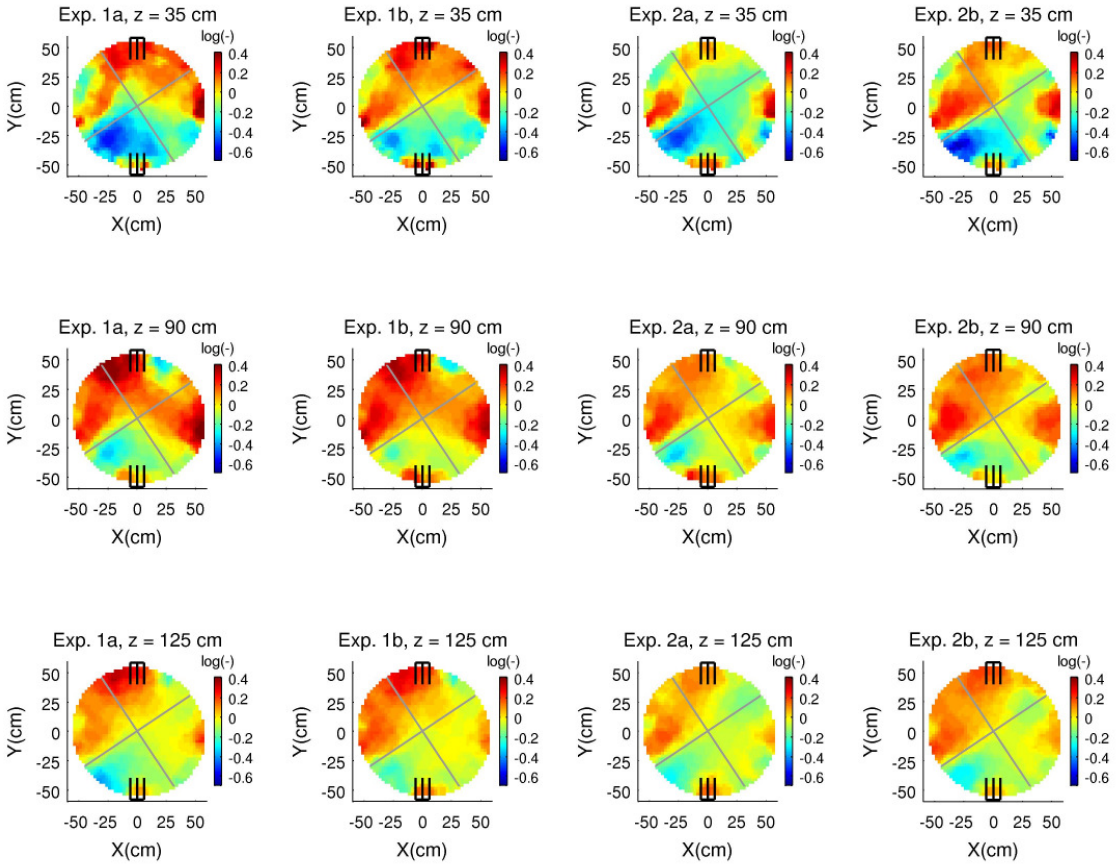


**Figure 5.6: Horizontal cross-sections of the voxel-scale integral velocities $v_{vox,ERT}$ normalized to the corresponding column-scale integral velocities $v_{col,EFFL}$ for the effluent BTC in three different depths. Additionally, the locations of the TDR probes and irrigation device segments are shown.**

The logarithms of the voxel-scale local velocities $u_{vox,ERT}$ normalized to the corresponding column-scale integral velocity for the effluent BTC $v_{col,EFFL}$ are depicted in Figure 5.7. The $u_{vox,ERT}$ patterns at a depth of $z$ = 35 cm show evidence that, for the high-flux experiments, the $v_{vox,ERT}$ features aligned to the soil structure in the topsoil are generated at the bottom of the plow layer. For the experiments 1a and 1b, in contrast, the patterns at $z$ = 35 cm visually differ from each other and are at best approximately aligned to the structure in the topsoil. This indicates again that the velocity patterns in the topsoil may be affected by inhomogeneous irrigation, especially if we consider that the spatial irrigation homogeneity provided by the irrigation device was known to be smaller for low irrigation rates. In the vertical middle of the column, the $u_{vox,ERT}$ patterns of all experiments are more similar (Figure 5.7). For the low-flux experiments, two patches of accelerated transport are noticeable in the bottom part of the column (Figure 5.7, $z$ = 100 cm). Note that patches with large $u_{vox,ERT}$ do not necessarily indicate fast transport. When deriving $u_{vox,ERT}$ we assumed that transport takes place in the vertical direction only, which is an approximation of the true 3-D flow field. For example, spots with large $u_{vox,ERT}$ may also be related to a location where solute is laterally bypassing an above located region with very low hydraulic conductivity.

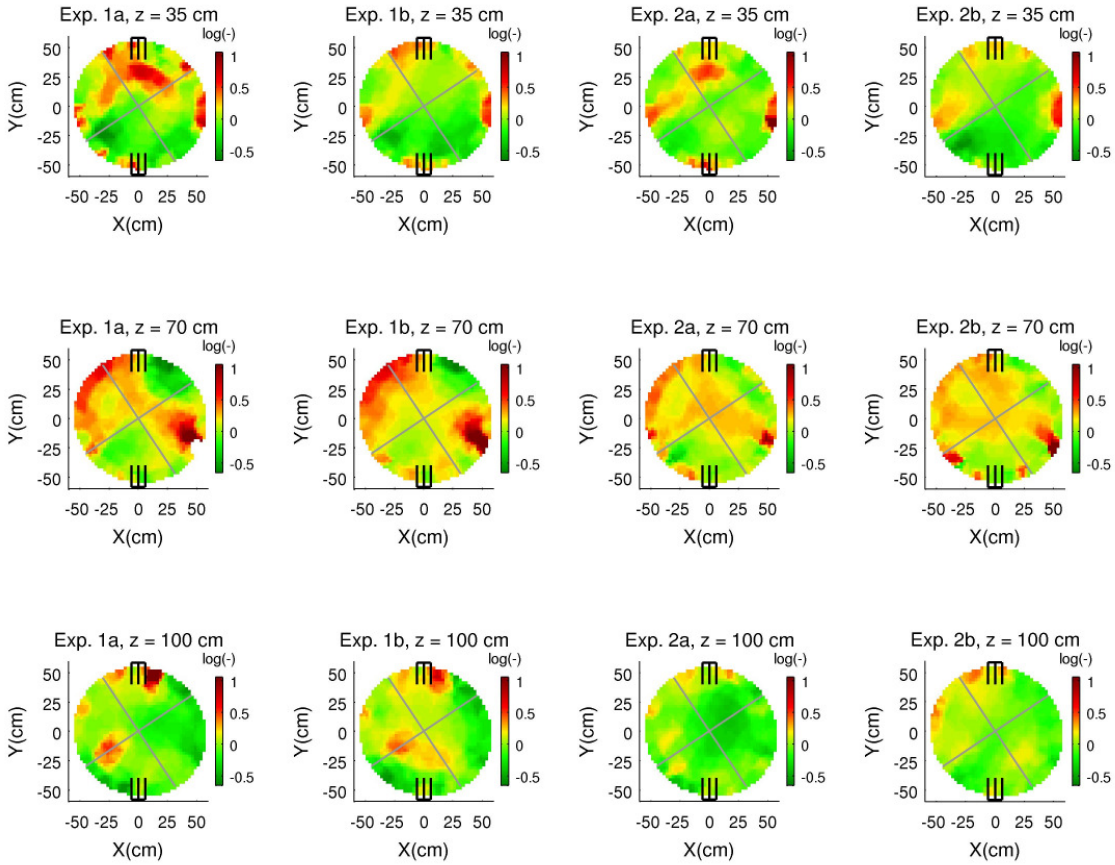


**Figure 5.7: Horizontal cross-sections of the voxel-scale local velocities $u_{vox,ERT}$ normalized to the corresponding column-scale integral velocities $v_{col,EFFL}$ for the effluent BTC in three different depths. Additionally, the locations of the TDR probes and irrigation device segments are shown.**

Figure 5.8 completes the voxel-based transport analysis showing the voxel-scale dispersivities $\lambda_{vox,ERT}$. Due to the large precision error in $\lambda_{vox,ERT}$ (see chapter 4.3.5) structures in or similarities between dispersivity patterns are only weakly discernable. At best, features oriented in direction of the above discussed structural feature in the topsoil are visible.

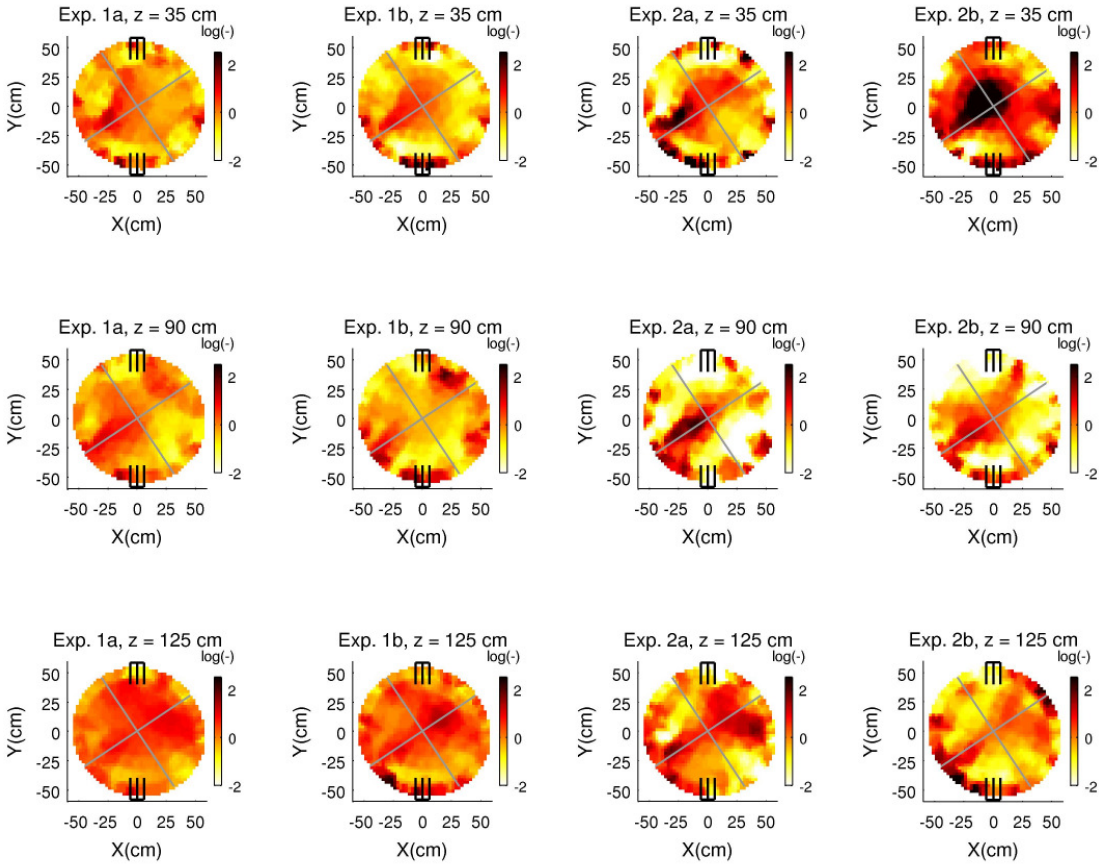


**Figure 5.8: Horizontal cross-sections of the voxel-scale dispersivities $\lambda_{vox,ERT}$ normalized to the corresponding column-scale integral dispersivity $\lambda_{col,EFFL}$ for the effluent BTC in three different depths. Additionally, the locations of the TDR probes and irrigation device segments are shown.**

## 5.3.4. Inference to Mixing Regime

In chapter 4.3.5 we concluded that the ERT-derived voxel-scale dispersivity overestimates the TDR-derived one by approximately 50% on average and that this bias is not sensitive to the ERT sensitivity distribution. The mean voxel-scale dispersivities $\langle\lambda_{vox,ERT}\rangle$ overestimated the TDR-derived dispersivities by a similar amount (Figure 5.5) and there are no indications that the residuals between $\langle\lambda_{vox,ERT}\rangle$ and $\langle\lambda_{tdr,TDR}\rangle$ depend on the travel distance. In contrast, in chapter 4.3.6 we found that the variability of $v_{vox,ERT}$ was underestimated due to smoothing associated with the ERT data inversion leading to an underestimation of $\lambda_{adv,ERT}$. Supposing that the underestimation is not dependent on the travel distance we can infer the mixing regime from the dispersivity profile.

Neglecting the uppermost 30 (50) cm for the low (high)-flux experiments, Figure 5.5 shows that the column-scale dispersivity remains approximately constant with travel distance for all four experiments, indicating a Fickian solute mixing regime (CD mixing regime). This result is further corroborated by the $CV_v$ of the integral voxel-scale velocities which are exclusively decreasing with depth whereas the respective $CV_u$ of the local velocity remains approximately constant (Figure 5.9).

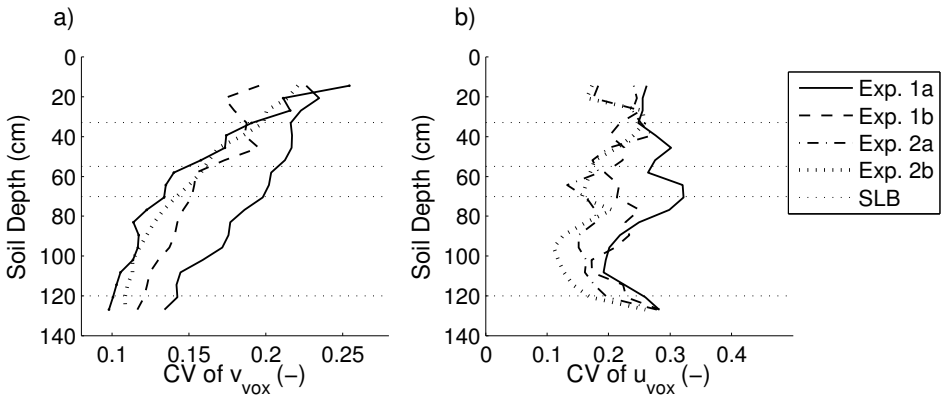


**Figure 5.9: (a) Depth-wise coefficients of variations of the voxel-scale integral velocities $v_{vox,ERT}$ and (b) local velocities $u_{vox,ERT}$. SLB stands for soil layer boundary.**

## 5.3.5. Effect of Lateral Observation Scale on Dispersivity

Figure 5.5 depicts that the ERT-derived column-scale dispersivity $\lambda_{col,ERT}$ is successfully estimated by the mean voxel-scale dispersivity $<\lambda_{vox,ERT}>$ calculated according to Eq. (5.4) and the advective dispersivity $\lambda_{adv,ERT}$ which was derived by means of Eq. (5.5). We conclude that the up-scaling approach is suitable to investigate the relationship between lateral observation scale and dispersivity.

From Figure 5.5 it can be seen that the average ERT-derived voxel-scale dispersivities $<\lambda_{vox,ERT}>$, as well as the average TDR-derived TDR-scale dispersivities $<\lambda_{tdr,TDR}>$, are clearly smaller than the column-scale dispersivity. It follows that the soil investigated in our study is susceptible to increasing dispersivity with increasing lateral observation scale for the considered range of scales and for the imposed initial and boundary conditions.

Figure 5.10 illustrates that the differences between the four experiments in column-scale dispersivities measured in the effluent $\lambda_{col,EFFL}$ are, to a large part, generated above the voxel scale of $s$ = 7 cm. The average voxel-scale dispersivities are more similar for all experiments and range (at depth $z$ = 127 cm) from 0.9 to 1.3 cm as opposed to 1.7 to 2.5 cm at the column scale (see chapter 4). Notably, the dispersivities between experiments with identical hydrologic initial and boundary conditions differ already considerably at smaller depths. This is another indication that the solute transport was in part influenced by heterogeneous irrigation.

Unlike Javaux and Vanclooster (2003), we did not find indications that the mixing regime shifted with lateral observation scale. In their case, this was probably due to very pronounced macroscopic structural soil features which influenced large scale transport. The shapes of the dispersivity profiles in our study were similar for all lateral observation scales considered (Figure 5.10). The lateral-scale to dispersivity relationships in the topsoil appear to be merely related with the applied irrigation (Figure 5.10, $z$ = 50 cm). For $z$ = 130 cm, in contrast, they are remarkably well correlated with the irrigation rate (Figure 5.10). Most notably, for these depths, the discrepancy in dispersivity between low flux and high flux appears to be generated at scales $s$ < 7 cm; in contrast, the differences in dispersivity of experiments with identical water flux appear to be induced at scales $s$ > 40 cm (Figure 5.10).

Apart from this result, the relationship between increase of dispersivity and lateral observation scale was approximately linear which is in contrast to the findings of Persson et al. (2005). In our study, systematic deviations from linearity can be observed as

a complete cessation of dispersivity-increase for $s$ = 40 cm, which is observable for all experiments and almost all depths (Figure 5.10). It can be speculated whether this is related to structural features in the hydrologic soil properties and state variables with a similar scale, particularly as the scale of 40 cm corresponds more or less to the width of the discussed soil structural feature in the topsoil. Furthermore, Figure 5.10 shows that the dispersivity to lateral-scale relationship does not asymptotically approach a maximum but appears to increase for lateral observation scales larger than 120 cm. It is, therefore, likely that the column-scale dispersivity $\lambda_{col}$ underestimates the field-scale dispersivity. This is in agreement with a review by Vanderborght and Vereecken (2007b) who found that dispersivities that were observed in coarse textured soils were in general smaller in column than in field-scale studies.

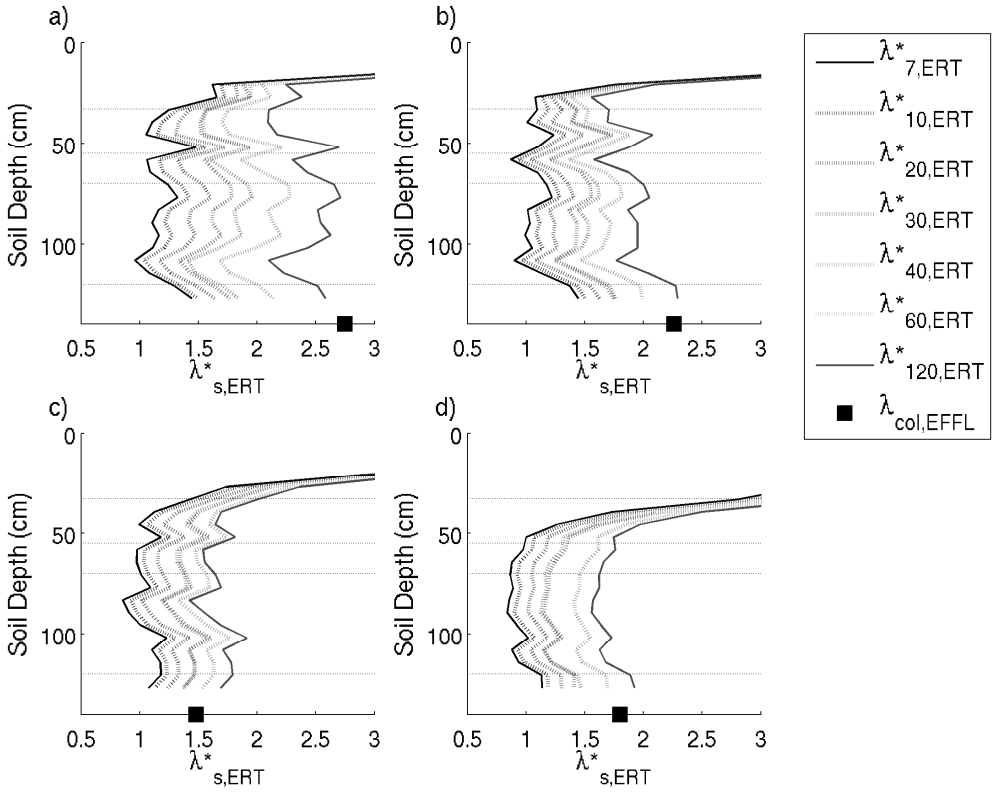


**Figure 5.10: The ERT-derived dispersivity profiles $\lambda^*_{s,ERT}$ for different lateral observation scales $s$ for experiments 1a (a), 1b (b), 2a (c), and 2b (d). Additionally, the dispersivity of the effluent BTC $\lambda_{col,EFFL}$ and the soil layer boundaries are shown.**

In the light of the above discussed findings and with reference to the results of Persson et al. (2005), we believe that the function that links dispersivity to lateral observation scale is suitable to identify scales of heterogeneity that are important to solute transport characteristics.

## 5.4. Summary and Conclusions

In this study we investigated the 3-D spatio-temporal transport characteristics of four tracer displacement experiments carried out for two distinct hydraulic steady states in a large

unsaturated undisturbed soil column. By means of ERT-derived apparent CDE-parameters we were able to non-invasively characterize the respective transport processes with 3-D resolution. Furthermore, TDR-data was used (alongside) with tensiometer data, which both provided important hydrologic state variables, namely the water content and the suction head. The experimental approach offered unprecedented spatio-temporal resolution and a means to investigate the transport processes inside the soil column.

The hydrologic state variables were largely influenced by a hydraulically less conductive soil layer within the topmost 30 cm and by the seepage bottom boundary condition. As a result, both water content and suction head were minimal in the vertical middle of the column and increased near its bottom and top. For the high-flux experiments, a secondary less permeable soil layer was observed in a depth of 70 cm, which led to an increased water content and an (in absolute terms) increased hydraulic head gradient at this depth.

For all four experiments, the (1-D) column-scale local velocity profiles indicate accelerated transport in the vertical middle of the column where the water content is minimal. In the same depth, the column-scale local velocities indicate accelerated transport (when compared to the respective integral velocities) for high-flux experiments, whereas the local velocities for low-flux experiments match the corresponding integral velocity. Apart from this, the zones of accelerated and retarded transport are identical for all depths and all experiments. Also, for 70 cm depth, the TDR-derived piston-flow velocities for the high-flux are considerably lower than the ERT-derived local velocities. The mismatch may be caused by solute bypassing a sizeable part of the water filled pore space. Alternatively, the column-scale water content may have been overestimated by TDR. Apart from the discussed deviation, the piston-flow and local velocities coincide for all depths and experiments. This suggests that differences in solute transport characteristics that were induced by alteration of the initial and boundary conditions are most likely in a depth of 70 cm.

However, despite the discussed differences in hydrologic state variables and 1-D solute transport velocities between the low and high-flux experiments, the transport velocity patterns were very similar for all 4 experiments. Most notably, a strong coincidence between the voxel-scale CDE-parameter patterns and a man-made structural feature in the topsoil was observed for all experiments. Apart from this we found indications that spatio-temporal heterogeneities of the applied irrigation had a measureable influence on solute front evolution. We consider it therefore needful to monitor the experiment's boundary conditions with similar spatio-temporal resolution as the one applied to the solute transport monitoring.

The column-scale dispersivities were small (< 3 cm) for all experiments. They were slightly reduced for the high-flux experiments as compared to the low-flux experiments. The small values already suggest a rather homogeneous transport and lateral mixing. The column-scale dispersivity profiles and the profiles of coefficients of variations of the integral and local-scale velocities support this statement as they identify the transport process as convective-dispersive. Nevertheless, the 3-D resolved transport velocity fields within the column gave a more heterogeneous picture of the transport process. An important conclusion that can be drawn from this observation is that a transport process that appears to be homogeneous at the scale of a column may hide a macroscopically (i.e. at a scale which is much larger than the characteristic length scale of the pore network) heterogeneous transport process within the column. As well, one can conclude that a transport process that appears heterogeneous at a local scale may nevertheless be described

at a larger scale using a transport model that assumes homogeneous flow and perfect lateral solute mixing.

When investigating the relationship between lateral observation scale and apparent dispersivity, we found that our up-scaling approach was able to predict the column-scale dispersivity on basis of the voxel-scale integral velocities and dispersivities. The up-scaling approach also proved to be useful to explicitly allocate apparent dispersivity increments to the corresponding increase of lateral observation scale. For all four experiments, we found that approximately half of the column-scale apparent dispersivity was generated below the voxel scale. Above the voxel scale, the dispersivity increased linearly with lateral scale except for the scale of 40 cm. This may be related to the scale of prominent features in the velocity field. Notably, the width of the band of decreased transport velocities that was aligned to the man-made feature in the topsoil had a similar width. The investigation on the lateral scale-dependency of the dispersivity yielded furthermore that the dispersivity does not reach an asymptotical value for the larger scales considered in our study. Instead it appears to increase further for scales beyond the column scale. This suggests that the column-scale dispersivity likely underestimates the field-scale dispersivity. Due to the promising results, we consider the relationship between dispersivity and lateral observation scale as a potentially effective tool for characterizing solute transport in future studies.

For future experiments, we consider it necessary to investigate whether ERT can be used in soils exhibiting more heterogeneous transport and a lack of lateral solute mixing. Of special interest will be the monitoring of preferential flow and transport processes through macropores, which is an important process in fine textured soils. Based on the results of Olsen et al. (1999) and the results from this study, it seems clear that ERT does not offer sufficient high spatial resolution to directly visualize transport through individual macropores, at least not for the scales considered here. However, whether the quantitative impact of rapid transport through a small fraction of the total pore space can be monitored or indirectly observed using ERT remains to be investigated.

# 6. Summary, Conclusions, and Outlook

## 6.1. Summary

This thesis explores the potential of non-invasive quantitative 3-D spatio-temporal imaging of solute displacement through unsaturated soil using ERT. Such imaging is needed to unequivocally relate soil structure, hydrologic initial and boundary conditions, observation scale, and solute transport process. ERT has shown potential to provide the required image data. However, a quantitative interpretation of ERT-image derived data is difficult due to the non-uniqueness of the ERT-inversion problem; technical limitations to appraising the (spatially varying) ERT-image accuracy and resolution; the lack of an independent method to ground-truth the ERT-image data in unsaturated soil; difficulties to parameterize a petrophysical relationship with 3-D resolution. Therefore, most of the so-far published studies that use ERT to image solute transport processes with spatial resolution are restricted to rather qualitative interpretations (e.g. al Hagrey et al., 1999) or report large bias in the ERT data (e.g. Binley et al., 2002b; Singha et al., 2005).

The objective of this thesis was to further investigate the potential and limitations of ERT to quantitatively visualize and characterize solute transport in 3-D spatio-temporal resolution in a large undisturbed unsaturated soil column. The studies carried out in the framework of the thesis provided various results which are important and novel in the considered field of research. In the following, results and innovative aspects are summarized and grouped into three sub-section entitled (i) experimental setup and ERT data processing; (ii) validation of ERT-derived parameters; (iii) solute transport characterization using ERT.

### 6.1.1. Experimental Setup and ERT data processing

The choice of the large column scale ($58 \times 58 \times 140 \times \pi$ cm³) was beneficial for the purpose of the thesis. Thus, the soil was accessible from all sides where electrodes could be installed with regular spacing and with good electrical contact to the soil, which provided a high spatial resolution spatial resolution (< 0.4 dm³ in vicinity to the electrodes) and minimized the ERT measurement error. Furthermore, the limited size of the column helped to control the hydrologic boundary conditions. The latter was crucial for the quantitative interpretation of the ERT-image data. At the same time, transport processes in an undisturbed soil block considerably larger than the laboratory scale could be investigated.

With respect to data acquisition, it was discovered that the joint application of ERT and TDR works out but is aggravated by the design of the TDR-multiplexing devices used in this study (Campbell Scientific SDMX50). The multiplexing system allows the ERT-injected electrical current to flow from one TDR probe to another via the TDR-cable's shielding and the multiplexers. It was found that the ERT-image data exhibited distinctive artifacts if ERT and TDR data were collected at the same time. These artifacts rendered even a qualitative interpretation of the ERT images impossible. Built-in relays which disconnected the TDR-probes from the multiplexing system whenever the ERT device was active proved to be a workaround. TDR was switched on solely when the ERT device was not measuring. Due to the temporal offset the joint application of both methods became possible. Based on the experience gathered during the experiments, it is considered mandatory to assure that the TDR multiplexing system galvanically separates the TDR-probes from each other if ERT measurements are carried out in vicinity of the TDR-probes.

Furthermore, a refined method is presented to quantitatively characterize the error in the ERT data. The ERT-error appraisal is based on an analysis of the deviation between normal and reciprocal transfer resistances. The method was useful to spot outliers in the ERT data and helped to identify an appropriate error level to which the ERT-data was fitted. As a spin-off, the relationship between ERT error-level and water and solute saturation could be investigated.

With regard to the ERT-image data interpretation, an approach was introduced which had formerly been used to translate bulk electrical conductivity to solute concentration for electrical conductivity BTCs of TDR data (Mallants et al., 1996). The approach requires hydraulic steady state as well as the knowledge of the spatial distribution of the solute concentration for two distinct solute-saturation states. Furthermore, corrections of the electrical conductivity due to temperature shifts must be considered. The discussed requirements render the approach rather impractical for field applications. However, the big advantage is that it enables translation of bulk electrical conductivity to solute concentration without knowledge of the petrophysical properties of the considered porous medium and without disregarding the 3-D heterogeneity of the petrophysical parameters. Cross-checks of the ERT-derived tracer mass with the mass balance certify the good performance of the approach as the error in the ERT-derived mass was predominantly smaller than 5 % for all experiments. This is an exceptional result as ERT-derived tracer masses are normally prone to large bias, i.e. with mass balance errors larger than 50 % in the case of Singha and Gorelick (2005) or Binley et al. (2002b).

### 6.1.2. Validation of ERT-derived Parameters

The ERT-image data was compared to the corresponding TDR-derived electrical conductivity. It was investigated how the choice of the error level used in ERT-image reconstruction affects the ERT-derived bulk electrical conductivities, solute concentrations and apparent CDE-parameters. One important outcome is that all three quantities were matching the respective TDR-derived ones as long as an adequate error level was chosen. This shows that TDR-data is able to ground-truth the ERT data. With respect to the ERT-derived apparent CDE parameters, it was observed that the apparent velocities were barely affected by the choice of the ERT error level. The apparent dispersivities, in contrast, exhibited a strong dependence on the latter. Moreover, it was found that the precision and accuracy was considerably larger for ERT-derived apparent velocities than for the corresponding dispersivities. In general, this supports the results of similar studies carried out in the past which showed that ERT recovers the velocity of a solute plume/front better than its spreading (e.g. Singha and Gorelick 2005).

Furthermore, impacts of temporal smearing and spatially varying accuracy and resolution in the ERT-images were investigated. The apparent velocities were less affected by temporal smearing than the apparent dispersivities. The mean apparent velocity was not impaired by ERT-sensitivity whereas its variability was. In contrast to previous findings of Vanderborght et al. (2005), the apparent dispersivity was not correlated with decreasing ERT sensitivity. The explanation for this fact may be that Vanderborght et al. (2005) relied on a 2-D inversion code to investigate a 3-D problem.

Finally, photographically-derived Brilliant Blue staining patterns were compared to corresponding ERT-image data. The important novelty in the here presented approach is that the ionic charge of the Brilliant Blue molecules is exploited for ERT imaging. The photographically and ERT-derived dye staining patterns coincided for regions connected to

the ERT electrodes. Brilliant Blue staining patterns that were cut off from the electrodes were not recovered by ERT. This illustrates both, the general ability of ERT to non-invasively provide the structure of electrical conductivity distributions as well as the severe loss of resolution and accuracy with increasing distance to the electrodes which, in turn, depends on the spatial distribution of the electrical conductivity itself. ERT bulk electrical conductivity and photographically-derived Brilliant Blue concentrations could be reconciled with reasonable parameterizations of petrophysical models as long as ERT imaged the dye distribution sufficiently well. The results show that the two methods, ERT and dye staining, can be combined in a quantitative way. It follows that both methods are suited for mutual ground-truth. Furthermore, time-lapse ERT data could be used to aid with the interpretation solute transport leading to Brilliant Blue staining patterns in excavated soil in the course of solute displacement experiments. Finally, information on photographically derived Brilliant Blue concentrations could be used to regularize the ERT inversion problem which may improve the ERT image reconstruction.

### 6.1.3. Solute Transport Characterization using ERT

Four inert solute transport experiments in a large undisturbed unsaturated soil column were carried out in the framework of this thesis. Two experiments were conducted with an irrigation rate of 1.5 cm/d, the remaining two with an irrigation rate of 6.5 cm/d. The ERT image data proved to be useful to quantitatively investigate and compare the solute transport characteristics of the four experiments. It was shown that the main velocity patterns remained invariable for all four experiments despite a considerable increase in water content between the low and the high flux experiments. Smaller deviations between the patterns exist whereas the coincidences between experiments with similar flux are clearly larger. Indications were found that the transport patterns may have been influenced by spatial heterogeneity of the applied irrigation. Another important outcome was that all transport velocity patterns were aligned to a structural feature in the topsoil which, in turn, was aligned to the plowing direction and, therefore, identified as a man-made structure.

The mixing regime of all displacement experiments was found to be convective-dispersive despite considerable lateral variations in the local transport velocity. An important conclusion hereof is that a transport process that appears to be homogeneous at the scale of a column may hide a heterogeneous transport process within the column. Also, one can conclude that a transport process that appears heterogeneous at a local scale may nevertheless be described at a larger scale using a transport model that assumes homogeneous flow and perfect lateral solute mixing.

The local ERT-derived apparent dispersivity was successfully laterally up-scaled to the column scale using a newly introduced up-scaling approach. Furthermore, the up-scaling approach is used to investigating the relationship between lateral scale and apparent dispersivity. The apparent dispersivity was linearly increasing with lateral scale except for the scale of approximately 40 cm. The anomaly at this scale may indicate the presence of transport-relevant structures at this scale. Notably, this corresponds to the extension of the man-made structural feature in the topsoil. Moreover, with respect to the relationship between apparent dispersivity and lateral scale, the apparent dispersivity did not converge to a stable value for large scale. This indicates that the dispersivity that was sampled in the effluent underestimates the field scale dispersivity, i.e. the diameter of the soil column may be too small to adequately represent the field scale heterogeneity relevant to solute transport. Based on our results, investigations on the relationship between lateral observation scale, apparent dispersivity, and soil structural features are considered fruitful for future studies.

## 6.2 Conclusions and Outlook

This Ph.D. project provided image series of solute displacement through undisturbed unsaturated soil with, at the considered scale, unprecedented 3-D spatio-temporal resolution. In this way, novel details on the interactions between initial and boundary conditions, observation scale, soil properties, and transport characteristics were investigated. Furthermore, innovations with respect to ERT-data processing, quantitative ERT-image validation by means of TDR, and direct imaging of Brillant Blue with ERT were introduced in this work.

Despite the promising results of this thesis it is clear that standalone ERT imaging has considerable shortcomings for quantitative characterization of solute transport, which require further research efforts. Most aggravating are the large impact of the regularization on the reconstructed ERT-image as well as the loss of resolution and accuracy with distance to the electrodes. The results of this thesis corroborate that the estimation of the solute spreading is especially hindered by the former whereas the latter hampers as well the solute velocity appraisal.

In the thesis, a smoothness constraint was used to regularize the ERT inversion problem. This type of regularization is widely used because of its simplicity and because of advantages with respect to its implementation into numerical codes. However, smoothness-constrained inversion algorithms are not able to resolve sharp electrical conductivity contrasts, which are often found for solute transport in undisturbed soil (e.g. Kasteel et al., 2005). Instead of the smoothness constraint, additional information on the structural properties of the electrical conductivity distribution may be implemented in the regularization term that is used in the ERT-image reconstruction. The additional information could be spatial statistics of the bulk electrical conductivity structure or a corresponding proxy (e.g. Yeh et al., 2002). However, such data is seldom available. Instead, data is preferred which has been, in the ideal case, collected in parallel to the ERT data but with an independent imaging method. For example, GPR and seismics promise potential to act as such a method (e.g. Linde et al. 2006, 2008). The joint application of ERT and GPR appears especially reasonable as the sensitivity of ERT and GPR are complementary and because GPR provides the soil water content in addition to the bulk electrical conductivity. The latter may renders investigations of solute displacement under non-steady hydraulic boundary conditions possible (e.g. Winship et al., 2006).

Another important issue deserving further attention in future research is the determination of confidence intervals for each ERT-derived parameter. In this thesis, the accuracy and resolution of the ERT-images and thereof derived parameters were only implicitly investigated. The reason was the lack of computational power that would have been necessary to apply explicit uncertainty-estimation approaches with 3-D resolution. Presently, suitable methods allowing a spatially resolved estimate of the ERT-image accuracy are evaluated by means of 2-D synthetic scenarios (e.g. Friedel 2003; Oldenborger and Routh, 2009). However, computational restrictions are expected to be overcome in short as the performance of new computer systems continues to increase exponentially. As soon as the uncertainty in the ERT-image data is quantifiable, numerical scenarios could be employed to evaluate performance and error propagation issues, e.g. with respect to apparent CDE parameters voxels BTCs, the dilution index or leaching surfaces.

Beside its imaging capabilities, the great advantages of ERT are its comparatively low

costs, the automatability of the data acquisition and processing, and the applicability over a wide range of scales. Considering this, ERT is expected to play a significant role in 3-D solute displacement imaging in the future, especially, if it is expanded to IP/SIP imaging and/or if it is combined with additional independent measurement methods, in the first instance TDR, GPR, X-ray computed tomography, or MCS.

# A. Appendix

In this appendix we drop the subscript denoting the measurement method (in our case '*ERT*') for the reason that the up-scaling approach does not only apply to ERT data, but is generally valid as long as its underlying assumptions are met.

The column-scale dispersivity $\lambda^*_{col}$ can be related to variance of particle arrival times, *var(t)* at a certain depth z by the following equation (Jury and Sposito, 1985):

$$\lambda^*_{col} = \frac{z \cdot \mathrm{var}(t_j)}{2E(t_j)^2} = \frac{z \sum_{n_{part,c}} \left( t_j - \frac{\sum t_j}{n_{part,c}} \right)^2}{2n_{part,c}} \Bigg/ \left( \frac{\sum t_j}{n_{part,c}} \right)^2 = \frac{z \sum_{n_{part,c}} \left( t_j - \frac{\sum t_j}{n_{part,c}} \right)^2}{2n_{part,c}} \Bigg/ \left( \frac{z}{v^*_{col}} \right)^2 \quad \textbf{(A.1)}$$

where *E(t)* is the expected value of the arrival times, $n_{part,c}$ is the number of particles that crosses the cross-section of the column at depth *z*, and $t_j$ is the arrival time of the $j^{\text{th}}$ particle. The sum of squares in the numerator can be split up in two sums of squares:

$$\begin{aligned} \sum_{n_{part,c}} \left( t_j - \frac{\sum t_j}{n_{part,c}} \right)^2 &= \sum_{n_{part,c}} \left( t_j - \frac{\sum t_j}{n_{part,k}} \right)^2 + \sum_{n_{part,c}} \left( \frac{\sum t_j}{n_{part,k}} - \frac{\sum t_j}{n_{part,c}} \right)^2 \\ &= \sum_{n_{\mathrm{vox}}} n_{part,k}\ \mathrm{var}_{\mathrm{vox,k}}(t) + \sum_{n_{vox}} n_{part,k} \left( \frac{z}{v_{\mathrm{vox},k}} - \frac{z}{v^*_{col}} \right)^2 \end{aligned} \quad \textbf{(A.2)}$$

where $n_{part,k}$ is the number of particles crossing the $k^{\text{th}}$ voxel, which is the voxel where the $j^{\text{th}}$ solute particle crosses the lysimeter cross-section; $var_{vox,k}(t)$ is the variance of the particle arrival times in the $i^{\text{th}}$ voxel, and $n_{vox}$ is the number of voxels in the lysimeter cross-section.

Assuming that $n_{part,k}$ is proportional to the advection velocity to the $i^{\text{th}}$ voxel $v_{vox,k}$ yields

$$\frac{n_{part,k} n_{vox}}{\sum_{n_{vox}} n_{part,k}} = \frac{v_{vox,k}}{v^*_{col}} \quad \textbf{(A.3)}$$

whereas $v^*_{col}$ is the mean velocity in the lysimeter cross-section:

$$v_{col}^{*} = \frac{\sum v_{\mathrm{vox,k}}}{n_{\mathrm{vox}}}.$$

**(A.4)**

As

$$n_{part,c} = \sum_{n_{vox}} n_{part,k}$$

**(A.5)**

it follows that

$$n_{part,k} = \frac{v_{vox,k} n_{part,c}}{n_{vox} v_{col}^{*}}.$$

**(A.6)**

Thus, we can write:

$$\frac{\sum_{n_{part,c}} \left( t_j - \frac{\sum t_j}{n_{part,c}} \right)^2}{n_{part,c}} = \frac{\sum v_{vox,k}\ \mathrm{var}_{\mathrm{vox,k}}(t)}{n_{\mathrm{vox}}\ v_{col}^{*}} + \frac{\sum_{n_{vox}} v_{\mathrm{vox,k}} \left( \frac{z}{v_{\mathrm{vox,k}}} - \frac{z}{v_{col}^{*}} \right)^2}{n_{\mathrm{vox}}\ v_{col}^{*}}$$

$$= \frac{\sum_{n_{\mathrm{vox}}} \frac{2z\lambda_{\mathrm{vox,k}}}{v_{\mathrm{vox,k}}}}{n_{\mathrm{vox}}\ v_{col}^{*}} + \frac{\sum_{n_{vox}} \frac{z^2}{v_{\mathrm{vox,k}}} - \frac{n_{\mathrm{vox}}\ z^2}{v_{col}^{*}}}{n_{\mathrm{vox}}\ v_{col}^{*}}$$

**(A.7)**

where we used the relation between $var_{vox,k}(t)$ and $\lambda_{vox,k}$, which has the same form as the relation between $\lambda^{*}_{col}$ and $var(t)$ given in (A.1) and the relation between $v_{vox,k}$ and $v^{*}_{col}$ given in (A.6).

The assumption of proportionality between $n_{part,k}$ and $v_{vox,k}$ comes down to assuming that the water flux through the voxel is perfectly correlated to the average advection velocity of a particle from the injection surface to the voxel. This assumption is violated when the advection velocity of a particle is not constant along its trajectory. However, based on numerical simulations in heterogeneous conductivity fields, Vanderborght et al. (2005) found that the average BTC can be relatively well reconstructed from local BTCs using this assumption. As a consequence, this assumption is not expected to have large impacts on the estimation of $\lambda^{*}_{\mathrm{col}}$.

Substitution of (A.6) in (A.1) leads to

$$\lambda_{col}^{*} = \frac{v_{col}^{*\,2}}{2z} \left[ \frac{\sum_{n_{\mathrm{vox}}} \frac{2z\lambda_{\mathrm{vox,k}}}{v_{\mathrm{vox,k}}}}{n_{\mathrm{vox}}\ v_{col}^{*}} + \frac{\sum_{n_{vox}} \frac{z^2}{v_{\mathrm{vox,k}}} - \frac{n_{\mathrm{vox}}\ z^2}{v_{col}^{*}}}{n_{\mathrm{vox}}\ v_{col}^{*}} \right]$$

**(A.8)**

and further to

$$\lambda_{col}^{*} = \frac{\sum_{n_{\text{vox}}} \frac{v_{col}^{*} \lambda_{\text{vox,k}}}{v_{\text{vox,k}}}}{n_{\text{vox}}} + \frac{z}{2}\left( \sum_{n_{vox}} \frac{v_{col}^{*}}{v_{\text{vox,k}} n_{vox}} - 1 \right).$$

**(A.9)**

# References

Abbaspour, K., R. Kasteel, R. Schulin. 2000. Inverse parameter estimation in a layered unsaturated field soil. Soil Science 165(2):109-123.

al Hagrey, S. A., J. Michaelson. 1999. Resistivity and percolation study of preferential flow in vadose zone at Bokhorst, Germany. Geophysics 64:746-753.

Annan, A. P. 2005. GPR methods for hydrogeological studies. Pages 185-213 in Hydrogeophysics, by Y. Rubin and S. S. Hubbard (editors). Springer.

Archie, G. E. 1942. The electrical resistivity log as an aid in determining some reservoir characteristics. Trans. Am. Inst. Min. Metall. Pet. Eng. 146:54 - 67.

Bear, J., 1972. Dynamics of Fluid in Porous Media. American Elsevier, New York.

Biggar, J. W., D. R. Nielsen. 1976. Spatial variability of leaching characteristics of a field soil. Water Resources Research 12:78-84.

Binley, A., A. Ramirez, W. Daily. 1995. Regularised image reconstruction of noisy electrical resistance tomography data. *in* 4th Workshop of the European Concerted Action on Process Tomography, European Concerted Action on Process Tomography, Bergen.

Binley, A., S. Henry-Poulter, B. Shaw. 1996a. Examination of solute transport in an undisturbed soil column using electrical resistance tomography. Water Resources Research 32:763-769.

Binley, A., P. Pinheiro, F. Dickin. 1996b. Finite element based three-dimensional forward and inverse solvers for electrical impedance tomography. IEE Colloquium on Advances in Electrical Tomography, London, IEE.

Binley, A., P. Winship P, R. Middleton, M. Pokar, J. West. 2001. High-resolution characterization of vadose zone dynamics using cross-borehole radar. Water Resources Research 37:2639-2652.

Binley, A., P. Winship, L. J. West, M. Pokar, R. Middleton. 2002a. Seasonal variation of moisture content in unsaturated sandstone inferred from borehole radar and resistivity profiles. Journal of Hydrology 267:160-172.

Binley, A., G. Cassiani, R. Middleton, P. Winship. 2002b. Vadose zone flow model parameterisation using cross-borehole radar and resistivity imaging, Journal of Hydrology 267:147-159.

Binley, A., A. Kemna. 2005. Electrical methods. Pages 129-156 *in* Hydrogeophysics, by Y. Rubin and S. S. Hubbard (editors). Springer.

Blümich, B. 2000. NMR-Imaging of Materials, Oxford Science Publications, Oxford.

Börner, F. D., J. R. Schopper, A. Weller. 1996. Evaluation of transport and storage properties in the soil and groundwater zone from induced polarization measurements. Geophysical Prospecting 44(4):583-601.

Buckingham, E. 1907. Studies on the movement of soil moisture. Bulletin 38. USDA Bureau of Soils, Washington, DC.

Chang, P. Y., D. Alumbaugh, J. Brainard, L. Hall. 2006. Cross-borehole ground-penetrating radar for monitoring and imaging solute transport within the vadose zone. Water Resources Research 42, W10413, doi:10.1029/2004WR003871.

Cirpka, O.A., P.K. Kitanidis. 2002. Numerical evaluation of solute dispersion and dilution in unsaturated heterogeneous media. Water Resources Research 38(11), doi:10.1029/2001WR001262.

Clausnitzer, V., J. W. Hopmans. 2000. Pore-scale measurements of solute breakthrough using microfocus X-ray computed tomography. Water Resources Research 36(8): 2067-2079.

Cnudde, V., B. Masschaele, M. Dierick, J. Vlassenbroeck, L. Van Hoorebeke, P. Jacobs. 2006. Recent progress in X-ray CT as a geosciences tool. Applied Geochemistry 21:826–832.

Coquet, Y., C. Coutadeur, C. Labat, P. Vachier, T. van Genuchten, J. Roger-Estrade, J. Simunek. 2005. Water and solute transport in a cultivated silt loam soil: 1. Field observations. Vadose Zone Journal 4:573-586.

Corey, J. C., D. R. Nielsen, D. Kirkham. 1967. Miscible displacement of nitrate through soil columns. Soil Science Society of America Proceedings 31:497-501.

Daily, W., W. Lin, T. Buscheck. 1987. Hydrological properties of Topopah spring tuff - Laboratory measurements. Journal of Geophysical Research-Solid Earth and Planets 92:7854-7864.

Daily, W., E. Owen. 1991. Cross-borehole resistivity tomography. Geophysics 56:1228-1235.

Daily, W., A. Ramirez, D. LaBrecque, J. Nitao. 1992. Electrical-resistivity tomography of vadose water-movement. Water Resources Research 28:1429-1442.

Day-Lewis, F. D., J. W. Lane, J. M. Harris, S. M. Gorelick. 2003. Time-lapse imaging of saline-tracer transport in fractured rock using difference-attenuation radar tomography. Water Resources Research 39(10):1290, doi: 10.1029/2002WR001722.

Day-Lewis, F. D., K. Singha, A. Binley. 2005. Applying petrophysical models to radar travel time and electrical resistivity tomograms: Resolution-dependent limitations. Journal of Geophysical Research-Solid Earth, 110, B08206, doi:10.1029/2004JB003569.

Day-Lewis, F. D., Y. Chen, K. Singha. 2007. Moment inference from tomograms. Geophysical Research Letters 34, L22404, doi:10.1029/2007GL031621.

de Rooij, G.H., F. Stagnitti. 2002. Spatial and temporal distribution of solute leaching in heterogeneous soils: analysis and application to multisampler lysimeter data. Journal of Contaminant Hydrolology 54(3-4):329-346.

de Rooij, G.H., O.A. Cirpka, F. Stagnitti, S.H. Vuurens, J. Boll. 2006. Quantifying minimum monolith size and solute dilution from multi-compartment percolation sampler data. Vadose Zone Journal 5:1086-1092, doi:10.2136/vzj2005.0101

de Smedt, F., F. Wauters, and J. Sevilla. 1986. Study of tracer movement through unsaturated sand. Journal of Hydrology 85:169-181.

Deurer, M., W. H. M. Duijnisveld, J. Bottcher, G. Klump. 2001. Heterogeneous solute flow in a sandy soil under a pine forest: Evaluation of a modeling concept. Journal of Plant Nutrition and Soil Science - Zeitschrift für Pflanzenernährung und Bodenkunde 164(6):601-610.

DIN.EN.27888. 1993. Bestimmung der elektrischen Leitfähigkeit (ISO 7888 : 1985), Deutsche Fassung EN 27 888 : 1993.

Ernst, J. R., H. Maurer, A. G. Green, K. Holliger. 2007. Full-waveform inversion of crosshole radar data based on 2-D finite-difference time-domain solutions of Maxwell's equations. IEEE Transactions on Geoscience and Remote Sensing 45(9), doi: 10.1109/TGRS.2007.901048.

Ewing, R. P., R. Horton. 1999. Discriminating dyes in soil with color image analysis. Soil Science Society of America Journal 63:18-24.

Ferré, T. P. A., J. H. Knight, D. L. Rudolph, R. G. Kachanoski. 1998. The sample areas of conventional and alternative time domain reflectometry probes. Water Resources Research 34:2971-2979.

Flühler, H., W. Durner, M. Flury. 1996. Lateral solute mixing processes - A key for understanding field-scale transport of water and solutes. Geoderma 70(2-4):165-183.

Flury, M., H. Flühler, W. A. Jury, J. Leuenberger. 1994. Susceptibility of soils to Preferential flow of water - a field-study. Water Resources Research 30:1945-1954.

Flury, M., H. Flühler. 1995. Tracer characteristics of Brilliant Blue FCF. Soil Science Society of America Journal 59:22-27.

Flury, M. 1996. Experimental evidence of transport of pesticides through field soils - A review. Journal of Environmental Quality 25(1):25-45.

Forrer, I., R. Kasteel, M. Flury, H. Flühler. 1999. Longitudinal and lateral dispersion in an unsaturated field soil. Water Resources Research 35:3049-3060.

Forrer, I., A. Papritz, R. Kasteel, H. Flühler, D. Luca. 2000. Quantifying dye tracers in soil profiles by image processing. European Journal of Soil Science 51:313-322.

Franson, M. A. H. 1985. Standard methods for the examination of water and wastewater. 16th ed. Am. Public Health Assoc., Washington, DC.

French, H. K., C. Hardbattle, A. Binley, P. Winship, L. Jakobsen. 2002. Monitoring snowmelt induced unsaturated flow and transport using electrical resistivity tomography. Journal of Hydrology 267:273-284.

Friedel, S. 2003. Resolution, stability and efficiency of resistivity tomography estimated from a generalized inverse approach. Geophysical Journal International 153:305-316.

Friedman, S. P. 2005. Soil properties influencing apparent electrical conductivity: a review. Computers and Electronics in Agriculture 46:45-70.

German-Heins, J., M. Flury. 2000. Sorption of Brilliant Blue FCF in soils as affected by pH and ionic strength. Geoderma 97:87-101.

Ghodrati, M., W. A. Jury. 1992. A field-study of the effects of soil structure and irrigation method on preferential flow of pesticides in unsaturated soil. Journal of Contaminant Hydrology 11:101-125.

Gründig, M., M. Richter, A. Seese, O. Sabri. 2007. Tomographic radiotracer studies of the spatial distribution of heterogeneous geochemical transport processes. Applied Geochemistry 22:2334–2343.

Hall, L. D., M. H. G. Amin, E. Dougherty, M. Sanda, J. Votrubová, K. S. Richards, R. J. Chorley, M. Číslerová. 1997. MR properties of water in saturated soils and resulting loss of MRI signal in water content detection at 2 tesla. Geoderma 80:431-448.

Heimovaara, T. J. 1993. Design of triple-wire time-domain reflectometry probes in practice and theory. Soil Science Society of America Journal 57:1410-1417.

Heimovaara, T. J., A. G. Focke, W. Bouten, J. M. Verstraten. 1995. Assessing temporal variations in soil-water composition with time-domain reflectometry. Soil Science Society of America Journal 59:689-698.

Hillel, D. 1980. Applications of soil physics. Academic Press Inc.. San Diego. California.

Hinz, C. 2001. Description of sorption data with isotherm equations. Geoderma 99(3-4):225-243.

Huisman, J. A., S. S. Hubbard, J. D. Redman, A. P. Annan. 2003. Measuring soil water content with ground penetrating radar: A review. Vadose Zone Journal 2:476-491.

Huisman, J. A., C. P. Lin, L. Weihermuller, H. Vereecken. 2008. Accuracy of bulk electrical conductivity measurements with time-domain reflectometry. Vadose Zone Journal 7:426-433, doi: 10.2136/vzj2007.0139.

Jacques, D., J. Vanderborght, D. Mallants, D.-J. Kim, H. Vereecken, J. Feyen. 1997. Comparision of three stream tube models predicting field-scale solute transport. Hydrology and Earth System Sciences 4:873-893.

Jacques, D., D. J. Kim, J. Diels, J. Vanderborght, H. Vereecken, J. Feyen. 1998. Analysis of steady state chloride transport through two heterogeneous field soils. Water Resources Research 34(10):2539-2550.

Jardani, A., A. Revil, F. Santos, C. Fauchard, J. P. Dupont. 2007. Detection of preferential infiltration pathways in sinkholes using joint inversion of self-potential and EM-34 conductivity data. Geophysical Prospecting 55(5):749-760.

Javaux, M., M. Vanclooster. 2003. Scale- and rate-dependent solute transport within an unsaturated sandy monolith. Soil Science Society of America Journal 67:1334-1343.

Javaux, M., J. Vanderborght, R. Kasteel, M. Vanclooster. 2006. Three-dimensional modeling of the scale- and flow rate-dependency of dispersion in a heterogeneous unsaturated sandy monolith. 10.2136/vzj2005.0056, Vadose Zone Journal 5:515-528.

Javaux, M., R. Kasteel, J. Vanderborght, M. Vanclooster. 2006. Interpretation of dye transport in a macroscopically heterogeneous, unsaturated subsoil with a one-dimensional model. Vadose Zone Journal 5(2):529-538.

Jury, W. A., G. Sposito. 1985. Field calibration and validation of solute transport models for the unsaturated zone. Soil Science Society of America Journal 49:1331-1341.

Jury, W. A., K. Roth. 1990. Transfer functions and solute movement through soil. Theory and applications. Birkhäuser Verlag, Basel, Switzerland.

Jury, W. A., H. Flühler. 1992. Transport of chemicals through soil - mechanisms, models, and field applications. Advances in Agronomy 47:141-201.

Kachanoski, R. G., E. Pringle, A. Ward. 1992. Field measurement of solute travel-times using time-domain reflectometry. Soil Science Society of America Journal 56(1):47-52.

Kaestner, A., E. Lehmann, M. Stampanoni. 2008. Imaging and image processing in porous media research. Advances in Water Resources 31:1174–1187.

Kasteel, R; H. J. Vogel, K. Roth. 2002. Effect of non-linear adsorption on the transport behaviour of Brilliant Blue in a field soil. European Journal of Soil Science 53(2):231-240.

Kasteel, R., M. Burkhardt, S. Giesa, H. Vereecken. 2005. Characterization of field tracer transport using high-resolution images. Vadose Zone Journal 4(1):101-111.

Kasteel, R., P. Garnier, P. Vachier, Y. Coquet. 2007. Dye tracer infiltration in the plough layer after straw incorporation. Geoderma 137:360-369.

Kemna, A. 2000. Tomographic inversion of complex resistivity-theory and application. Ph.D Dissertation, University of Bochum, Germany.

Kemna, A., J. Vanderborght, B. Kulessa, and H. Vereecken. 2002. Imaging and characterisation of subsurface solute transport using electrical resistivity tomography (ERT) and equivalent transport models. Journal of Hydrology 267:125-146.

Kemna, A, A. Binley A, L. Slater. 2004. Crosshole IP imaging for engineering and environmental applications. Geophysics 69(1):97-107.

Kemna, A., A. Binley, F. Day-Lewis, A. Englert, B. Tezkan, J. Vanderborght, H. Vereecken, P. Winship. 2006. Solute transport processes. Pages 117-159 *in* Applied Hydrogeophysics, by H. Vereecken, A. Binley, G. Cassiani, A. Revil, and K. Titov (editors). NATO Science Series IV – Earth and Environmental Sciences, Vol. 71, Springer.

Ketelsen, H., S. Meyer-Windel. 1999. Adsorption of Brilliant Blue FCF by soils. Geoderma 90:131-145.

Khalili, A., A. J. Basu, U. Pietrzyk. 1998. Flow visualization in porous media via Positron Emission Tomography. Physics of Fluids 10(4):1031-1033.

Khan, A. U.-H., W. A. Jury. 1990. A laboratory study of the dispersion scale effect in column outflow experiments. Journal of Contaminant Hydrology 5:119-131.

Kitanidis, P. K. 1994. The concept of the dilution index. Water Resources Research, 30:2011-2026.

Knight, R. 1991. Hysteresis in the electrical-resistivity of partially saturated sandstones. Geophysics 56:2139-2147.

Koestel, J. K., A. Kemna, M. Javaux, A. Binley, H. Vereecken. 2008. Quantitative imaging of solute transport in an unsaturated and undisturbed soil monolith with 3-D ERT and TDR. Water Resources Research 44, W12411, doi:10.1029/2007WR006755.

Kung, K.-J. S. 1990. Preferential flow in a sandy vadose zone: 2. Mechanism and implications. Geoderma 46:59-71.

LaBrecque, D., S. H. Ward. 1990. Two-dimensional cross-borehole resistivity model fitting. Pages 51-74 *in* S. H. Ward, editor. Geotechnical and Environmental Geophysics. Society of Exploration Geophysicists, Tulsa.

LaBrecque, D. J., W. Daily, A. Ramirez, A. Binley, S. A. Schima. 1996. ERT monitoring on environmental remediation processes. Measurement Science & Technology 7:375-383.

Lehmann, P., M. Berchtold, B. Ahrenholz, J. Tölke, A. Kaestner, M. Krafczyk, H. Flühler, H.R. Künsch. 2008. Impact of geometrical properties on permeability and fluid phase distribution in porous media. Advances in Water Resources 31:1188–1204.

Lewis, M.G., M. Sharma, H. Dunlap. 1988. Wettability and stress effects on saturation and cementation exponents: Society of Professional Well Log Analysts Logging Symposium, 29th, San Antonio, Texas, Transactions, p. K1-K24.

Linde, N., A. Binley, A. Tryggvason, L. B. Pedersen, A. Revil. 2006. Improved hydrogeophysical characterization using joint inversion of cross-hole electrical resistance and ground-penetrating radar traveltime data. Water Resources Research, 42, W12404, doi:10.1029/2006WR005131.

Linde, N., A. Tryggvason, J. E. Peterson, S. S. Hubbard. 2008. Joint inversion of crosshole radar and seismic traveltimes acquired at the South Oyster Bacterial Transport Site. Geophysics 73(4):G29-G37.

Longeron, D., J. M. Argaud, J. P. Ferraud. 1989. Effect of overburden pressure, nature and microscopic distribution of the fluids on electrical properties of rock samples, Soc. Pet. Eng. Formation Evaluation **6**(2):194-202.

Looms, M. C., K. H. Jensen, A. Binley, L. Nielsen. 2008. Monitoring unsaturated flow and transport using cross-borehole geophysical methods. Vadose Zone Journal 7(1):227-237.

Maciejewski, S. 1993. Numerical and experimental study of solute transport in unsaturated soils. Journal of Contaminant Hydrology 14:193-206.

Mallants, D., M. Vanclooster, M. Meddahi, J. Feyen. 1994. Estimating solute transport in undisturbed soil columns using time-domain reflectometry. Journal of Contaminant Hydrology 17:91-109.

Mallants, D., M. Vanclooster, N. Toride, J. Vanderborght, M. T. van Genuchten, J. Feyen. 1996. Comparison of three methods to calibrate TDR for monitoring solute movement in undisturbed soil. Soil Science Society of America Journal 60:747-754.

Menke, W. 1989. Geophysical data analysis: Discrete inverse theory, Academic Press Inc.

Michot, D., Y. Benderitter, A. Dorigny, B. Nicoullaud, D. King, A. Tabbagh. 2003. Spatial and temporal monitoring of soil water content with an irrigated corn crop cover using surface electrical resistivity tomography. Water Resources Research 39, NO. 5, 1138, doi:10.1029/2002WR001581.

Morelli, G., D. LaBrecque. 1996. Advances in ERT modeling. Eur. J. Environ. Eng. Geophysics 1:171 -186.

Nielsen, D.R., J.W. Biggar, K.T. Ker. 1973. Spatial variability of field-measured soil-water properties. Hilgardia 42:215–259.

Nielsen, J., G. Pinder, T. Kulp, S. Angel. 1991. Investigation of dispersion in porous media using fiber-optic technology, Water Resources Research 27(10):2743-2749.

Nimmer, R. E., J. L. Osiensky, A. M. Binley, B. C. Williams. 2008. Three-dimensional effects causing artifacts in two-dimensional, cross-borehole, electrical imaging. Journal of Hydrology 359(1-2):59-70.

Nützmann, G., S. Maciejewski, K. Joswig. 2002. Estimation of water saturation dependence of dispersion in unsaturated porous media: experiments and modeling analysis. Advances in Water Resources 25:565-576.

Öhrström, P., Y. Hamed, M. Persson, R. Berndtsson. 2004. Characterizing unsaturated solute transport by simultaneous use of dye and bromide. Journal of Hydrology 289:23-35.

Oldenborger, G. A., P. S. Routh, M. D. Knoll. 2005. Sensitivity of electrical resistivity tomography data to electrode position errors. Geophysical Journal International 163:1-9.

Oldenborger, G. A., P. S. Routh, M. D. Knoll. 2007. Model reliability for 3-D electrical resistivity tomography: Appilication of the volume of investigation index to a time-lapse monitoring experiment. Geophysics 72(4):F167-F175.

Oldenborger, G.A., P. S. Routh. 2009. The point-spread function measure of resolution for the 3-D electrical resistivity experiment. Geophysical Journal International 176(2):405-414.

Olsen, P. A., A. Binley, W. Tych. 1999. Characterizing solute transport in undisturbed soil cores using electrical and X-ray tomographic methods. Hydrological Processes 13(2):211-221.

Padilla, I. Y., T.-C. J. Yeh,, M. H. Conklin. 1999. The effect of water content on solute transport in unsaturated porous media. Water Resources Research 35:3303-3313.

Papafotiou, A., R. Helmig, J. Schaap, P. Lehmann, A. Kaestner, H. Flühler, I. Neuweiler, R. Hassanein, B. Ahrenholz, J. Tölke, A. Peters, W. Durner. 2008. From the pore scale to the lab scale: 3-D lab experiment and numerical simulation of drainage in heterogeneous porous media. Advances in Water Resources 31:1253–1268.

Park, S. 1998. Fluid migration in the vadose zone from 3-D inversion of resistivity monitoring data. Geophysics 63:41-51.

Parker, J. C., M. T. van Genuchten. 1984. Flux-averaged and volume-averaged concentrations in continuum approaches to solute transport. Water Resources Research 20:866-872.

Patterson, B. M., P. D. Franzmann, J. L. Rayner, G. B. Davis. 2000. Combining coring and suction cup data to improve the monitoring of pesticides in sandy vadose zones: a field-release experiment. Journal of Contaminant Hydrology 46:187-204.

Perillo, C. A., S. C. Gupta, E. A. Nater, J. F. Moncrief. 1998. Flow velocity effects on the retardation of FD & C Blue No 1 food dye in soil. Soil Science Society of America Journal 62:39-45.

Perillo, C. A., S. C. Gupta, E. A. Nater, J. F. Moncrief. 1999. Prevalence and initiation of preferential flow paths in a sandy loam with argillic horizon. Geoderma 89:307-331.

Perret, J., S. O. Prasher, A. Kantzas, K. Hamilton, C. Langford. 2000. Preferential solute flow in intact soil columns measured by SPECT Scanning. Soil Sci. Soc. Am. J. 64:469–477.

Persson, M., S. Haridy, J. Olsson, J. Wendt. 2005. Solute transport dynamics by high-resolution dye tracer experiments - Image analysis and time moments. Vadose Zone Journal 4:856-865.

Petersen, C. T., S. Hansen, H. E. Jensen. 1997. Tillage-induced horizontal periodicity of preferential flow in the root zone. Soil Science Society of America Journal 61:586-594.

Petersen, C. T., H. E. Jensen, S. Hansen, C. Bender Koch. 2001. Susceptibility of a sandy loam soil to preferential flow as affected by tillage. Soil & Tillage Research 58:81-89.

Peyton, R. L., Anderson, S. H., Gantzer, C. J., Wigger, J. W., Heinze, D. J., Wang, H. 1994. Soil-Core breakthrough measured by X-ray computed tomography. Tomography of Soil-Water-Root Processes. SSSA, Madison, WI. Special Publication No. 36:59-71.

Pütz, T., K. Klimsa. 1991. Profilbeschreibung und Analyseergebnisse des Standortes Kaldenkirchen-Hülst. Interner Bericht, KfA Jülich.

Ramirez, A., W. Daily, D. LaBrecque, E. Owen, D. Chestnut. 1993. Monitoring an underground steam injection process using electrical-resistance tomography. Water Resources Research 29:73-87.

Ramirez, A. L., J. J. Nitao, W. G. Hanley, R. Aines, R. E. Glaser, S. K. Sengupta, K. M. Dyer, T. L. Hickling, W. D. Daily. 2005. Stochastic inversion of electrical resistivity changes using a Markov Chain Monte Carlo approach, Journal of Geophysical Research-Solid Earth 110, B02101, doi: 10.1029/2004JB003449.

Revil, A., P. W. J. Glover. 1998. Nature of surface electrical conductivity in natural sands, sandstones, and clays. Geophysical Research Letters 25:691-694.

Revil, A., L. M. Cathles III, S. Losh. 1998. Electrical conductivity in shaly sands with geophysical applications. Journal of Geophysical Research (B) 103, 23,925-23,936.

Revil, A., A. Finizola, S. Piscitelli, E. Rizzo, T. Ricci, A. Crespy, B. Angeletti, M. Balasco, S. Barde Cabusson, L. Bennati, A. Bole`ve, S. Byrdina, N. Carzaniga, F. Di Gangi, J. Morin, A. Perrone, M. Rossi, E. Roulleau, B. Suski. 2008. Inner structure of La Fossa di Vulcano (Vulcano Island, southern Tyrrhenian Sea, Italy) revealed by high-resolution electric resistivity tomography coupled with self-potential, temperature, and $CO_2$ diffuse degassing measurements, J. Geophys. Res. 113, B07207, doi:10.1029/2007JB005394.

Richards, L.A. 1931. Capillary conduction of liquids through porous mediums. PhD Thesis. Cornell University.

Ritsema, C. J., L. W. Dekker. 1994. How water moves in a water repellent sandy soil 2. Dynamics of fingered flow. Water Resources Research 30(9):2519–2531.

Roth, K., R. Schulin, H. Flühler, and W. Attinger. 1990. Calibration of time-domain reflectometry for water-content measurement using a composite dielectric approach. Water Resources Research 26:2267-2273.

Roth, K. 1995. Steady-State flow in an unsaturated, 2-dimensional, macroscopically homogeneous, Miller-similar medium. Water Resources Research 31(9):2127-2140.

Roth, K., K. Hammel. 1996. Transport of conservative chemical through an unsaturated two-dimensional Miller-similar medium with steady state flow. Water Resources Research 32(6):1653-1663.

Roth, K. 2006. Soil Physics. Lecture Notes. Institute of Environmental Physics, University of Heidelberg.

Rothe, A., W. Weis, K. Kreutzer, D. Matthies, U. Hess, B. Ansorge. 1997. Changes in soil structure caused by the installation of time domain reflectometry probes and their influence on the measurement of soil moisture. Water Resources Research 33:1585-1593.

Rudolph, D. L., R. G. Kachanoski, M. A. Celia, D. R. LeBlanc, J. H. Stevens. 1996. Infiltration and solute transport experiments in unsaturated sand and gravel, Cape Cod, Massachusetts: Experimental design and overview of results. Water Resources Research 32(3):519-532.

Russ, J. C. 1995. The image processing handbook. 2nd edition, CRC Press, Boca Raton, FL.

Sasaki, Y. 1992. Resolution of resistivity tomography inferred from numerical simulation. Geophysical Prospecting 40:453-463.

Sato, T., H. Tanahashi, H. A. Loáiciga. 2003. Solute dispersion in a variably saturated sand. Water Resources Research 39, doi: 10.1029/2002WR001649.

Scheffer, F., P. Schachtschabel. 2002. Lehrbuch der Bodenkunde. 15. Auflage neubearbeitet und erweitert von Hans-Peter Blume u. a. Spektrum Akademischer Verlag, Heidelberg und Berlin.

Schmalholz, J., H. Stoffregen, A. Kemna, U. Yaramanci. 2004. Imaging of water content distributions inside a lysimeter using GPR tomography. Vadose Zone Journal 3:1106-1115.

Schön, J. H. 1998. Physical properties of rocks: fundamentals and principles of petrophysics: 2nd. ed., 583p. pp., Pergamon, Oxford.

Simmons, C. S. 1982. A Stochastic-Convective Transport Representation of Dispersion in One-Dimensional Porous-Media Systems. Water Resources Research 18:1193-1214.

Singha, K., S. M. Gorelick. 2005. Saline tracer visualized with three-dimensional electrical resistivity tomography: field-scale spatial moment analysis. Water Resources Research 41, W05023, doi:10.1029/2004WR003460.

Singha, K., S. M. Gorelick. 2006. Hydrogeophysical tracking of 3-D tracer migration: the concept and application of apparent petrophysical relations. Water Resources Research, 42, W06422, doi:10.1029/2005WR004568.

Slater, L., A. Binley, R. Versteeg, G. Cassiani, R. Birken, S. Sandberg. 2002. A 3-D ERT study of solute transport in a large experimental tank. Journal of Applied Geophysics 49:211-229.

Slater, L., A. M. Binley, W. Daily, R. Johnson. 2000. Cross-hole electrical imaging of a controlled saline tracer injection. Journal of Applied Geophysics 44:85-102.

Spitzer, K. 1998. The three-dimensional DC sensitivity for surface and subsurface sources. Geophysical Journal International 134(3):736-746.

Steenhuis, T. S., W. Staubitz, M. S. Andreini, J. Surface, T. L. Richard, R. Paulsen, N. B. Pickering, J. R. Hagerman, L. D. Geohring. 1990. Preferential movement of pesticides and tracers in agricultural soils. Journal of irrigation and drainage engineering 116(1):50-66.

Stöhr, M., K. Roth, B. Jähne, 2003. Measurement of 3-D pore-scale flow in index-matched porous media. Experiments in Fluids 35, doi:10.1007/s00348-003-0641-x, 159-166.

Suman, R. J., R. J. Knight. 1997. Effects of pore structure and wettability on the electrical resistivity of partially saturated rocks - A network study. Geophysics 62:1151-1162.

Taina, I. A., R. J. Heck, T. R. Elliot. 2008. Application of X-ray computed tomography to soil science: A literature review. Canadian Journal of Soil Science 88(1):1-20.

Taylor, G. 1953. Dispersion of soluble matter in solvent flowing slowly through a tube. Proceedings of the Royal Society of London Series a - Mathematical and Physical Sciences 219:186-203.

Topp, G. C., J. L. Davis, A. P. Annan. 1980. Electromagnetic determination of soil-water content – measurements in coaxial transmission-lines. Water Resources Research 16:574-582.

Toride, N., M. Inoue, F. J. Leij. 2003. Hydrodynamic dispersion in an unsaturated dune sand. Soil Science Society of America Journal 67:703-712.

Ursino, N., T. Gimmi, H. Flühler. 2001. Combined effects of heterogeneity, anisotropy, and saturation on steady state flow and transport: A laboratory sand tank experiment. Water Resources Research 37(2):201-208.

Vanclooster, M., D. Mallants, J. Diels, J. Feyen. 1993. Determining local-scale solute transport Parameters using time-domain reflectometry (TDR). Journal of Hydrology 148(1-4):93-107.

Vanclooster, M., D. Mallants, J. Vanderborght, J. Diels, J. Vanorshoven, J. Feyen. 1995. Monitoring solute transport in a multilayered sandy lysimeter using time-domain reflectometry. Soil Science Society of America Journal 59:337-344.

Vanderborght, J., M. Vanclooster, D. Mallants, J. Diels, J. Feyen. 1996. Determining convective lognormal solute transport parameters from resident concentration data. Soil Science Society of America Journal 60(5):1306-1317.

Vanderborght, J., C. Gonzalez, M. Vanclooster, D. Mallants, J. Feyen. 1997. Effects of soil type and water flux on solute transport. Soil Science Society of America Journal 61:372-389.

Vanderborght, J., D. Mallants, J. Feyen. 1998. Solute transport in a heterogeneous soil for boundary and initial conditions: Evaluation of first-order approximations. Water Resources Research 34(12):3255–3270.

Vanderborght, J., M. Vanclooster, A. Timmerman, P. Seuntjens, D. Mallants, D. J. Kim, D. Jacques, L. Hubrechts, C. Gonzalez, J. Feyen, J. Diels, J. Deckers. 2001. Overview of inert tracer experiments in key Belgian soil types: relation between transport and soil morphological and hydraulic properties. Water Resources Research 37:2873-2888.

Vanderborght, J. 2001. Concentration variance and spatial covariance in second-order stationary heterogeneous conductivity fields. Water Resources Research 37(7):1893-1912.

Vanderborght, J., A. Kemna, H. Hardelauf, H. Vereecken. 2005. Potential of electrical resistivity tomography to infer aquifer transport characteristics from tracer studies: A synthetic case study. Water Resources Research 41(6), W06013, doi: 10.1029/2004WR003774.

Vanderborght, J., R. Kasteel, H. Vereecken. 2006. Stochastic continuum transport equations for field-scale solute transport: Overview of theoretical and experimental results. Vadose Zone Journal 5(1):184-203.

Vanderborght, J., H. Vereecken. 2007a. One-dimensional modeling of transport in soils with depth-dependent dispersion, sorption and decay. Vadose Zone Journal 6:140-148.

Vanderborght, J., H. Vereecken. 2007b. Review of dispersivities for transport modeling in soils. Vadose Zone Journal 6:29-52.

van der Pol, R. M., P. J. Wierenga, D. R. Nielsen. 1977. Solute movement in a field soil. Soil Science Society of America Journal 41:10-13.

van Wesenbeeck, I. J., R. G. Kachanoski. 1991. Spatial scale dependence of in situ solute transport. Soil Science Society of America Journal 55:3-7.

van Wesenbeeck, I. J., R. G. Kachanoski. 1994. Effect of variable horizon thickness on solute transport. Soil Science Society of America Journal 58:1307-1316.

Vereecken, H., R. Kasteel, J. Vanderborght, T. Harter. 2007. Upscaling hydraulic properties and soil water flow processes in heterogeneous soils: A review. Vadose Zone Journal 6:1–28.

Vogel, H. J., K. Roth. 2003. Moving through scales of flow and transport in soil. Journal of Hydrology 272:95–106.

Vogel, H. J., I. Cousin, O. Ippisch, P. Bastian. 2006. The dominant role of structure for solute transport in soil: experimental evidence and modeling of structure and transport in a field experiment. Hydrology and Earth System Sciences 10(4):495-506.

Votrubová, J., M. Císlerová, M. H. G. Amin, L. D. Hall. 2003. Recurrent ponded infiltration into structured soil: A magnetic resonance imaging study. Water Resources Research 39(12), 1371, doi:10.1029/2003WR002222.

Wang, Z., L. Wu, T. Harter, J. Lu, W. A. Jury. 2003. A field study of unstable preferential flow during soil water redistribution. Water Resources Research 39(4), 1075, doi:10.1029/2001WR000903

Ward, A. L., R. G. Kachanoski, A. P. von Bertoldi, D. E. Elrick. 1995. Field and Undisturbed-Column Measurements for Predicting Transport in Unsaturated Layered Soil. Soil Science Society of America Journal 59:52-59.

Waxman, M. H., and L. J. M. Smits. 1968. Electrical conductivities in oil-bearing shaly sands. Society of Petroleum Engineers Journal 8:107-122.

Waxman, M. H., E. C. Thomas. 1974. Electrical conductivity in shaly sands: I. The relation between hydrocarbon saturation and resistivity index. II. The temperature coefficient of electrical conductivity. Society of Petroleum Engineers Journal 14: 213-225.

Weihermuller, L., R. Kasteel, J. Vanderborght, T. Putz, H. Vereecken. 2005. Soil water extraction with a suction cup: Results of numerical simulations. Vadose Zone Journal 4(4):899-907

Weihermuller, L., R. Kasteel, H. Vereecken. 2006. Soil heterogeneity effects on solute breakthrough sampled with suction cups: numerical simulations. Vadose Zone Journal 5(3):886-893.

West, L. J., K. Handley, Y. Huang, M. Pokar. 2003. Radar frequency dielectric dispersion in sandstone: Implications for determination of moisture and clay content. Water Resources Research 39(2), 1026, doi:10.1029/2001WR000923.

Wildenschild, D., K. H. Jensen, K. Villholth, T. H. Illangasekare. 1994. A laboratory analysis of the effect of macropores on solute transport. Ground Water 32(3):381-389.

Wildenschild, D., K. H. Jensen. 1999. Laboratory investigations of effective flow behavior in unsaturated heterogeneous sands. Water Resources Research 35:17-27.

Winship, P., A. Binley, D. Gomez. 2006. Flow and transport in the unsaturated Sherwood sandstone: characterization using cross-borehole geophysical methods. Pages 219–231 *in* R. D. Barker and J. H. Tellam, editors. Fluid flow and solute movement in sandstones: The Onshore UK permo-triassic red bed sequence. The Geological Society of London, London.

Yeh, T. C. J., L. W. Gelhar, A. L. Gutjahr. 1985. Stochastic-Analysis of Unsaturated Flow in Heterogeneous Soils 3: Observations and Applications. Water Resources Research 21:465-471.

Yeh, T. C. J., S. Liu, R. J. Glass, K. Baker, J. R. Brainard, D. Alumbaugh, D. LaBrecque. 2002. A geostatistically based inverse model for electrical resistivity surveys and its applications to vadose zone hydrology, Water Resources Research 38, W01278, doi: 10.1029/2001WR001204.

Yoon, H. K., C. Y. Zhang, C. J. Werth, A. J. Valocchi, A. G. Webb. 2008. Numerical simulation of water flow in three dimensional heterogeneous porous media observed in a magnetic resonance imaging experiment. Water Resources Research 44, W06405, doi:10.1029/2007WR006213.

Zhou, B., T. Dahlin. 2003. Properties and effects of measurement errors on 2-D resistivity imaging surveying. Near Surface Geophysics 1:105-117.